

**FAULTING PARAMETERS OF THE
SEPTEMBER 25, 1998 PYMATUNING,
PENNSYLVANIA EARTHQUAKE**

Monica Maceira

A Digest Submitted to the Faculty of the Graduate School
of Saint Louis University in Partial Fulfillment of
the Requirements for the Degree of
Master of Science (Research)

2000

Digest

Earthquakes in midplate regions have been considered enigmatic since they cannot be easily associated with major plate boundary deformations. In North America, small magnitude midplate seismicity is common in the central and eastern United States and Canada. On September 25, 1998 a moderate-size earthquake occurred in northwestern Pennsylvania, near the border of Ohio and Pennsylvania.

Rapid analyses of seismic waveforms generated by the m_{bLg} 5.2 Pennsylvania -Ohio border region earthquake suggested an unusual, non double-couple component to the faulting mechanism. The existence of a substantial non double-couple component to the faulting mechanism has important implications for the cause of the earthquake (hydrologically induced shallow faulting or “typical” eastern North America basement faulting?). Preliminary checks of the near real-time solutions suggested the non double-couple component may have been an artifact caused by the available data.

One of the goals of this study was to investigate the size of the non double-couple faulting component in the Pymatuning earthquake the other was to improve mechanism and depth estimates for the event. To investigate the detailed nature of this event I used the observed seismograms (from the United States National Seismic Network, USNSN, and from the Canada National Seismic Network, CNSN) to constrain faulting parameters including the source depth, fault strike, dip, and slip, and to explore the reason(s) why early estimates contained large non double-couple

source components. I performed moment tensor inversions with L2 and L1 norms for the closest stations (epicentral distance less than 1000 km), and the results agree with the previous near-real time studies. To test the significance of the non double-couple component I sought a solution constrained to be a pure double couple by checking the match to the observations for all values of strike, dip, and rake (grid search) for depths between 2.5 and 25 km.

The final results show that the Pymatuning earthquake can be explained with a pure double couple faulting mechanism, corresponding to a near-vertical, mostly strike-slip fault with planes striking 110° and 13° , with dips of 70° and 71° , and rakes of 20° and 159° . The estimated moment for this inversion is 5.6×10^{22} dyne-cm, which corresponds to a moment magnitude of 4.5. All three inversions (L2, L1 moment tensor and L1 Grid Search) match the observed seismograms well for a source depth less than 7.5 km. The best “formal” fit is for a 2.5 km deep source, but the 5.0 km depth fits the regional waveforms well. A short period teleseismic P-waveform from northwest Russia is more consistent with a very shallow 2-4 km source.

Although either solution (L2, L1, grid search) fits the regional waveforms well, the preferred solution is the pure double couple, with a depth shallower than 5 km. The Pymatuning earthquake was a small earthquake and most likely a simple rupture. The roughly east-west or north-south striking vertical strike slip mechanism agrees well with existing estimates of the stress field, and is similar to the 1986 Ohio earthquake mechanism (65 km northwest of the Pymatuning event).

**FAULTING PARAMETERS OF THE
SEPTEMBER 25, 1998 PYMATUNING,
PENNSYLVANIA EARTHQUAKE**

Monica Maceira, B.S.

A Thesis Submitted to the Faculty of the Graduate School
of Saint Louis University in Partial Fulfillment of
the Requirements for the Degree of
Master of Science (Research)

2000

COMMITTEE IN CHARGE OF CANDIDACY:

Associate Professor Dr. Ammon,
Chairperson and Advisor

Professor Dr. Herrmann

Professor Dr. Mitchell

Acknowledgments

I dedicate this thesis to my lovely parents and Chispi, I love you. Thanks for being always there supporting me in all the ways even if you disagreed with me.

I want to thank you, the reader, for your interest. I hope my efforts can in some way help you. I would also like to thank Dr. Robert B. Herrmann for giving me the opportunity to study in the States, and I appreciate the careful review of this work by him and Dr. Brian Mitchell. Very special thanks to the person who helped this work to reach an end, Dr. Charles J. Ammon. Thanks Chuck, it was a pleasure to have such an exceptional professor and without you I would probably had never finished. Thanks to my friend Roberto Ortega for his priceless help and support. And thanks to the whole Department of Earth and Atmospheric Sciences of Saint Louis University for accepting me and making me feel at home.

Thanks to all my “old” friends back in Spain and my “new” friends in America, even if you didn’t do anything in this work, thanks just for being there when I needed you. For being always there, especially in the bad moments, my friend Gerardo receives the gold medal. Thank you very much, I don’t have enough words to express my appreciation.

And to that special person in my life who made me laugh when everything looked really bad, who has withstood me and my complaints from the beginning to the end, who listened in silence and gave me his hand when I was falling, thanks very much Nawaz, I love you.

Table of Contents

List of Tables	v
List of Figures	xvi
1 INTRODUCTION	1
2 THE TECTONIC STRESS FIELD IN CENTRAL AND EASTERN NORTH AMERICA	6
3 EARTHQUAKES IN PENNSYLVANIA	12
4 THE PYMATUNING EARTHQUAKE	19
4.1 GENERAL DESCRIPTION	19
4.2 INTENSITY OF THE EARTHQUAKE	20
4.3 HYDROLOGIC EFFECTS	23
5 SEISMIC OBSERVATIONS OF THE PYMATUNING EARTHQUAKE	26
5.1 ANALYSIS OF THE OBSERVATIONS	26
5.1.1 ELECTRONIC SATURATION	30
5.1.2 GWDE - POLARITY REVERSAL	34
6 TIME-DOMAIN MOMENT TENSOR ESTIMATION	36
6.1 THE PYMATUNING EVENT MOMENT-TENSOR	39

6.1.1	LEAST-SQUARES TIME-DOMAIN INVERSION . . .	41
6.1.2	L1 NORM TIME-DOMAIN INVERSION	56
6.2	THE GRID SEARCH	68
6.3	IMPROVING SOURCE DEPTH RESOLUTION	71
7	CONCLUSIONS	87
	BIBLIOGRAPHY	90
	Vita Auctoris	95

List of Tables

2.1	Location and dislocation angles for North American mid-plate earthquakes (From Zoback, 1992, Chang et al., 1998, Ammon et al., 1998).	10
5.1	Seismic stations used in the study	28
5.2	Stations with nonlinear instrument problems. The peak velocity is in counts/s and the units of the peak acceleration are counts/s ²	34
6.1	Weight and bandwidth applied to each component of the different stations used for the moment tensor inversion . . .	40
6.2	Least square moment tensor inversion misfits for different depths. Also moment tensor elements.	42
6.3	L1 Norm moment tensor inversion misfits for different depths. Also moment tensor elements.	58
6.4	Grid search misfits for different depths. Also the obtained fault parameters.	70

List of Figures

1.1	Comparison of the damage areas for the 1906 San Francisco earthquake and the 1811 New Madrid earthquake (after Nuttli, 1981).	3
2.1	Map of seismicity in United States between 1534-1962. From the Decade of North American Geology data base. Each earthquake is represented by a circle. The size of the circle is proportional to the earthquake magnitude (the larger of m_b and M_s is shown in the map).	7
2.2	Map of seismicity in United States from 1963 to the present. From the USGS. Each earthquake is represented by a circle. The size of the circle is proportional to the earthquake magnitude (the larger of m_b and M_s is shown on the map).	7
2.3	Map of central and eastern United States showing focal mechanisms of midplate earthquakes in the area. (From Zoback, 1992, Chang et al., 1998, Ammon et al., 1998).	9

3.1	Map of Pennsylvania state showing the location of historic earthquakes (white circles) and the Pymatuning event (red star). The numbers indicate the ten earthquakes with highest intensities. The table makes reference to these earthquakes indicating the year of occurrence, the number of earthquakes at each location, and the maximum Modified Mercalli intensity of all the earthquakes located at that geographic position.	13
4.1	Map showing intensities in the region near the epicenter which is represented by a star. (From Armbruster J., Barton H., Bodin P., Buckwalter T., Cox J., Cranswick E., Dewey J., Fleegeer G., Hopper M., Horton S., Hoskins D., Kilb D., Maramonte M., Metzger A., Risser D., Seeber L., Shedlock H., Stanley K., Withers M., and Zirbes M.).	22
4.2	Increase in the groundwater level of one of the USGS observation well located in a valley adjacent to the "hydrologic island". (From Armbruster J., Barton H., Bodin P., Buckwalter T., Cox J., Cranswick E., Dewey J., Fleegeer G., Hopper M., Horton S., Hoskins D., Kilb D., Maramonte M., Metzger A., Risser D., Seeber L., Shedlock H., Stanley K., Withers M., and Zirbes M. (USGS)).	25
5.1	Map of North America showing the earthquake (red circle) and stations (yellow triangles) used in this study.	27

5.2	Raw vertical (velocity) component seismogram and its derivative and its integral from station BINY, Binghamton, NY. . .	31
5.3	Raw vertical (velocity) component seismogram and its derivative and its integral from station BLA, Blacksburg, VA. . . .	32
5.4	Raw vertical (velocity) component seismogram and its derivative and its integral from station GAC.	33
6.1	Waveform matches corresponding to the least square moment tensor inversion for 2.5 km depth. The blue line identifies the observations, the red line indicates the predictions. The three components of each stations are shown with an individual amplitude scale.	43
6.2	Waveform matches corresponding to the least square moment tensor inversion for 2.5 km depth. The blue line identifies the observations, the red line indicates the predictions. The three components of each stations are shown with an individual amplitude scale.	44
6.3	Waveform matches corresponding to the least square moment tensor inversion for 2.5 km depth. The blue line identifies the observations, the red line indicates the predictions. The three components of each stations are shown with an individual amplitude scale.	45

6.4	Waveform matches corresponding to the least square moment tensor inversion for 2.5 km depth. The blue line identifies the observations, the red line indicates the predictions. The three components of each stations are shown with an individual amplitude scale.	46
6.5	Waveform matches corresponding to the best-fitting moment tensor (5 km depth). The blue line identifies the observations, the red line indicates the predictions. Each component of each stations is shown with an individual amplitude scale.	47
6.6	Waveform matches corresponding to the best-fitting moment tensor (5 km depth). The blue line identifies the observations, the red line indicates the predictions. Each component of each stations is shown with an individual amplitude scale.	48
6.7	Waveform matches corresponding to the best-fitting moment tensor (5 km depth). The blue line identifies the observations, the red line indicates the predictions. Each component of each stations is shown with an individual amplitude scale.	49

6.8	Waveform matches corresponding to the best-fitting moment tensor (5 km depth). The blue line identifies the observations, the red line indicates the predictions. Each component of each stations is shown with an individual amplitude scale.	50
6.9	Waveform matches corresponding to the least square moment tensor inversion for 7.5 km depth. The blue line identifies the observations, the red line indicates the predictions. The three components of each stations are shown with an individual amplitude scale.	51
6.10	Waveform matches corresponding to the least square moment tensor inversion for 7.5 km depth. The blue line identifies the observations, the red line indicates the predictions. The three components of each stations are shown with an individual amplitude scale.	52
6.11	Waveform matches corresponding to the least square moment tensor inversion for 7.5 km depth. The blue line identifies the observations, the red line indicates the predictions. The three components of each stations are shown with an individual amplitude scale.	53

6.12	Waveform matches corresponding to the least square moment tensor inversion for 7.5 km depth. The blue line identifies the observations, the red line indicates the predictions. The three components of each stations are shown with an individual amplitude scale.	54
6.13	Non double-couple focal mechanism resulting from the least squares moment tensor inversion. Decomposition of this NDC mechanism into a major and a minor double couple. The second decomposition is performed fixing the P axis. . .	57
6.14	Waveform matches corresponding to the best-fitting L1 moment tensor (2.5 km depth). The blue line identifies the observations, the red line indicates the predictions. Each component of each stations is shown with an individual amplitude scale.	59
6.15	Waveform matches corresponding to the best-fitting L1 moment tensor (2.5 km depth). The blue line identifies the observations, the red line indicates the predictions. Each component of each stations is shown with an individual amplitude scale.	60
6.16	Waveform matches corresponding to the best-fitting L1 moment tensor (2.5 km depth). The blue line identifies the observations, the red line indicates the predictions. Each component of each stations is shown with an individual amplitude scale.	61

6.17	Waveform matches corresponding to the best-fitting L1 moment tensor (2.5 km depth). The blue line identifies the observations, the red line indicates the predictions. Each component of each stations is shown with an individual amplitude scale.	62
6.18	Waveform matches corresponding to the best-fitting L1 moment tensor (5 km depth). The blue line identifies the observations, the red line indicates the predictions. Each component of each stations is shown with an individual amplitude scale.	63
6.19	Waveform matches corresponding to the best-fitting L1 moment tensor (5 km depth). The blue line identifies the observations, the red line indicates the predictions. Each component of each stations is shown with an individual amplitude scale.	64
6.20	Waveform matches corresponding to the best-fitting L1 moment tensor (5 km depth). The blue line identifies the observations, the red line indicates the predictions. Each component of each stations is shown with an individual amplitude scale.	65

6.21	Waveform matches corresponding to the best-fitting L1 moment tensor (5 km depth). The blue line identifies the observations, the red line indicates the predictions. Each component of each stations is shown with an individual amplitude scale.	66
6.22	Non double-couple focal mechanism resulting from the L1 norm moment tensor inversion. Decomposition of this NDC mechanism into a major and a minor double couple. The second decomposition is performed fixing the P axis.	67
6.23	Percentage of non double-couple to the faulting mechanism resulted from least-squares, time-domain, moment tensor inversion when one of the stations is not considered.	68
6.24	Percentage of non double-couple to the faulting mechanism resulted from L1 norm, time-domain, moment tensor inversion when one of the stations is not considered.	69
6.25	Pure double couple focal mechanism for the Pymatuning earthquake from the Grid Search.	71
6.26	Waveform matches between observed and synthetic seismograms from the Grid Search assuming a depth source of 2.5 km. The blue line identifies the observations, the red line indicates the predictions. Each component of each stations is shown with an individual amplitude scale.	72

6.27	Waveform matches between observed and synthetic seismograms from the Grid Search assuming a depth source of 2.5km. The blue line identifies the observations, the red line indicates the predictions. Each component of each stations is shown with an individual amplitude scale.	73
6.28	Waveform matches between observed and synthetic seismograms from the Grid Search assuming a depth source of 2.5 km. The blue line identifies the observations, the red line indicates the predictions. Each component of each stations is shown with an individual amplitude scale.	74
6.29	Waveform matches between observed and synthetic seismograms from the Grid Search assuming a depth source of 2.5 km. The blue line identifies the observations, the red line indicates the predictions. Each component of each stations is shown with an individual amplitude scale.	75
6.30	Waveform matches between observed and synthetic seismograms from the Grid Search assuming a depth source of 5.0 km. The blue line identifies the observations, the red line indicates the predictions. Each component of each stations is shown with an individual amplitude scale.	76

6.31	Waveform matches between observed and synthetic seismograms from the Grid Search assuming a depth source of 5.0 km. The blue line identifies the observations, the red line indicates the predictions. Each component of each stations is shown with an individual amplitude scale.	77
6.32	Waveform matches between observed and synthetic seismograms from the Grid Search assuming a depth source of 5.0 km. The blue line identifies the observations, the red line indicates the predictions. Each component of each stations is shown with an individual amplitude scale.	78
6.33	Waveform matches between observed and synthetic seismograms from the Grid Search assuming a depth source of 5.0 km. The blue line identifies the observations, the red line indicates the predictions. Each component of each stations is shown with an individual amplitude scale.	79
6.34	Comparison between the synthetics from the least-squares inversion (blue line) and the grid search (red line) for a source depth of 5 km.	80
6.35	Comparison between the synthetics from the least-squares inversion (blue line) and the grid search (red line) for a source depth of 5 km.	81

6.36	Comparison between the synthetics from the least-squares inversion (blue line) and the grid search (red line) for a source depth of 5 km.	82
6.37	Comparison between the synthetics from the least-squares inversion (blue line) and the grid search (red line) for a source depth of 5 km.	83
6.38	Misfit versus depth for least-squares, L1 norm, and grid search inversions.	85
6.39	Computed body wave seismograms for source depths of 2.5, 5, and 7 km.	86
7.1	Focal mechanisms in Pennsylvania and surrounding states of northeast North America. The Pymatuning event focal mechanism obtained in this study (grey shading for compressional quadrants) is consistent with previous earthquakes in the area.	89

1. INTRODUCTION

Since they cannot be easily associated with major plate boundary deformations, earthquakes in midplate regions have been considered as enigmatic. But tectonic activity driven by plate interactions can extend far from plate boundaries where most of the seismic activity takes place, and even in the most standard geologically quite zones, "stable" is a relative term. Hundreds of events worldwide have taken place in what is considered stable continental crust. Several examples are described in Johnston and Kanter (1990), such as the 1886 Charleston, South Carolina, earthquake which may have been larger than the $M_w = 6.9$, October 18, 1989 Loma Prieta earthquake (near San Francisco). In 1886 water-saturated soil liquefied, erupted in geysers of mud and sand, and toppled buildings. Sixty-three people were killed, 3757 people were injured, and \$6 billion is the estimate of property damage. Another earthquake with dramatic effects struck Kutch, India, in 1819 killing more than 1500 people. A scarp between six and nine meters high and at least ninety kilometers long was thrust up; land to the north of it was elevated while the land to the south was depressed. More recently, the 1993, $M_s = 6.4$ Latur India earthquake killed 10,000. Although the sparse population assured relatively few casualties, the New Madrid events during the winter of 1811-1812 are considered some of the largest events to have occurred in North America. Major earthquakes of this size rarely occur in plate interiors (Johnston and Kanter, 1990).

Small magnitude midplate seismicity is common in the central and eastern United States. The most seismically active region of eastern North America is located along the Mississippi river in southeastern Missouri and the adjacent parts of Arkansas, Illinois, Kentucky, and Tennessee. The New Madrid region contains the epicenters of the large earthquakes during the winter of 1811-1812, and has been active (Nuttli, 1973a) through the historic and instrumental records. The region accounts for about one-third of the earthquakes in the central United States (Nuttli, 1978). However, for the most part, the seismicity rate in the central and eastern United States is low compared to that in more seismically active regions such as California or Alaska (Nuttli, 1978). Still, there are at least three factors that encourage scientific study of earthquakes in the central and eastern United States.

First, the New Madrid seismic zone has been the site of large earthquakes and may be susceptible to future great earthquakes. Second, the low attenuation of seismic wave energy in the frequency range of damaging ground motion, namely about 0.1 to 10 Hz (Nuttli, 1973b; Mitchell, 1973, 1975) means that seismic waves will be felt, and cause damage, over a much larger region in the central United States than would waves from a similar magnitude in regions such as California, where attenuation is much greater (see Figure 1.1). Third, possible characteristics of midplate earthquakes may result in large magnitude earthquakes in midplate regions can occur with relatively short rupture lengths (Nuttli, 1983a). Thus, relatively small faults may have the potential for producing large earthquakes and strong ground motion. Large earthquakes in the central and eastern United States are a low probability but high consequence hazard.

The connections between geology and seismicity remain poorly under-

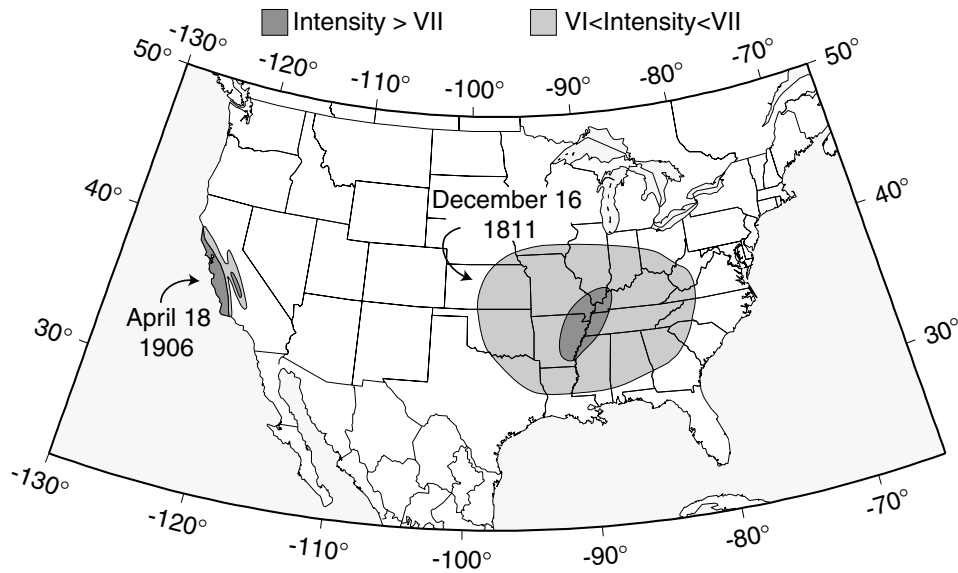


Figure 1.1: Comparison of the damage areas for the 1906 San Francisco earthquake and the 1811 New Madrid earthquake (after Nuttli, 1981).

stood in central and eastern North America. Many of the earthquakes cannot be associated with mapped faults (Mitchell et al., 1991). However, some relations between seismicity and geology in stable continental regions can be established (Wheeler and Johnston, 1992): (a) if rupture generally progresses updip, then the tendency for large earthquakes to rupture more shallowly-dipping surfaces than small earthquakes can explain the scarcity of surface ruptures in central and eastern North America; (b) the few midcrustal earthquakes might be evidence that mafic or granulite facies rocks are present; (c) central and eastern North America seismicity is concentrated in Late Proterozoic and Phanerozoic orogens and extended terranes that rim an older, stable, central craton. Unusually shallow large earthquakes have been observed only in the central craton, where they might cause severe but localized shaking; (d) earthquakes in the Appalachian orogen tend to be shallower than those of comparable

size in the Late Proterozoic rifted continental margin that underlies and borders the northwest side of the orogen.

The majority of earthquake epicenters in central and eastern North America can be associated with a few types of basement structures, most of which can be classified as rifts, uplifts, basins, or former plate boundaries (Mitchell et al., 1991). In this study I analyze a moderate-size earthquake that occurred in September of 1998, near the border of Pennsylvania and Ohio. The earthquake was felt in parts of Michigan, New York, Ohio, and Pennsylvania, and southern Ontario, Canada. It was the largest earthquake in the area since a magnitude (m_b) 5.0 which occurred January 31, 1986 (for a list of more moderately damaging events in the area, see Bradley and Bennett, 1965).

In recent years many areas in the stable continental region have been instrumented with networks of modern, digital seismographs. One advantage of the modern instrumentation is the ability to quickly model and assess the impact of earthquakes in near real-time (within minutes to hours after the earthquake). Such near real-time studies of faulting provide important information for early response (scientific and emergency) to the events. In 1998, initial, rapid analyses of seismic waveforms generated by the m_{bLg} 5.2 Pennsylvania-Ohio border region earthquake suggested an unusual, non double-couple component to the faulting mechanism (G. Ekstrom, personal communication, 1998; Ammon, personal communication, 1998). The existence of a substantial non-double couple component to the faulting mechanism has important implications for the cause of the earthquake (hydrologically induced shallow faulting or typical ENA basement faulting?). Preliminary checks of the near real-time solutions suggested

that the non double-couple component may have been an artifact caused by the available data coverage (Ammon, personal communication, 1998). One of the goals of my research is to investigate the size of non-double couple faulting component in this earthquake. To investigate the detailed nature of faulting in this earthquake, I will use the observed seismograms to constrain faulting parameters including the source depth, fault strike, dip and slip, and to explore the reason(s) why early moment tensor estimates contained large non double-couple source components. To complete this task I will utilize complete seismograms recorded within a few hundred kilometers to the source (including both body and surface-waves) to construct a model of the faulting mechanism consistent with all the available data. I will perform inversions for a general, deviatoric moment tensor, and a pure double couple dislocation source.

2. THE TECTONIC STRESS FIELD IN CENTRAL AND EASTERN NORTH AMERICA

Intraplate seismicity represents diffuse deformation in relatively stable tectonic regions, and in North America it is characterized by widespread seismicity with a low level of both frequency of occurrence and size of the earthquakes. In contrast, plate boundary earthquakes represent forces driving deformation and seismically well defined faults. Seismic activity in western North America is characterized by high level of both frequency of occurrence and size of earthquakes (see Figures 2.1 and 2.2 for comparison of west and central-eastern seismicity in North America).

Reliable measurements of *in situ* stress orientation such as well bore breakouts, earthquake focal mechanisms, hydraulic fracturing measurements, and overcoring measurements made in mines, indicate a uniform maximum shear stress orientation through the intraplate North America region (Zoback and Zoback, 1991), varying between northeast and east and averaging east-northeast. The source of this broad-scale relatively uniform regional stress field is believed to be primarily plate-driving forces (Zoback et al., 1989). Richardson and Reding (1991) proposed that distributed ridge forces are capable of accounting for the dominant east-northeast trend for maximum compression through the North American plate east of the Rocky Mountains.

To determine if earthquake slip vectors are compatible with this broad-scale regional stress field, Zoback (1992) studied 32 well-constrained fo-

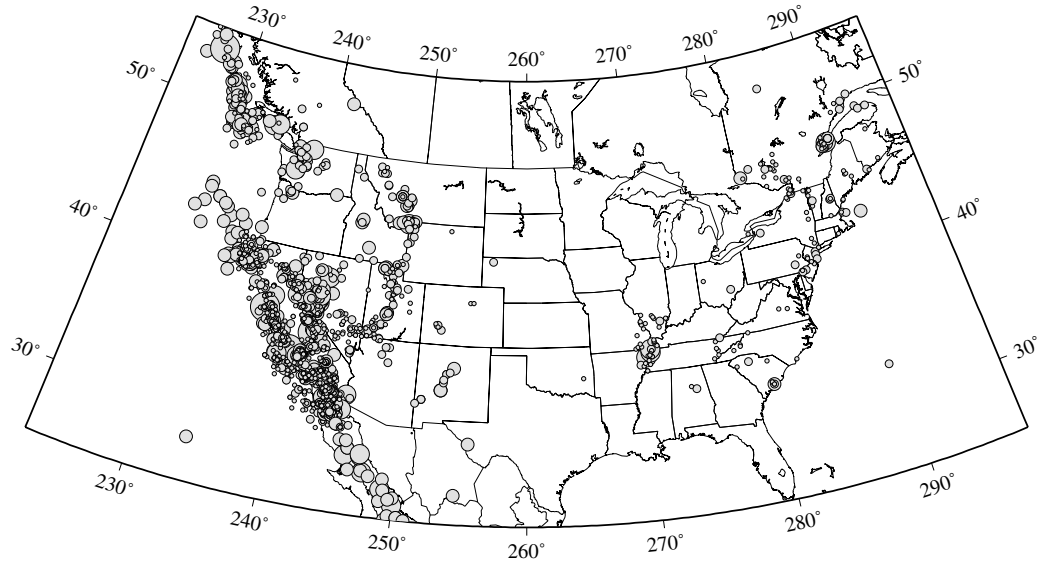


Figure 2.1: Map of seismicity in United States between 1534-1962. From the Decade of North American Geology data base. Each earthquake is represented by a circle. The size of the circle is proportional to the earthquake magnitude (the larger of m_b and M_S is shown in the map).

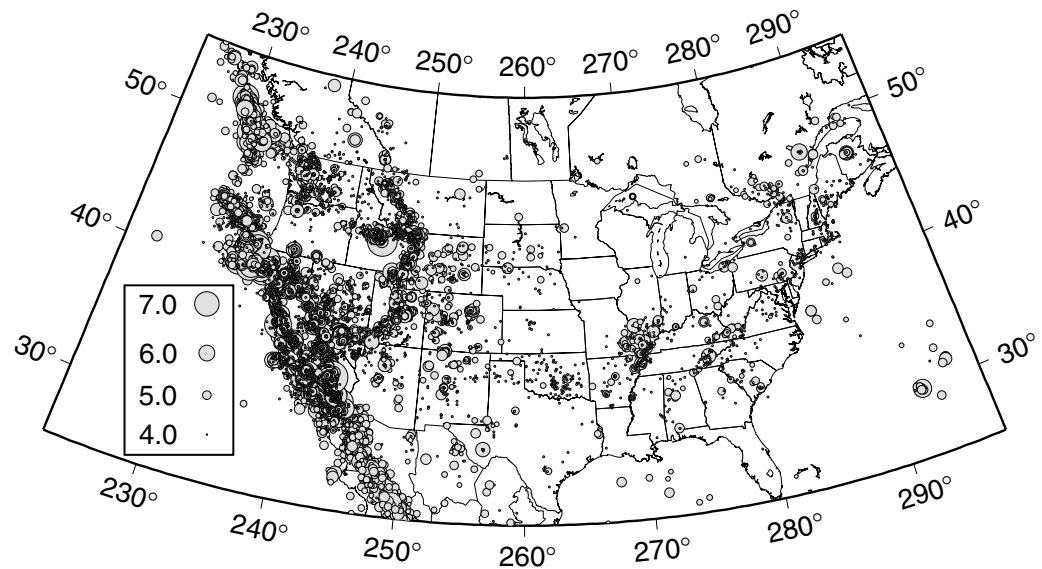


Figure 2.2: Map of seismicity in United States from 1963 to the present. From the USGS. Each earthquake is represented by a circle. The size of the circle is proportional to the earthquake magnitude (the larger of m_b and M_S is shown on the map).

cal mechanisms of North American midplate earthquakes (see Figure 2.3). These observations suggest two different styles of deformation: the central eastern United States earthquakes occur primarily in response to a strike-slip stress regime, whereas the southeastern Canada earthquakes reflect a reverse faulting stress regime (Hasegawa et al., 1985; Talwani and Rajendran, 1991). The contrast in faulting style between the Canadian and United States events is obvious in the focal mechanism plots in Figure 2.3 which indicate a variation in plunge of the T axes (Zoback, 1992). In the central and eastern United States, earthquakes are generally strike slip events with T axes dipping between 43° and 80° , with most in the 60° - 75° range; whereas most of the Canadian and northeast U.S. events show shallow dipping T axes (20° - 50°).

Two hypotheses have been proposed to explain the intraplate seismicity: (a) selective reactivation of preexisting faults by local variations in pore pressure, fault friction, and/or strain localization along favorably oriented lower crustal ductile shear zones formed during earlier deformation (Zoback et al., 1985); (b) local stress perturbation may produce events incompatible with the regional stress field (Zoback et al., 1987).

Zoback (1992) found that (see Table 2.1) slip in a majority of the earthquakes (25 of 32) was geometrically compatible with reactivation of favorably oriented preexisting fault planes in response to the broad-scale uniform regional stress regime. Slip in 23 of the 25 geometrically compatible earthquakes is also frictionally compatible with a relatively uniform regional stress field. The combination of slightly elevated pore pressure and a reduced coefficient of friction would result in slipping on these 23 well-oriented faults. Slip in five events was inconsistent with the regional

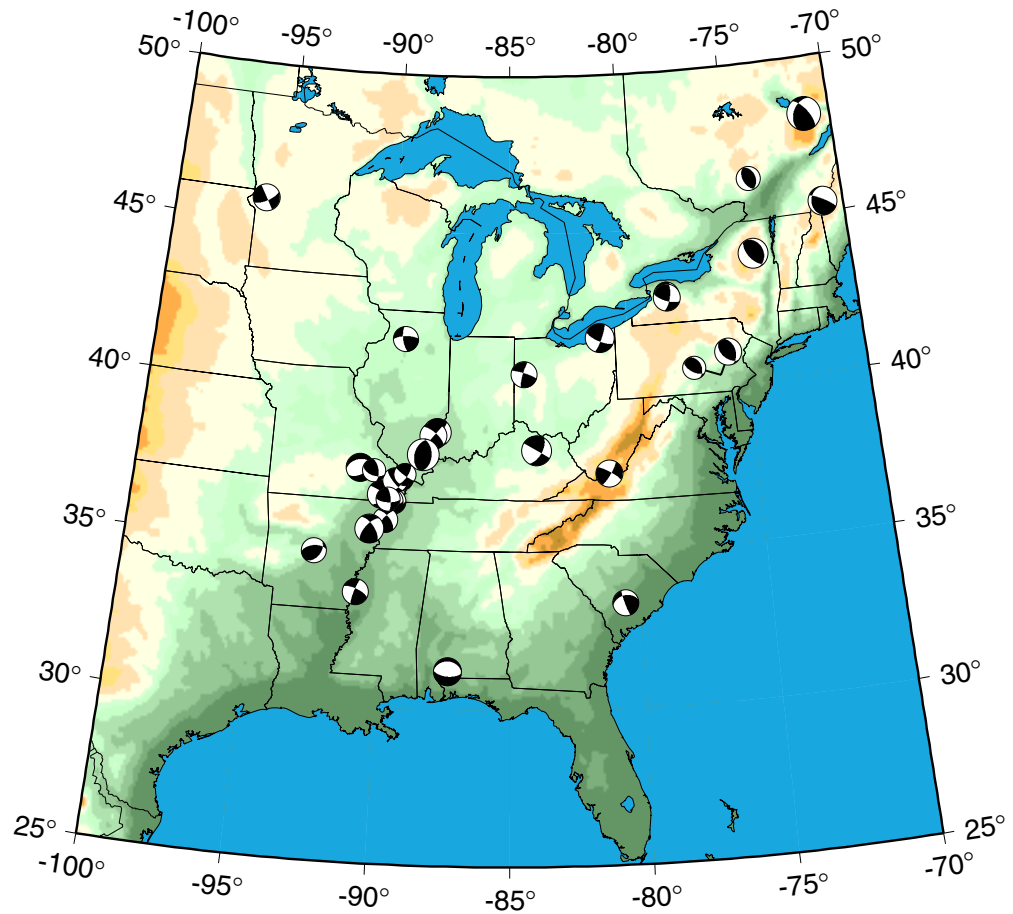


Figure 2.3: Map of central and eastern United States showing focal mechanisms of midplate earthquakes in the area. (From Zoback, 1992, Chang et al., 1998, Ammon et al., 1998).

Earthquakes and Focal Mechanisms						
Date	Location	Latitude (°N)	Longitude (°W)	Strike (N°E)	Dip(°)	Rake (°)
12/27/72	Canada	76.80	106.49	110	83	0
10/05/85	Canada	62.24	124.27	169	32	107
12/23/85	Canada	62.22	124.24	184	21	103
07/05/86	Canada	52.65	118.89	164	36	138
11/25/88	Canada	48.12	71.18	207	41	144
08/19/79	Canada	47.67	69.90	152	43	22
01/09/82	Canada	47.00	66.60	332	49	59
02/18/78	Canada	46.30	74.10	345	39	97
07/09/75	Minnesota	45.70	96.00	60	70	0
06/15/73	Quebec	45.30	70.90	185	23	153
10/07/83	New York	43.94	74.26	342	31	106
06/13/67	New York	42.90	78.20	130	47	37
01/01/66	New York	42.80	78.20	110	70	20
01/31/86	Ohio	41.65	81.16	115	71	10
09/15/72	Illinois	41.60	89.40	170	70	160
07/12/86	Ohio	40.55	84.39	288	80	10
06/10/87	Illinois	38.71	87.95	136	70	15
04/03/74	Illinois	38.60	88.10	310	70	0
07/27/80	Kentucky	38.17	83.91	30	60	180
11/09/68	Illinois	38.00	88.50	195	45	101
10/21/65	Missouri	37.50	91.00	260	40	-71
07/21/67	Missouri	37.50	90.40	107	52	-141
11/20/69	West Virginia	37.40	81.00	32	80	10
08/14/65	Illinois	37.20	89.30	280	70	-20
03/03/63	Missouri	36.70	90.10	220	60	15
02/02/62	Missouri	36.50	89.60	84	55	7
06/13/75	Missouri	36.50	89.70	85	60	-20
3 11/17/70	Arizona	35.90	89.90	319	61	18
03/25/76	Arizona	35.60	90.50	323	63	28
01/01/69	Arizona	34.80	92.60	35	45	54
06/04/67	Mississippi	33.60	90.90	292	70	10
02/03/72	South Carolina	33.31	80.58	259	40	9
10/24/97	Alabama	31.20	87.3	94	62	-90
01/16/94	Pennsylvania	40.30	76.04	135	49	68

Table 2.1: Location and dislocation angles for North American midplate earthquakes (From Zoback, 1992, Chang et al., 1998, Ammon et al., 1998).

stress field and appears to require localized stress anomalies. It is interesting that all five events occurred prior to the establishment of regional seismic networks in 1970, and the focal mechanisms determined are inconsistent with more recent solutions of nearby events. A clear exception is the 1997 southern Alabama event which was shown to be extensional and reflects stress field perturbations near the Gulf Coast (Chang et al., 1998).

As I mentioned above, the source of this broad-scale relatively uniform regional stress could be related to far-field plate-driving forces, but

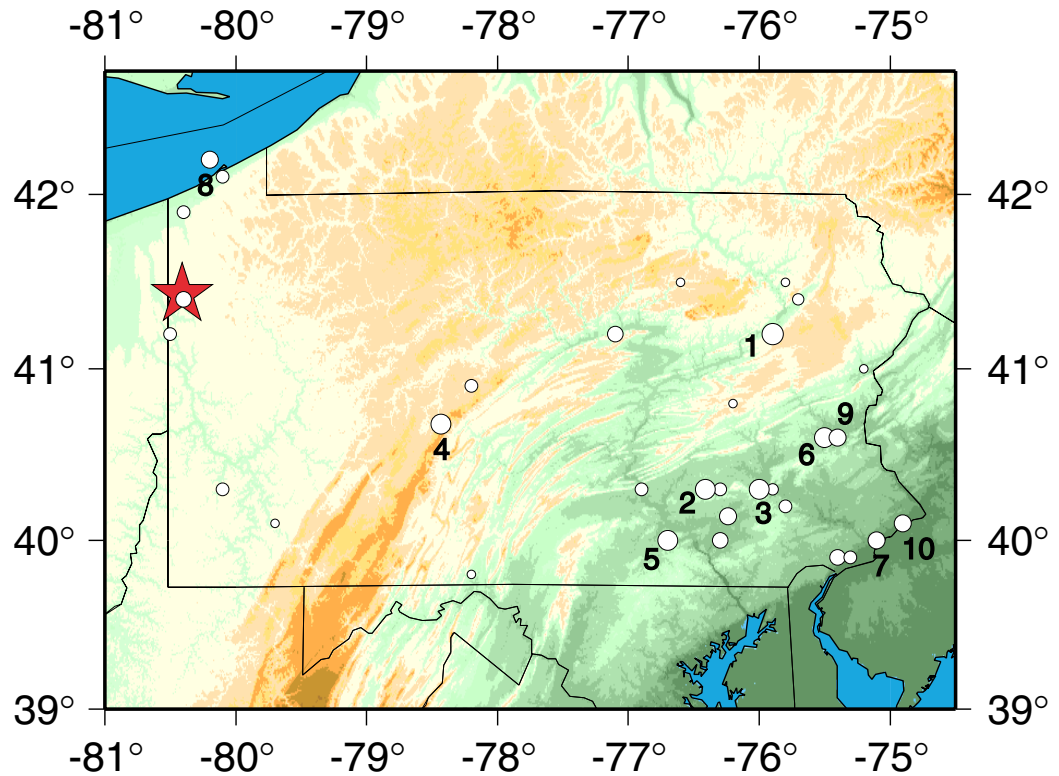
the contrast in southeastern Canada and northeastern United States stress regimes requires a "more local source of lateral variation of relative stress magnitudes" (Zoback, 1992). Several papers proposed the superposition of stresses due to simple flexural models of glacial rebound stresses as an explanation to the observed lateral variation (Talwani and Rajendran, 1991; Evans, 1989). These hypotheses can explain the lateral variation in the regional stress regimes, but the maximum computed changes in stress magnitude due to glacial rebound are quite small (about 10 MPa) (James, 1991; Stein et al., 1979) and unlikely large enough to produce the stress regime changes. On the other hand, rebound related stresses may not be the only force acting to perturb the regional stress field. Additional lateral varying forces may be acting too. One of these other forces, Zoback (1992) said, could be "compressive stresses related to support of a dense lower crustal structure beneath the ancient NE trending rift beneath the St. Lawrence Seaway". This extra force would facilitate the change in the roughly north/south North America stable continental region stress regime.

3. EARTHQUAKES IN PENNSYLVANIA

Although no large earthquakes have occurred in Pennsylvania, the Commonwealth has a long history of felt earthquakes. In this section I summarize the history of activity as documented in several references and in a World Wide Web (WWW) page maintained by Professor Larry Ruff, of the University of Michigan.

More than 60 earthquakes with epicenters in the state of Pennsylvania have been felt since 1737, 55 years after the first permanent settlement was established (see Figure 3.1 for location of some of these historic earthquakes). In addition, several earthquakes located outside Pennsylvania were felt in the state, although most of these earthquakes were felt only locally and have caused no damage or injuries.

Records of earlier earthquakes in the northeastern United States provide limited information on effects on Pennsylvania. A severe earthquake centered in the St. Lawrence River region in 1663 may have been felt in Pennsylvania, but historical accounts are ambiguous. Likewise, a damaging shock at Newbury, Massachusetts, in 1727 probably affected towns in Pennsylvania. A strong earthquake on December 18, 1737, toppled chimneys at New York City and was reported felt at Boston, Massachusetts, Philadelphia, Pennsylvania, and New Castle, Delaware. Other shocks with origins outside the state were felt in 1758, 1783, and 1791. In 1800, two earthquakes (March 17 and November 29) were reported as "severe" at Philadelphia. On November 11 and 14, 1840, earthquakes at Philadel-



	Maximum Intensity	Year	# events
1	VII	1954	2
2	VI	1964	1
3	VI	1954	24
4	VI	1938	1
5	VI	1889	1
6	VI	1908	3
7	V	1840	14
8	V	1934	1
9	V	1961	1
10	V	1961	1

Figure 3.1: Map of Pennsylvania state showing the location of historic earthquakes (white circles) and the Pymatuning event (red star). The numbers indicate the ten earthquakes with highest intensities. The table makes reference to these earthquakes indicating the year of occurrence, the number of earthquakes at each location, and the maximum Modified Mercalli intensity of all the earthquakes located at that geographic position.

phia were accompanied by a great and unusual swell on the Delaware River (von Hake, 1973).

Dishes were thrown from tables (intensity V) at Allentown by a strong shock on May 31, 1884. Thirty towns from Hartford, Connecticut, to West Chester, Pennsylvania, reported fallen bricks and cracked plaster from an earthquake centered near New York City on August 10, 1884. At York, a tremor was felt on March 8, 1889. The earthquake knocked down chimneys, bounced articles from shelves, and threw a man off a sofa. People reported that a "ball of fire" passed over the area at the time the shock occurred (Stover and Coffman, 1993). The intensity was estimated at VI. Another extremely local earthquake of intensity VI, on May 31, 1908, at Allentown (150 km north of Philadelphia) shook down a few chimneys and knocked down a few people. Because this area is known for its limestone, the shock may have been due to a rockfall in a subterranean cavern (Coffman et al., 1982). The disturbance was not felt over more than 150 square kilometers.

On October 29, 1934, a shock of intensity V was felt at Erie (von Hake, 1973). Buildings swayed, people left theaters, and dishes were thrown from cupboards. Another shock with very localized effects occurred in southern Blair County on July 15, 1938. Dishes broke and plaster fell (VI) at Henrietta and Clover Creek, south of Altoona. Wells were affected in Clover Creek Valley.

The area around Sinking Spring, Berks County, experienced minor damage from an earthquake on January 7, 1954. Coal-mining operations may have caused this tremor, which was intensity VI. Plaster was torn from ceilings and walls, dishes and bottles tumbled from shelves, windows

were broken and furniture was upset. Other slight damage to several brick and frame buildings was reported. Light aftershocks occurred during the rest of the month.

A local disturbance probably caused by subsidence of an underground coal mine caused damage estimated at \$1 million in a five-block residential area of Wilkes-Barre on February 21, 1954 (Stover and Coffman, 1993). Hundreds of homes were damaged, ceilings and cellar walls split and backyard fences fell over, sidewalks were pushed sharply upward and then collapsed. Gas and water mains snapped; methane rising from cracks in the earth created a temporary emergency. Two days later (February 23), a second disturbance was reported from the same section of Wilkes-Barre. More cracks appeared in ceilings and walls of apartment buildings. Curbs pulled away from sidewalks, and street pavements buckled. Additional water and gas mains were broken.

On September 14, 1961, a moderate earthquake that was centered in the Lehigh Valley shook buildings over a broad area and alarmed many residents (von Hake, 1973). There was only one report of damage - loose bricks fell from a chimney at Allentown (V). However police and newspaper throughout the area were overwhelmed with calls.

A similar disturbance occurred on December 27, 1961, in the northeast portion and suburbs of Philadelphia. Buildings shook, dishes broke, and other objects were disturbed. Police and newspaper offices received many calls from alarmed citizens inquiring about the loud rumbling sounds (V).

A strong local shock cracked wall and caused some plaster to fall (VI) at Cornwall, on May 12, 1964. Slight landslides were reported in the area. In one building, a radio was knocked from a table and a wall mirror moved

horizontally. Workers in an iron mine were alarmed by a "quite severe jarring motion".

A small earthquake whose epicenter was in New Jersey caused intensity V effects at Darby and Philadelphia. The December 10, 1968, shock was measured at magnitude 2.5. Although relatively small, it broke windows at a number of places in New Jersey.

On December 7, 1972, slight damage (V) was reported at New Holland. In addition, Akron, Penryn, and Talmage experienced intensity V effects. The total area covered approximately 1200 square kilometers of Berks and Lancaster Counties.

An intensity VI shock was reported on April 23, 1984 near Marticville, Lancaster County. It caused minor damage at Conestoga, where a garage shifted 1.3 cm off its foundation, plaster fell from ceilings, and cracks formed in windows and concrete basement walls. One foreshock occurred 5 days earlier and many slight aftershocks occurred.

In the last years, the largest earthquake in the region was the magnitude 5.0 Leroy (northeastern Ohio) earthquake that occurred on January 31, 1986, about 65 km west-northwest of the Pymatuning shock. This event caused minor property damage in several towns in northeast Ohio and northwest Pennsylvania. Seventeen people were injured in the epicentral area. Damage to buildings include fallen tiles and plaster, cracked chimneys and exterior walls, and broken windows. Hydrologic effects were observed and in more than a dozen wells east of Cleveland, changes in the water flow were reported (Stover and Coffman, 1993). On January 1994, two events, a foreshock (M_W 4.0) followed by an M_W 4.6 mainshock occurred near Wyomissing, Pennsylvania.

The origins of these Pennsylvania earthquakes, as with earthquakes in central and eastern United States, are poorly understood. Earthquakes in southeastern Pennsylvania correlate with the northern and southern margins of the Triassic rift basin (Newark-Gettysburg Basin). This is consistent with the worldwide observation that earthquakes in stable continental regions most often occur in crust that has experienced extension (Johnston and Kanter, 1990): faults created in continental crust by ancient extensional stresses may lie dormant for many millions of years, accumulating a blanket of sediments; later, the compressive stresses within continental interiors may reactivate a fault, which slips and generates an earthquake.

Southeast Pennsylvania earthquakes are generated on reactivated Mesozoic faults which extend away from the margins of the basin into the surrounding Paleozoic rocks. These zones are characterized by deep buried and poorly known faults, some of which serve as the sites for periodic release of strain, and few correlations can be made between epicenters and specific mapped faults. A possible exception is the north striking Fruitville Fault in central Lancaster County. Epicenters of October 6, 1978, and March 11, 1995 earthquakes are located close to the surface expression of this fault. Epicenters in the Conestoga-Marticville area of southern Lancaster County and in Cornwall area of Lebanon County are located at hypothetical extensions of the Fruitville Fault, although geological observations are lacking.

The epicenters in Susquehanna, Blair, Centre, and Somerset counties are along the Allegheny Front, which may reflect an antecedent tectonic feature, possibly the Iapetan rift margin of Laurentia. Epicenters in north-

western Pennsylvania appear to represent a westward extension of the western New York seismic zone, which may be an extension of the zone of seismicity along the Lawrence Paleozoic rift. Thus, all Pennsylvania seismic activity may be caused by reactivation of faults associated with crust that experienced Paleozoic or Mesozoic rifting.

4. THE PYMATUNING EARTHQUAKE

4.1 GENERAL DESCRIPTION

On Friday, September 25, 1998, at 19:52:52 UTC an earthquake occurred in Northwestern Pennsylvania. The earthquake epicenter was located by the National Earthquake Information Center (NEIC) at 41.5° N, 80.4° W, near the Crawford County community of Greenville, close to the Ohio-Pennsylvania border and near the south end of Pymatuning Lake. The earthquake was felt throughout northern Ohio, western Pennsylvania, and New York, and much of southern Ontario, Canada, covering an area of approximately 200,000 square kilometers. Also felt in some locations as far west as Illinois and Wisconsin, and as far east as New Jersey, Connecticut, and the District of Columbia, and as far south as Kentucky and Virginia. This earthquake is significant for two reasons. First, its magnitude ($m_{bLg} = 5.2$) is the highest for any previous Pennsylvania earthquake. Second, it occurred in an area that only rarely experiences such events. Most prior Pennsylvania earthquakes of moderate magnitude have occurred in or near Lancaster County in southeastern Pennsylvania.

The largest, recent previous earthquake in the region was the magnitude (m_b) 5.0 Leroy (northeastern Ohio) earthquake that occurred on January 31, 1986, about 65 km west-northwest of the Pymatuning shock. The major double couple planes of this Ohio earthquake strike 115° N and 22° N, with dips of 71° and 81° , and rakes of 10° and 161° . Three prior earthquakes occurred in the same epicentral area with magnitudes greater than

3.0. Two were instrumentally located near Pymatuning earthquake, and the third event in 1852 is assumed to have occurred 20-30 km to the north-east.

Like most of the seismicity east of the Rocky Mountains, earthquakes in the region occur along preexisting zones of weakness in Precambrian rocks. Wegweisser et al. (1998) suggested that seismicity in NW Pennsylvania may be associated with the NW trending "cross-strike discontinuities" that are recognized in the Paleozoic rocks and may represent reactivation of faults in the Precambrian basement. Alexandrowicz and Cole (1999) found evidence of preexisting NW striking faults in the epicentral region of the Pymatuning shock.

4.2 INTENSITY OF THE EARTHQUAKE

Much of the information that I summarize in this section is available on line (see bibliography for electronic addresses) in the WWW pages maintained by Dr. Ed Cranswick of the US Geological Survey (even if these electronic addresses will eventually expire, I want to give credit to the authors and contributors for their labor). A number of institutions participated in the collection of intensity information on the Pymatuning earthquake (including the US Geological Survey, University of Memphis, and Saint Louis University). The results were nicely compiled by USGS and Memphis researchers.

An earthquake intensity represents the level of ground shaking as measured by consideration of the effects of the earthquake on people, on buildings and other human-made structures, on building contents, and on the

landscape. The Modified Mercalli Intensity Scale consists of a description of earthquake effects ranging from I, "Not felt except by a very few under especially favorable circumstances", to XII, "Total damage". The maximum intensity of the Pymatuning earthquake was VI, "Felt by all. Many frightened and run outdoors. Persons made to move unsteadily. Broke dishes, glassware, in considerable quantity, also some windows. Fall of knickknacks, books, pictures. Overturned furniture in many instances. Some heavy furniture moved; a few instances of fallen plaster or damaged chimneys. Slight damage". This maximum intensity of VI was for communities near the epicenter and for several additional communities in Pennsylvania and Ohio (see Figure 4.1 from Armbruster J., Barton H., Bodin P., Buckwalter T., Cox J., Cranswick E., Dewey J., Fleeger G., Hopper M., Horton S., Hoskins D., Kilb D., Maramonte M., Metzger A., Risser D., Seeber L., Shedlock H., Stanley K., Withers M., and Zirbes M.).

In Greenville, the earthquake was felt by everyone. Damage reports described large cracks in the exterior walls of some buildings, cracked windows, cracked chimneys with lost of bricks, and loss of power in a factory as a consequence of the damage caused to a transformer. In some houses many items fell from shelves and items were shaken off store shelves. One person was injured from being thrown to the ground.

In Jamestown, ceiling tiles fell throughout the elementary school and windows were broken. A few old chimneys cracked or lost bricks. Exterior buildings walls sustained large cracks, interior walls sustained a few large cracks, and plaster fell. Many small objects overturned and fell, the suspended ones swung violently, and in some houses many items were shaken off store shelves, several dinnerware items broke, and hanging pic-

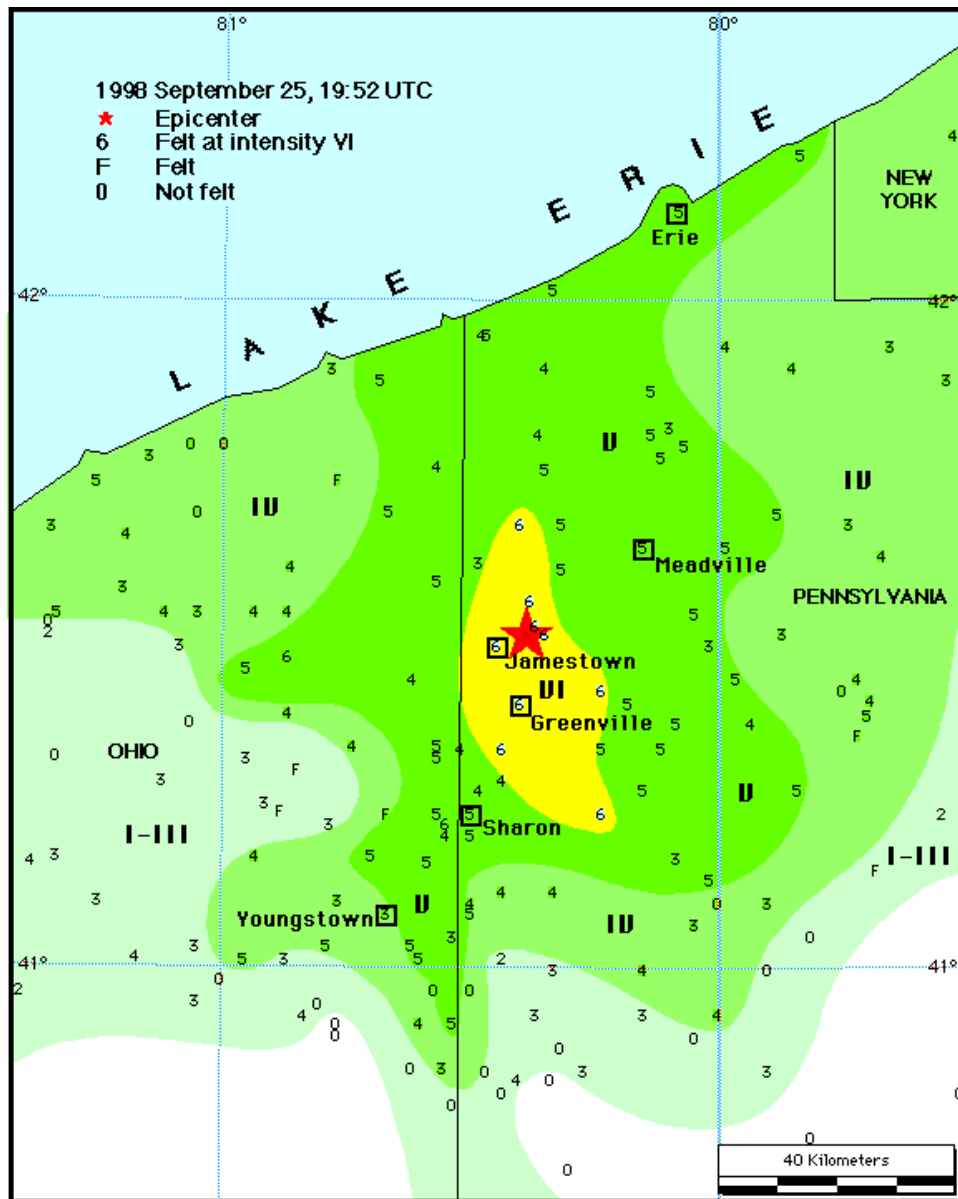


Figure 4.1: Map showing intensities in the region near the epicenter which is represented by a star. (From Armbruster J., Barton H., Bodin P., Buckwalter T., Cox J., Cranswick E., Dewey J., Fleegeer G., Hopper M., Horton S., Hoskins D., Kilb D., Maramonte M., Metzger A., Risser D., Seeber L., Shedlock H., Stanley K., Withers M., and Zirbes M.).

tures fell. The earthquake was also felt by everyone in Jamestown and many people run out of the buildings (USGS report).

4.3 HYDROLOGIC EFFECTS

An interesting and often overlooked consequence of moderate earthquakes are hydrologic effects. Researchers at the US Geological Survey investigated and summarized the hydrologic changes produced by the Pyramuning earthquake. The following section is a review of material available online at WWW sites maintained by the US Geological Survey.

Since the time of the earthquake, September 25, 1998, numerous residents of the area have reported hydrologic changes that might be related to the earthquake. These changes include water wells becoming dry (the maximum measurement water level decline was more than 30 m), new flowing artesian wells, formation of new springs, and changes in well-water quality (black water and sulfur). These hydrologic changes are nearly identical to those reported by residents of northeastern Ohio after the earthquake in 1986 (according to USGS hydrologist in Ohio).

Shallow groundwater in the Mercer, Pennsylvania, is described by Poth (1963) as circulating in a series of "hydrologic islands". The nature of the bedrock surface of the Mercer has resulted in ridges, surrounded by valleys containing perennial streams. These ridges constitute the "hydrologic islands". A shallow, local groundwater flow system operates within each "hydrologic island" and is hydrologically isolated from the local groundwater flow systems in adjacent islands. Most ground water in the ridge is stored and transmitted via bedrock fractures and bedding plane

partings. Most recharge to these "hydrologic islands" discharges the surrounding valleys; a small amount recharges deeper flow systems.

Shallow wells on the highest points of the ridge went dry as soon as the morning after the earthquake. Deeper wells on the ridge, and wells along the flanks of the ridges went dry in the posterior weeks. Some of the wells that went dry were deepened obtaining good results, but, within a month, they went dry again. On the other hand, within several days after the earthquake, there were springs, wells, ponds, and streams that increased flow or began new discharges. These are located on the discharge areas: the lower slopes of the ridge and bordering stream valleys. One of the USGS observation wells located in a valley recorded a 1 m rise in the groundwater level after the earthquake (see figure 4.2).

The Pymatuning hydrologic effects can be explaining considering that the earthquake created new fractures, or opened old fractures, through low permeability zones (aquitards) beneath the upper aquifer(s). The newly opened fractures increased the downward hydraulic conductivity through the aquitard, increasing the downward movement of groundwater and creating a zone of water table depression along the fracture(s). Shallow wells near the fracture(s) would have gone dry pretty soon, and as the water table continued to lower, deeper wells would have started to go dry. A consequence of the increased downward movement of groundwater in the recharge area would be an increase in discharge from new springs and flowing wells in the low-lying discharge area and to deeper flow systems.

So, although the Pymatuning earthquake did not produce a high level of damage to buildings and other human-made structures, the hydrologic effects were a costly result of the event.

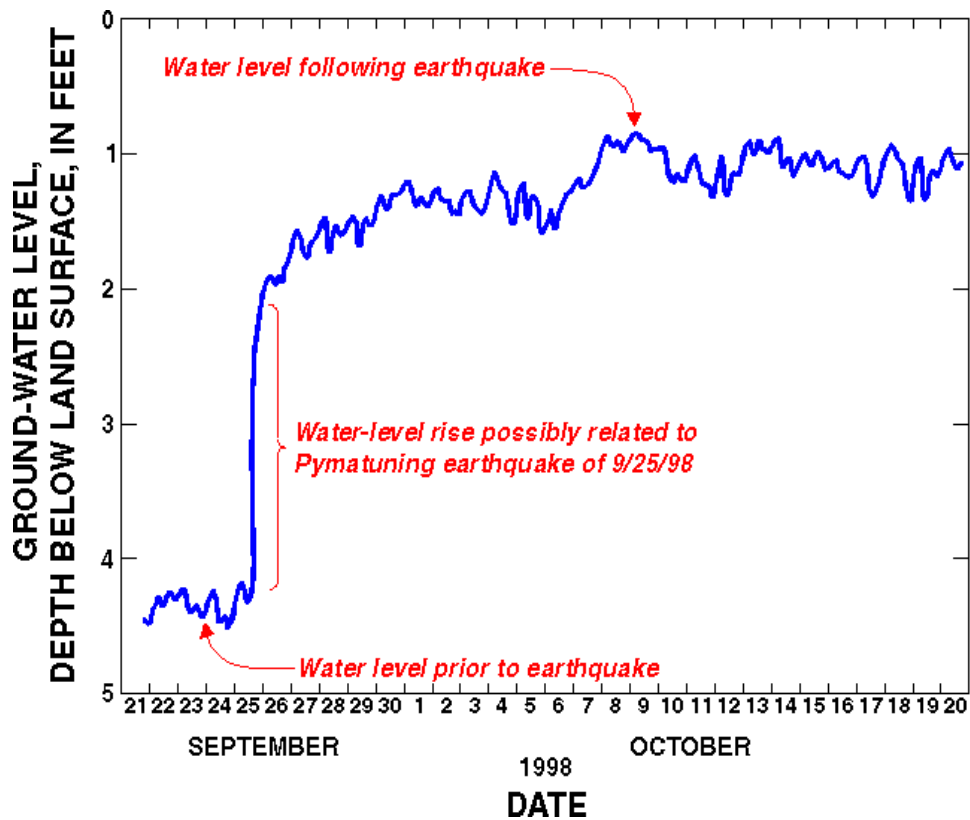


Figure 4.2: Increase in the groundwater level of one of the USGS observation well located in a valley adjacent to the "hydrologic island". (From Armbruster J., Barton H., Bodin P., Buckwalter T., Cox J., Cranswick E., Dewey J., Fleeger G., Hopper M., Horton S., Hoskins D., Kilb D., Maramonte M., Metzger A., Risser D., Seeber L., Shedlock H., Stanley K., Withers M., and Zirbes M. (USGS)).

5. SEISMIC OBSERVATIONS OF THE PYMATUNING EARTHQUAKE

The September 25, 1998, Pymatuning earthquake was well recorded by the US and Canadian National Seismic Networks. I examined waveforms recorded by 43 stations from these two seismic networks. Thirty-one of these stations are part of the US National Seismic Network (USNSN), a three-component, broad-band seismic network; the other twelve are components of the Canadian National Seismic Network (CNSN) which has similar instrumentation. The station distribution (epicentral distance and azimuth) is well suited for a source analysis (Figure 5.1 and Table 5.1)

To estimate the depth, fault geometry, and slip orientation for the Pymatuning event, I first modeled the observed seismic waveforms from the closest stations to the event using a least-square time-domain moment tensor inversion. To test the robustness of these results, I performed an L1 norm moment tensor inversion. I also used a grid search to fit the observed seismograms with a pure double couple. These results are discussed later.

5.1 ANALYSIS OF THE OBSERVATIONS

Initial analyses of the seismic waveforms generated by the September 25, 1998 Pymatuning earthquake suggested an unusual, non double-couple component to the faulting mechanism (Ammon, personal communication, 1998, G. Ekstrom, personal communication, 1998). The results

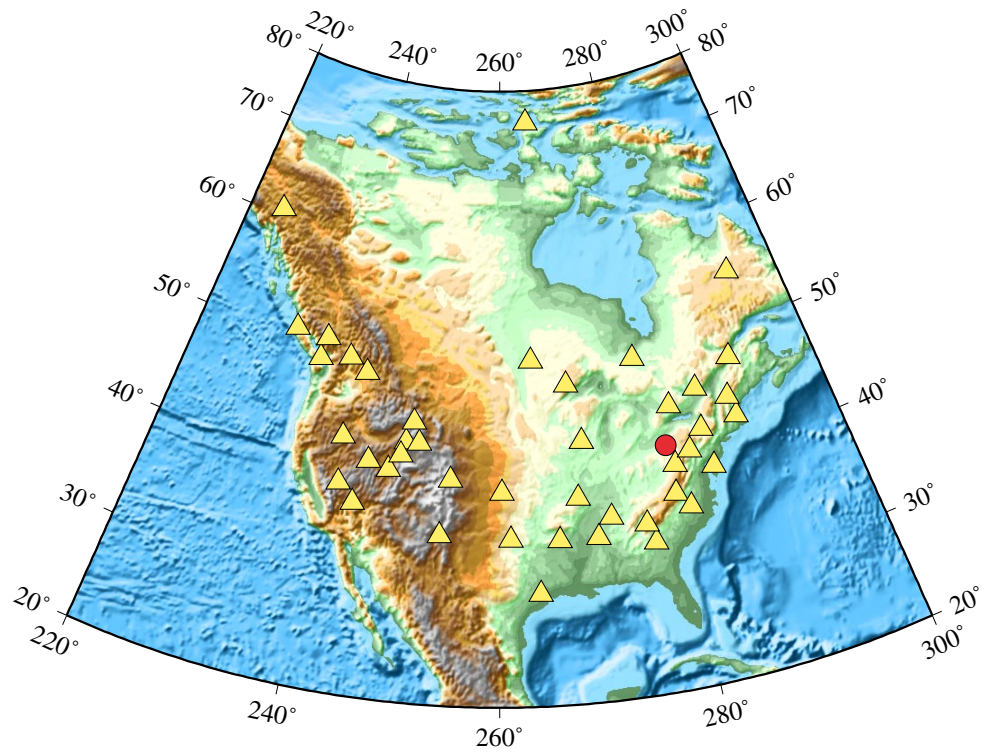


Figure 5.1: Map of North America showing the earthquake (red circle) and stations (yellow triangles) used in this study.

Sites description					
Station ID	Network	Latitude (°N)	Longitude (°W)	Azimuth (°)	Distance (km)
AHID	USNSN	42.765	111.100	284	2522
ALQ	USNSN	34.943	106.457	261	2377
BINY	USNSN	42.199	75.986	76	382
BLA	USNSN	37.211	80.421	179	473
BW06	USNSN	42.778	109.556	283	2397
CBKS	USNSN	38.814	99.737	266	1664
CCM	USNSN	38.056	91.245	251	996
CEH	USNSN	35.891	79.093	169	631
DUG	USNSN	40.195	112.813	278	2715
ELK	USNSN	40.745	115.239	280	2901
EYMN	USNSN	47.946	91.495	313	1129
GAC	CNSN	45.703	75.478	387	622
GOGA	USNSN	33.411	83.467	197	932
GWDE	USNSN	38.826	75.617	124	508
HKT	USNSN	29.950	95.833	232	1882
HRV	USNSN	42.506	71.558	78	748
HWUT	USNSN	41.607	111.565	281	2580
ISCO	USNSN	39.800	105.613	273	2127
JFWS	USNSN	42.915	90.249	284	822
KAPO	CNSN	49.450	82.508	351	904
LBNH	USNSN	44.240	71.926	63	763
LKWY	USNSN	44.565	110.400	288	2449
LMQ	CNSN	47.548	70.327	46	1053
MCWV	USNSN	39.658	79.846	165	208
MIAR	USNSN	34.546	93.573	240	1381
MNV	USNSN	38.433	118.153	277	3211
MYNC	USNSN	35.074	84.128	205	778
NEW	USNSN	48.263	117.120	297	2962
OXF	USNSN	34.512	89.409	228	1100
PGC	CNSN	48.650	123.451	298	3430
PHC	CNSN	50.707	127.432	302	3707
PMB	CNSN	50.519	123.076	302	3399
PNT	CNSN	49.317	119.617	300	3149
RES	CNSN	74.687	94.900	353	3775
SADO	CNSN	44.769	79.142	16	385
SCHQ	CNSN	54.832	66.834	29	1795
SSPA	USNSN	40.636	77.888	112	237
TPNV	USNSN	36.929	116.224	273	3106
ULM	CNSN	50.250	95.875	315	1540
WHY	CNSN	60.660	134.881	319	4207
WMOK	USNSN	34.738	98.781	251	1766
WVOR	USNSN	42.434	118.637	285	3139
WVT	USNSN	36.130	87.830	229	871

Table 5.1: Seismic stations used in the study

from the moment tensor inversion carefully carried out in this study, corroborate those initial results. Preliminary near real-time studies that constrained the source to be a double-couple, also suggested that the large size of the non double-couple component may have been an artifact caused by the available data coverage (Ammon, personal communication).

An important part of investigating the significance and cause of the non double-couple source is a careful examination of the observations. Although in this case corrupt data are not the cause of the source complexity, a number of interesting observations on instrument performance in the national seismic networks are possible. In this section I summarize specific “problems” that I found while I was working with the data.

USNSN Data: The epicentral distance of these stations varies from 208 to 3211 km away from the source, and the azimuth range is between 63° and 229° . Only five of these stations (BINY, BLA, MCWV, SADO, SSPA) were closer than 500 km, and ten stations were between 500 and 1000 km away from the source (see Table 5.1).

However, I could not use all of the three components from each of these 15 stations. As expected, many distant stations had low signal-to-noise ratios. The radial component of GOGA was not used, the same problem appears in the radial component of JFWS because the east component is too noisy (although the Love waves are well recorded on the north component). Several stations (CEH, MIAR, TPNV, WVOR), present problems with horizontal components often resulting in identical radial and transverse components, which were not used in further analysis.

5.1.1 ELECTRONIC SATURATION

The vertical component of BINY was not used because of instrument problems apparent in original signals. The raw vertical (velocity) component seismogram and its derivative and integral are shown in Figure 5.2. Careful examination of the velocity trace reveals a nonlinear component to the signal that begins soon after the large amplitude S-waves arrive at the station. Specifically, soon after the S-arrival, a broad trough initiates and continues for at least another minute. Similar problems were observed at stations BLA and GAC, which were also located relatively close to the source (see Figures 5.3 and 5.4).

The stations exhibiting nonlinearity are listed in Table 5.2. The cause of the signals is uncertain and difficult to pin down without detailed instrument information. The initiation of the problematic response with the large-amplitude S-waves suggests that the problem may have been electronic saturation. However, the original signals do not show clear evidence of clipping, only the broad nonlinear signal. The potential problems associated with the clipping could have important consequences on the performance of the national networks in the event of a large earthquake in the east. If clipping is common for a few hundred kilometers for a magnitude five, the problems will be exacerbated for a larger event. Having little useful near-field data from the next large eastern North American earthquake could be troublesome, since such events are uncommon.

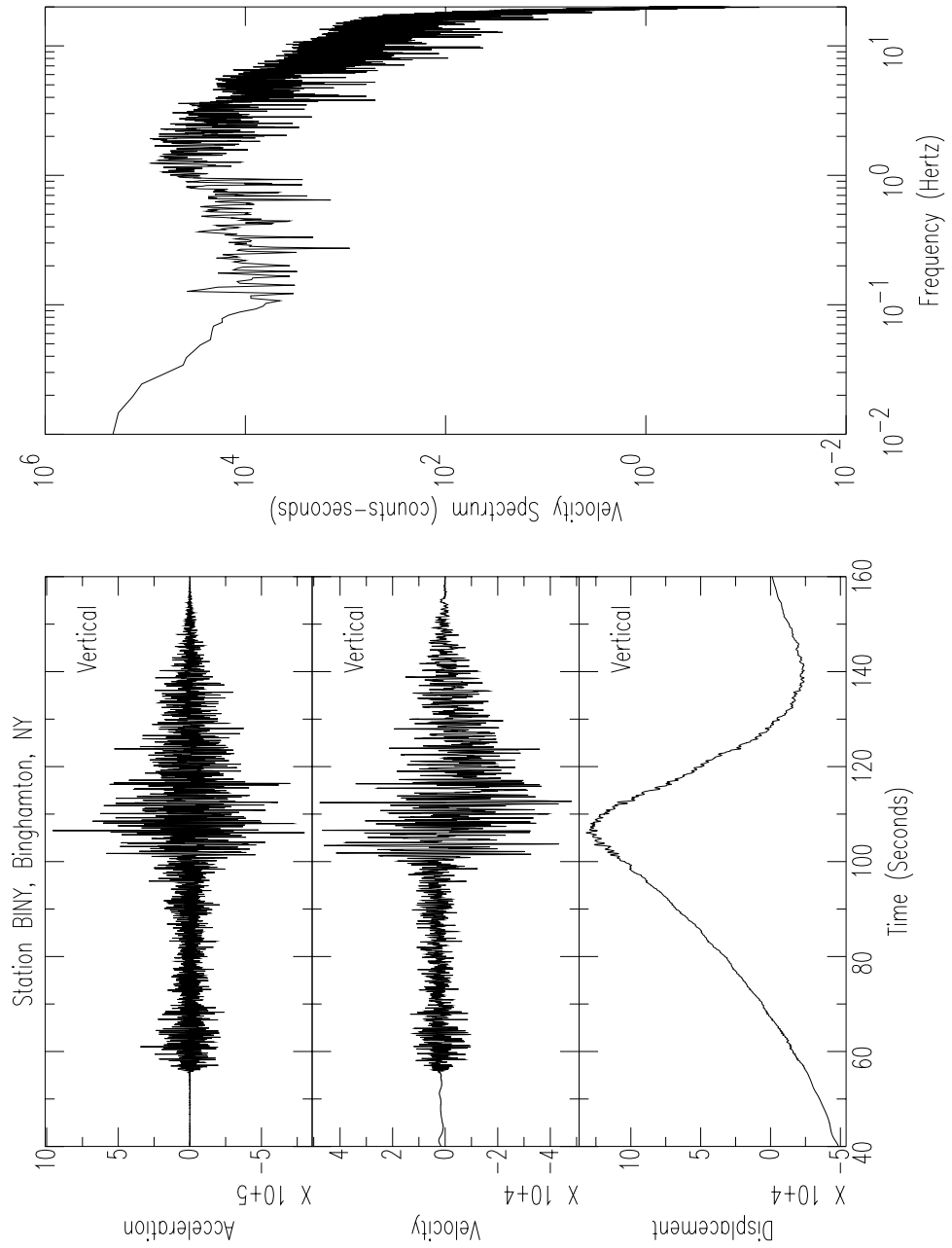


Figure 5.2: Raw vertical (velocity) component seismogram and its derivative and its integral from station BINY, Binghamton, NY.

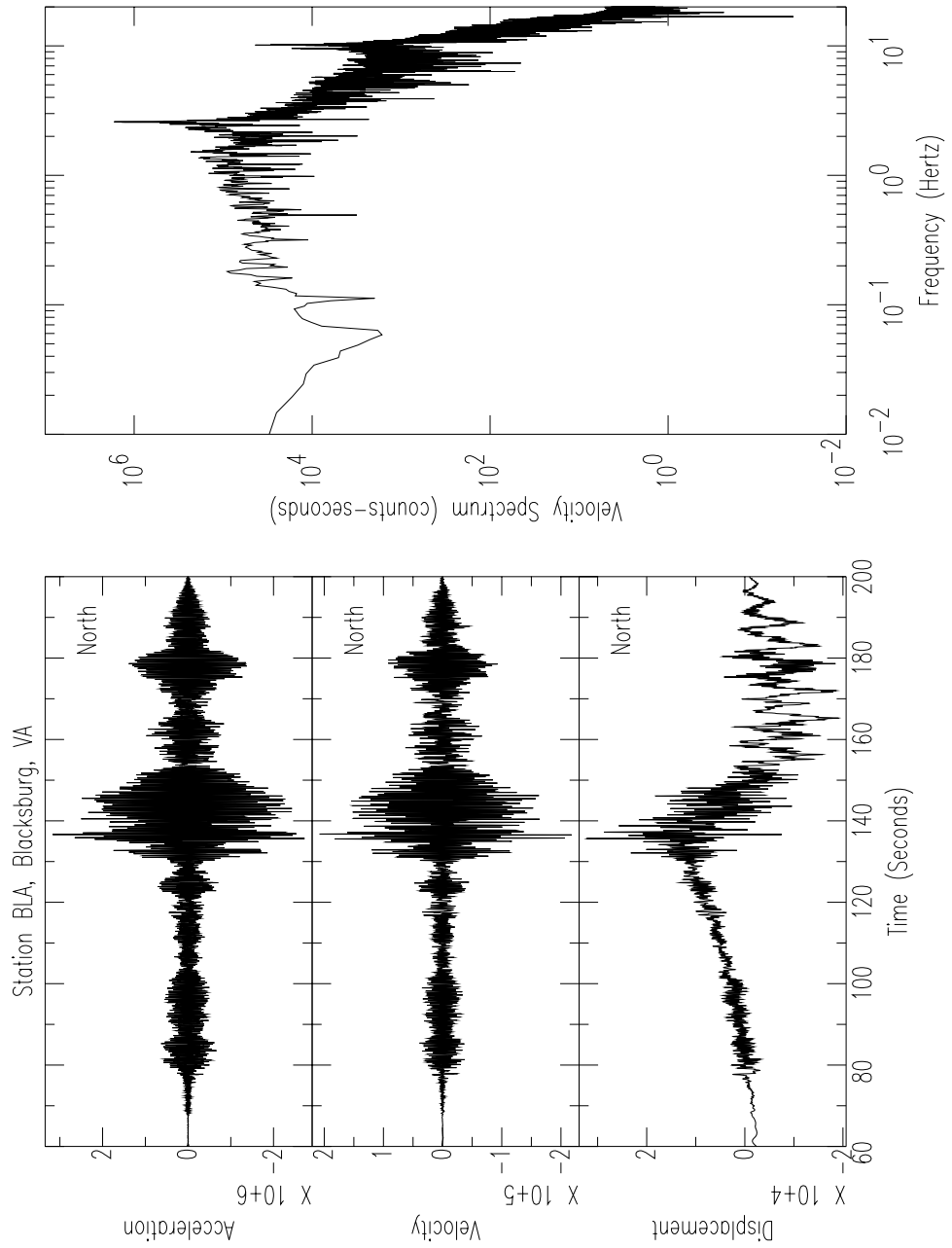


Figure 5.3: Raw vertical (velocity) component seismogram and its derivative and its integral from station BLA, Blacksburg, VA.

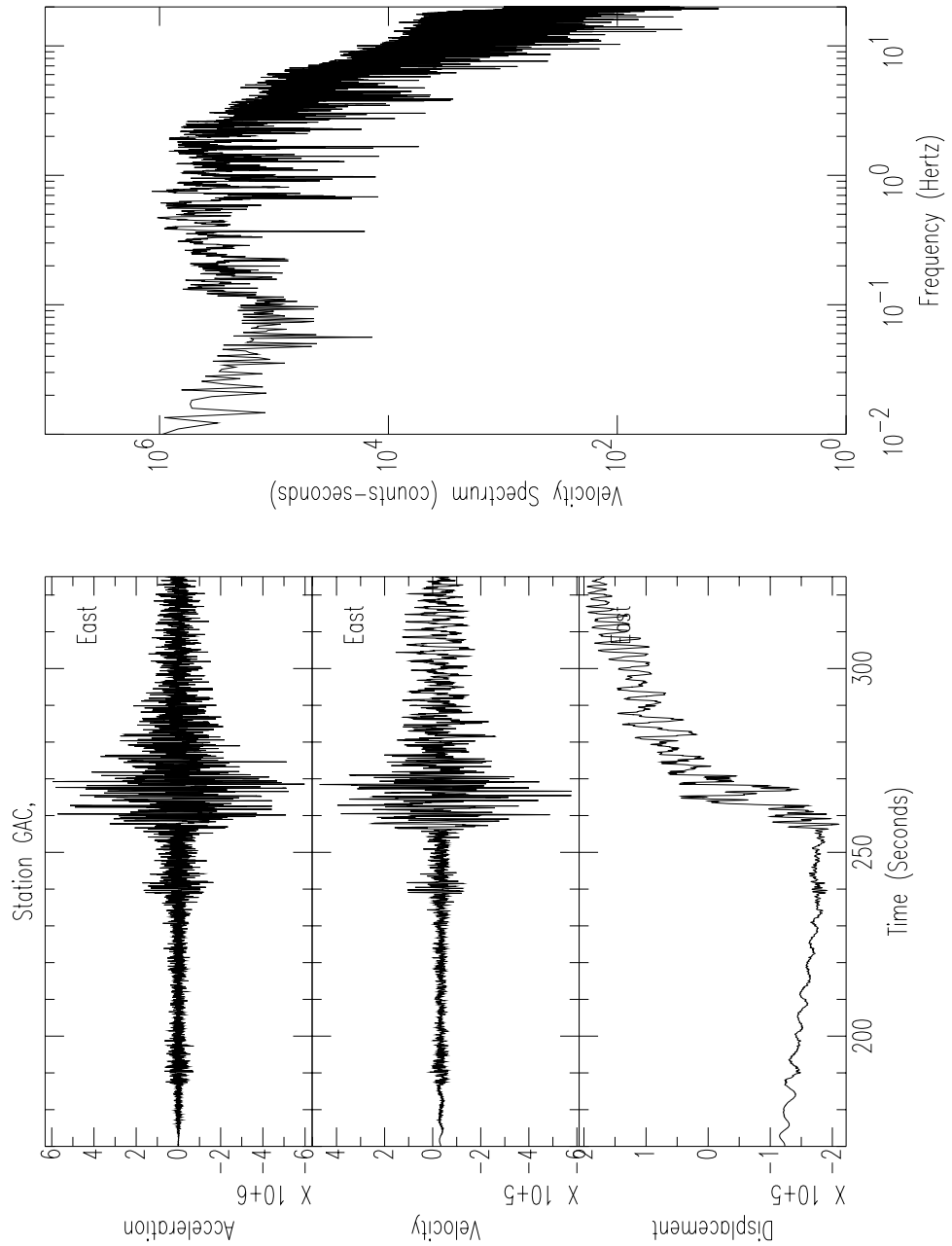


Figure 5.4: Raw vertical (velocity) component seismogram and its derivative and its integral from station GAC.

Stations with Nonlinear Instrument Problems			
Station ID	Distance (km)	Peak Velocity	Peak Acceleration
BINY	382	7.74e4	1.23e6
BLA	473	2.07e5	3.16e6
GAC	622	4.70e5	6.47e6
MYNC	778	1.91e4	2.52e5
OXF	1100	4.29e4	3.59e5

Table 5.2: Stations with nonlinear instrument problems. The peak velocity is in counts/s and the units of the peak acceleration are counts/s².

5.1.2 GWDE - POLARITY REVERSAL

Initial rotation of the horizontal seismograms recorded at station GWDE indicated a problem. The transverse seismogram correlated better with the vertical than did the radial. The problem was fixed if the east component's polarity was reversal. Analysis of a teleseismic P-wave confirmed the polarity reversal, so I changed the polarity of the east component and I proceeded as usual. The revised data are completely consistent with other observations.

Several stations (CEH, MIAR, TPNV, WVOR), present problems with horizontal components often resulting in identical radial and transverse components, which were not used in further analysis.

CNSN Data: The epicentral distance varies from 385 to 4207 km away from the source, and the azimuth range varies between 16° and 353°. Again, very distant stations had low signal-to-noise ratios and would have been difficult to fit without very accurate earth models. Only one station of the twelve considered is closer than 500 km (SADO) (see Table 5.1). Two more

stations have epicentral distances less than 1000 km, GAC and KAPO. Unfortunately, GAC suffered non-linearity instrument problems (see Figure 5.4), so it was excluded from the inversion.

6. TIME-DOMAIN MOMENT TENSOR ESTIMATION

Waveform modeling has become one of the most powerful tools for understanding fault rupture processes and the design of Earth models. In this study I use waveform modeling to recover the source parameters (source depth, time function, fault orientation, and seismic moment) by directly fitting observed seismograms with synthetic seismograms.

The mathematical theory underlying this technique is linear filter theory. A seismogram is treated as the output of a sequence of linear filters where each filter accounts for some aspect of the seismic source or propagation. The ideas are nicely reviewed in Lay and Wallace (1995); I summarized them in the discussion below.

It's well accepted that an observed seismogram, $u(t)$, can be represented as following:

$$u(t) = s(t) \star g(t) \star i(t) \tag{6.1}$$

where $s(t)$ is the signal from the seismic source, $g(t)$ is the earth structure operator, $i(t)$ is the seismometer response, and \star represents convolution. The $s(t)$ and $g(t)$ operators can be divided into several filters to account for specific effects. For instance, $s(t)$ can be divided into filters accounting for source radiation conditions and fault rupture characteristics. The most complex of these filters is $g(t)$, the earth transfer function, that formally includes all elastic and attenuation effects of earth structure.

Equation 6.1 can be rewritten (Langston, 1981; Lay and Wallace, 1995) as:

$$u_n(x, t) = s(t) \star i(t) \sum_{i=1}^5 (m_i \cdot G_{in}(t)) \quad (6.2)$$

where $m_1 = M_{11}$, $m_2 = M_{22}$, $m_3 = M_{12}$, $m_4 = M_{13}$, $m_5 = M_{23}$

and where u_n is the vertical, radial, or tangential displacement, and the Earth transfer function has been replaced by the summation of the product of the seismic moment tensor, m_i , and the corresponding Green's functions. This implies that any Earth transfer function can be represented as a linear combination of Green's functions.

Equation 6.2 is a powerful representation of a seismic waveform because it requires the calculation of only five (or with some recombination of terms, four) fundamental Green's functions to produce a synthetic waveform for an arbitrary moment tensor at a given distance (Lay and Wallace, 1995). The same equation is also the basis for inversion procedures to recover the seismic source parameters.

Assuming that we know the source time function and source depth, and since $i(t)$, the instrument response, is usually well known, then these two operators ($s(t)$ and $i(t)$) can be convolved directly with the Green's functions, and we can write

$$u = G m \quad (6.3)$$

where G is a matrix that contains the Green's functions (after convolution), u is a vector that contains the observed seismogram, and m is a vector that contains the unknown moment tensor.

In order to solve equations of the form of (6.3) Lanczos (1961) introduced a least-square solution for an estimate of m , which is minimal length and minimizes the L_2 norm $(u-Gm)^T(u-Gm)$. The solution is formed by summing eigenvectors of $G^T G$ and is called the "generalized inverse" estimate. We can also solve equation (6.3) by minimizing an L_1 norm, $\sum |u_i - Gm|$, which is less sensitive to outliers.

The power of waveform modeling for determining seismic source parameters by equation 6.3 depends on our ability to calculate suitable Green's functions. At teleseismic distances ($30^\circ - 90^\circ$) this is usually not a problem because the P and SH waves have simple structural interactions and travel mostly in the lower mantle where the velocity structure is smooth. At regional distances, the modeling is more difficult. However, as long as parameters such as crustal thickness, average crustal seismic velocities, and upper mantle Pn velocity are well approximated, the inversion for source parameters is often possible.

The procedure, for each inversion, is as follows: first, calculation of "fundamental fault" Green's functions for each station with observations. Second, because we do not know the depth of the event and the source time function *a priori*, an inversion is performed over a range of depths including the source time function as an unknown along with the moment tensor. The preferred depth is that with the best fit to observations. In general, simultaneous inversion for the moment tensor and source time function results in some trade-offs. For instance, a longer source time function at a shallower depth can produce the same effect as a shorter time function at a deeper depth. Therefore, the solution is not unique.

The moment tensors obtained from waveform inversion seldom cor-

respond to “perfect” double couples, but are usually decomposed into a major and a minor double couple, or into a major double couple and a CLVD (Compensated Linear Vector Dipole) (Lay and Wallace, 1995). Geological interpretation of non double couple components can be difficult (Julian, 1998; Frohlich and Apperson, 1992)

6.1 THE PYMATUNING EVENT MOMENT-TENSOR

Regional distance analysis is extremely important in the study of small or moderate-sized earthquakes ($m_b \leq 5.5$), which are rarely well recorded at teleseismic distances (e.g. Dreger and Helmberger, 1990, Dreger et al., 1995, Romanowicz et al., 1993, Ammon et al., 1998). The September 25, 1998, Pymatuning earthquake had a m_b of 5.2, so to estimate the moment tensor of this event I modeled the complete waveforms recorded at the closest stations in the period range between 50 and 10 seconds (see Table 6.1), depending on the epicentral distance of the different stations.

I used complete synthetic seismograms calculated using Kennett’s (1983) reflection-matrix method as implemented by G. E. Randall (personal communication). Before the inversion, I aligned the observed and the synthetics on the first P arrival time to minimize dependence on structure. Alignment reduces problems with location, origin-time uncertainty, and absolute velocity differences between the earth and the chosen velocity model (Ammon et al., 1998). Also, prior to inversion, the observations and the synthetics were filtered to include periods longer than 10 seconds and shorter than 50 seconds.

The moment tensor inversion is outlined by Langston (1981) and was

Weight and Bandwidth			
Station ID	Component	Weight	Bandwidth (Hz)
BINY	Vertical	0.0	0.02-0.1
BINY	Radial	1.0	0.02-0.1
BINY	Transverse	1.0	0.02-0.1
BLA	Vertical	1.0	0.02-0.1
BLA	Radial	0.0	0.02-0.1
BLA	Transverse	1.0	0.02-0.1
GWDE	Vertical	1.0	0.02-0.1
GWDE	Radial	1.0	0.02-0.1
GWDE	Transverse	1.0	0.02-0.1
MCWV	Vertical	1.0	0.02-0.1
MCWV	Radial	1.0	0.02-0.1
MCWV	Transverse	1.0	0.02-0.1
SADO	Vertical	1.0	0.02-0.1
SADO	Radial	1.0	0.02-0.1
SADO	Transverse	1.0	0.02-0.1
SSPA	Vertical	1.0	0.02-0.1
SSPA	Radial	1.0	0.02-0.1
SSPA	Transverse	1.0	0.02-0.1
HRV	Vertical	0.5	0.02-0.033
HRV	Radial	0.5	0.02-0.033
HRV	Transverse	0.5	0.02-0.033
LBNH	Vertical	0.5	0.02-0.025
LBNH	Radial	0.5	0.02-0.025
LBNH	Transverse	0.3	0.02-0.025
JFWS	Vertical	0.25	0.02-0.025
JFWS	Radial	0.0	0.02-0.025
JFWS	Transverse	0.25	0.02-0.025
KAPO	Vertical	0.3	0.02-0.025
KAPO	Radial	0.3	0.02-0.025
KAPO	Transverse	0.3	0.02-0.025
CCM	Vertical	0.2	0.02-0.025
CCM	Radial	0.2	0.02-0.025
CCM	Transverse	0.2	0.02-0.025
GOGA	Vertical	0.0	0.02-0.033
GOGA	Radial	0.0	0.02-0.033
GOGA	Transverse	0.0	0.02-0.033

Table 6.1: Weight and bandwidth applied to each component of the different stations used for the moment tensor inversion

reviewed in the previous section. Taking into account the bandwidth used in the modeling (see Table 6.1) and considering that the Pymatuning event was a moderate-size event, I assumed a step source time function. The crustal model used in the inversion is a five-layer model developed by Herrmann (1979) for the central United States. Although derived for the central US, this model proved adequate to model regional waveforms of the 1994 Wyoming Pennsylvania earthquake (Ammon et al., 1998).

6.1.1 LEAST-SQUARES TIME-DOMAIN INVERSION

I first performed least-squares, time-domain inversions of the complete waveforms to estimate the moment tensors for depths between 2.5 and 25 km. Six stations with epicentral distances less than 500 km (BINY, BLA, GWDE, MCWV, SADO, SSPA) were included in the first inversion. Then I added another six stations with epicentral distances between 500-1000 km to test the match between observed and synthetic seismograms, which remained good.

The resulting match between observations and synthetics is reasonably good (see Table 6.2). Like the near-real time analyses, these moment tensor inversion results suggest that the source of the Pymatuning earthquake is not a pure double couple (the intermediate principal moment is not zero and the other two principal moments are not equal and opposite in value). The compensated linear vector dipole (CLVD) ratio f_{clvd} measures how different the source is from a pure double couple source. For a pure double couple source, f_{clvd} is zero, while f_{clvd} is ± 0.5 for a pure CLVD source. The $clvd$ ratio for the Pymatuning earthquake (depth = 5.0 km) is - 0.38 which means that the moment tensor is 76% non double couple.

Least Square Moment Tensor Inversion Misfit								
Depth (km)	Misfit (%)	M ₀ (dyne-cm)	M ₁₁	M ₁₂	M ₁₃	M ₂₂	M ₂₃	M ₃₃
2.5	22.9	5.14E22	-2.31	4.10	0.27	3.50	0.27	-1.19
5.0	29.5	5.67E22	-1.61	4.09	-0.07	4.25	1.24	-2.64
7.5	29.6	5.79E22	-1.60	4.44	-0.08	4.16	0.78	-2.56
10.0	41.3	5.69E22	-1.67	4.36	0.44	4.02	0.96	-2.36
12.5	46.3	5.76E22	-1.63	4.55	0.30	3.77	0.84	-2.13
15.0	51.5	5.70E22	-1.43	4.81	0.31	3.13	1.35	-1.70
17.5	52.1	6.06E22	-1.56	5.26	0.38	3.17	1.19	-1.61
20.0	54.2	6.58E22	-1.99	5.43	0.573	4.00	1.22	-2.01
22.5	65.7	6.20E22	-1.75	5.25	0.88	3.43	1.10	-1.68
25.0	74.5	5.86E22	-0.61	5.15	1.11	2.01	1.83	-1.39

Table 6.2: Least square moment tensor inversion misfits for different depths. Also moment tensor elements.

The estimated moment is 5.6×10^{22} dyne-cm, which corresponds to a moment magnitude of 4.5. The major double couple planes strike at 14 N and 110 N, with dips of 77° and 67° , and rakes of 156° and 15° . The P axis strikes 63 N and plunges 7° , the tension axis strikes 330 N and plunges 26° . These results are consistent with previous studies of the stress regime in central and eastern United States (Zoback, 1992).

The waveform fits computed by assuming a source depth of 2.5 km, 5.0 km, and 7.5 km are shown in Figures 6.1 - 6.12. A blue line represents the observations, and a red line indicates the predictions. The three components of each station are shown with a uniform amplitude scale. A number of waveforms were not used in the inversion but predicted waveforms are computed and displayed for completeness (vertical BINY, and radial BLA, GOGA and JFWS). For stations farther than 500 km, the fits are surprisingly good: the observations and predictions are slightly out of phase but the main features such as the ratio of Rayleigh, Love, and body waves are reproduced very well.

Since I will show a number of waveform comparisons it is worth some time discussing the observations and fits in detail. This should help the

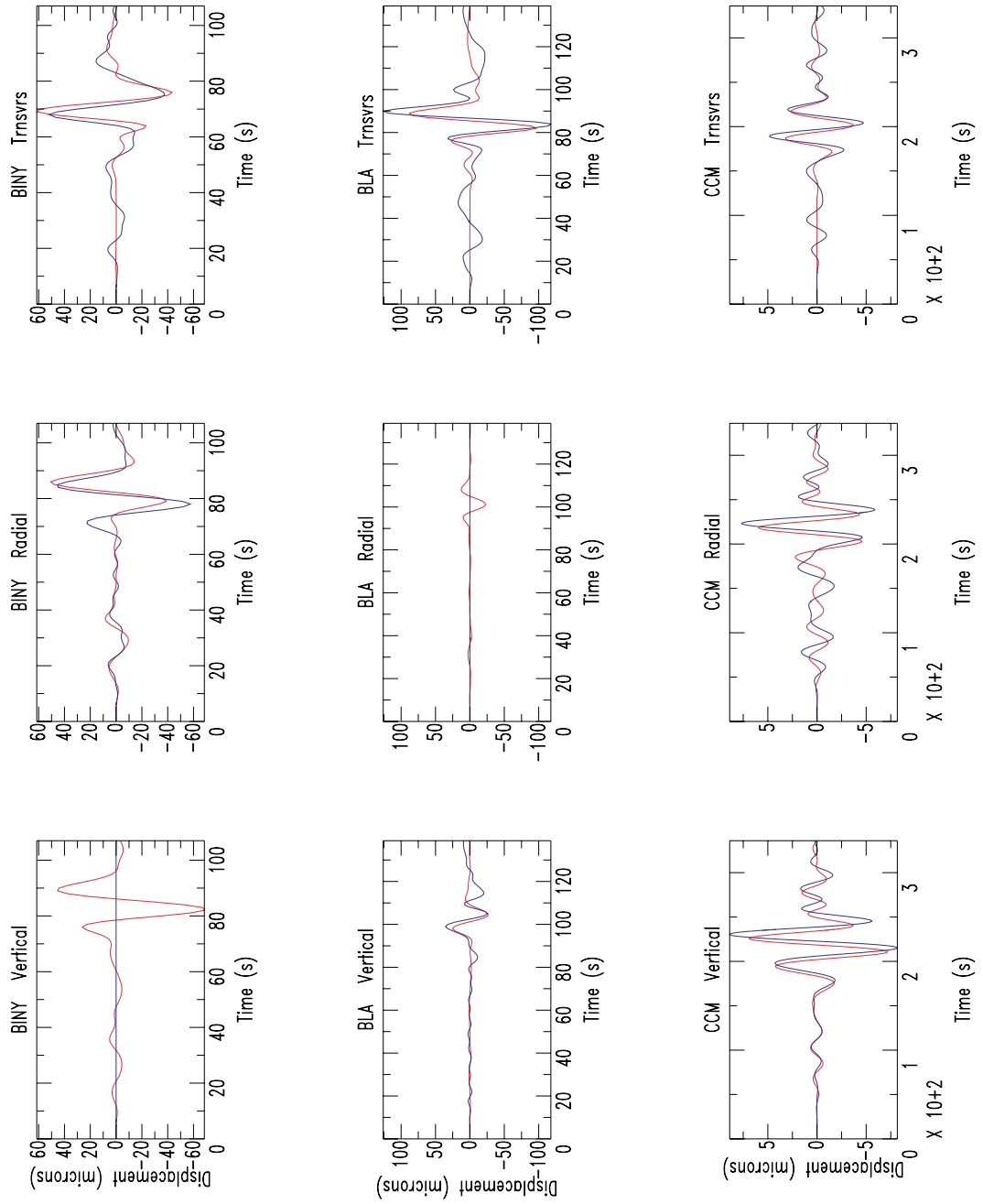


Figure 6.1: Waveform matches corresponding to the least square moment tensor inversion for 2.5 km depth. The blue line identifies the observations, the red line indicates the predictions. The three components of each stations are shown with an individual amplitude scale.

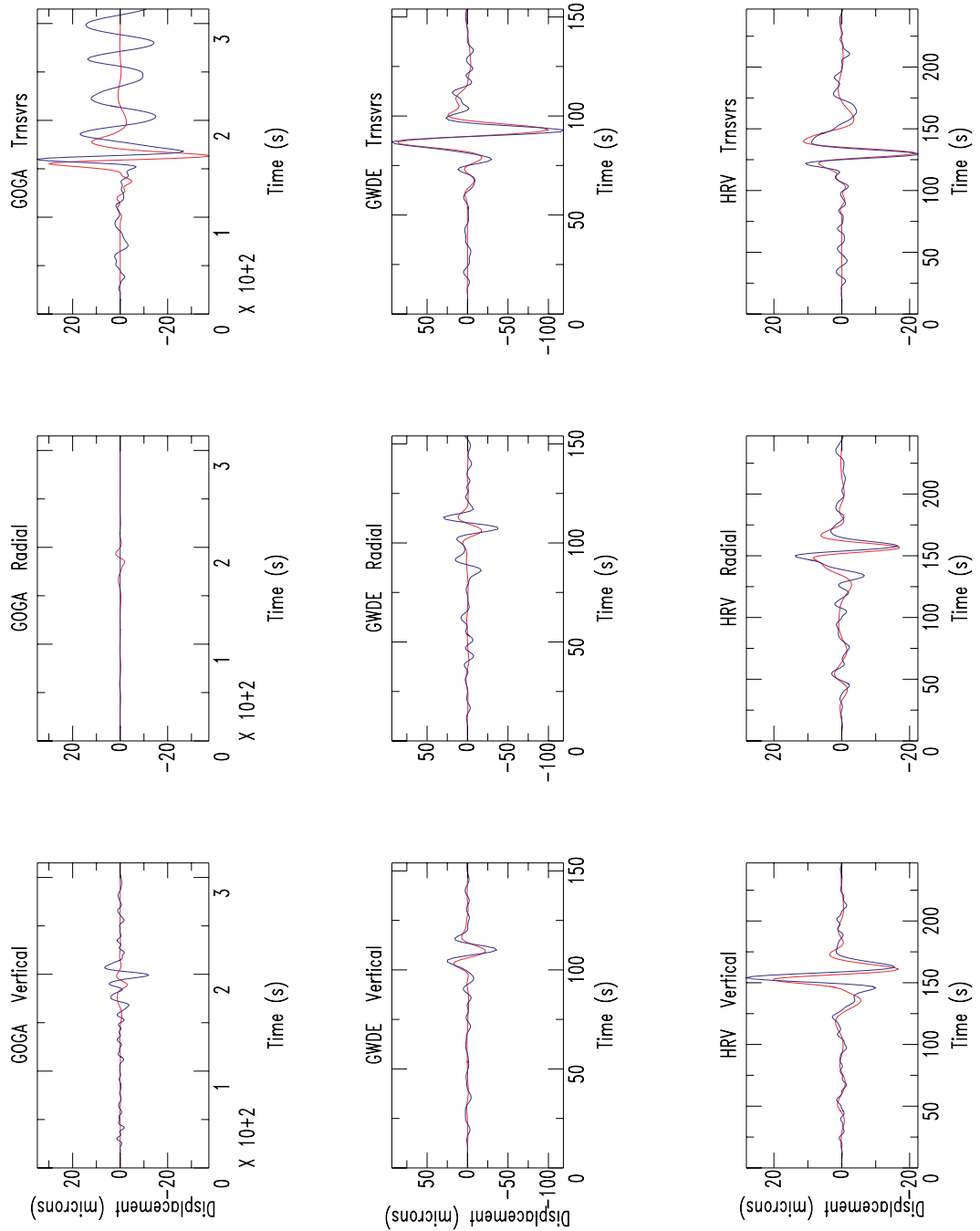


Figure 6.2: Waveform matches corresponding to the least square moment tensor inversion for 2.5 km depth. The blue line identifies the observations, the red line indicates the predictions. The three components of each stations are shown with an individual amplitude scale.

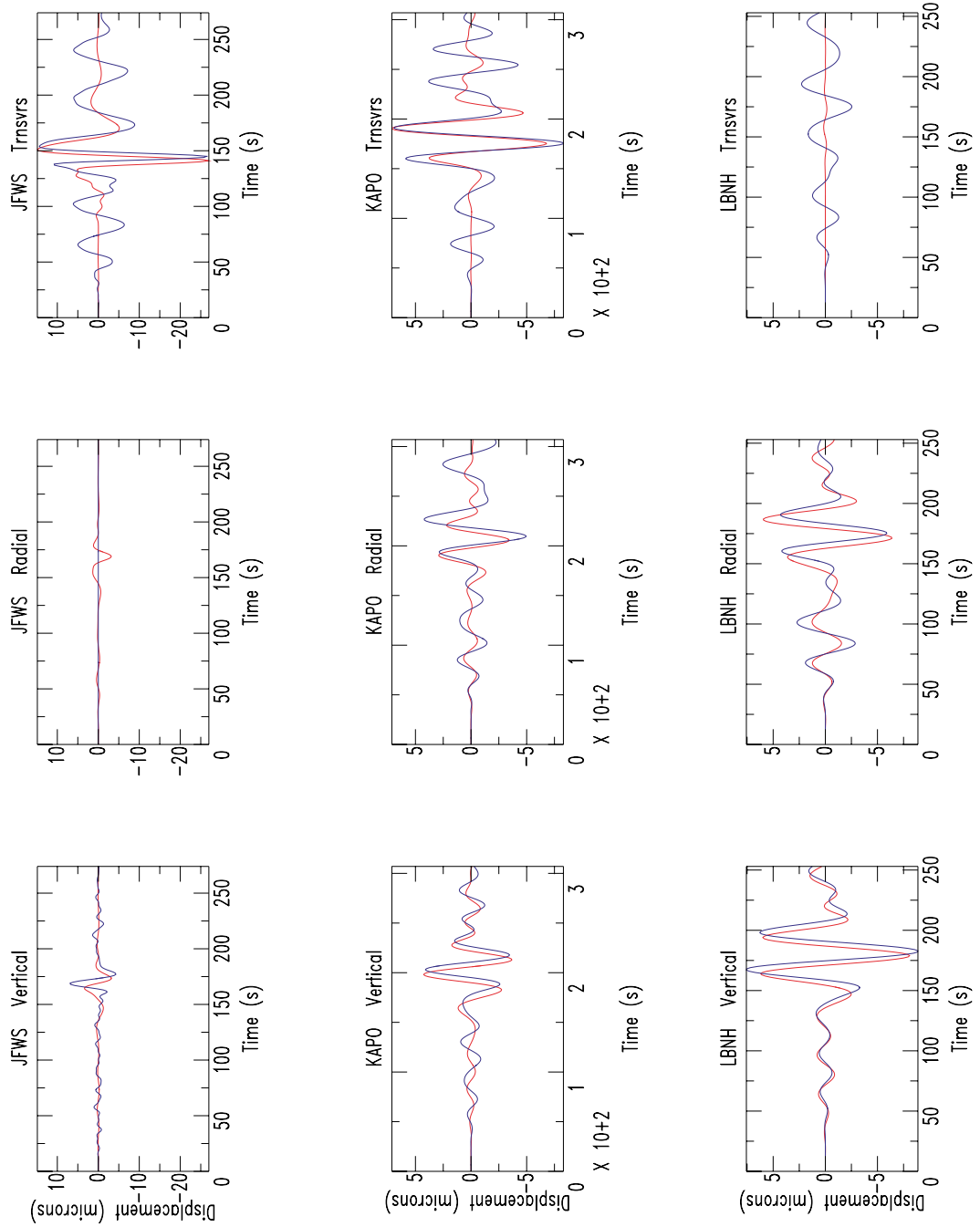


Figure 6.3: Waveform matches corresponding to the least square moment tensor inversion for 2.5 km depth. The blue line identifies the observations, the red line indicates the predictions. The three components of each station are shown with an individual amplitude scale.

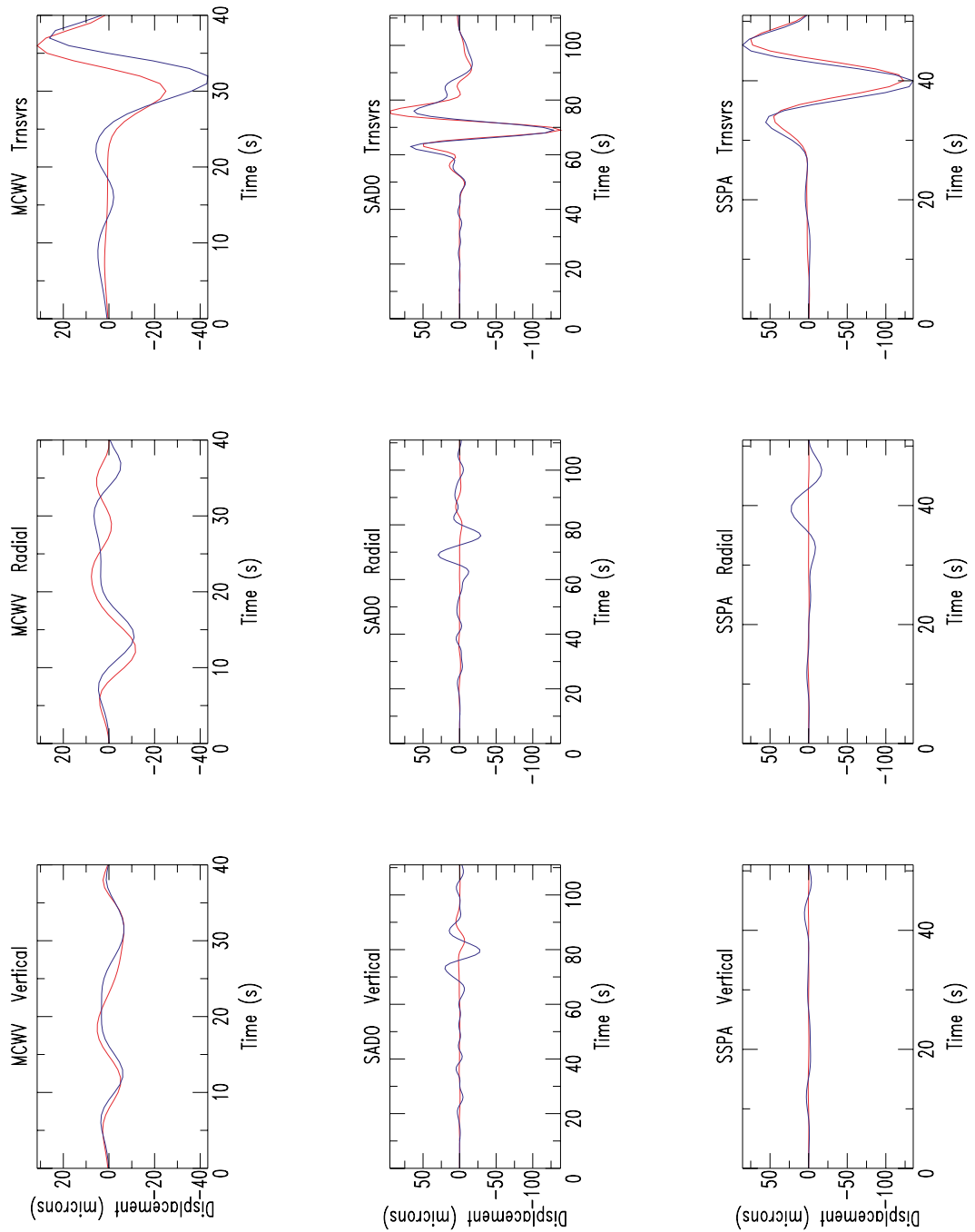


Figure 6.4: Waveform matches corresponding to the least square moment tensor inversion for 2.5 km depth. The blue line identifies the observations, the red line indicates the predictions. The three components of each stations are shown with an individual amplitude scale.

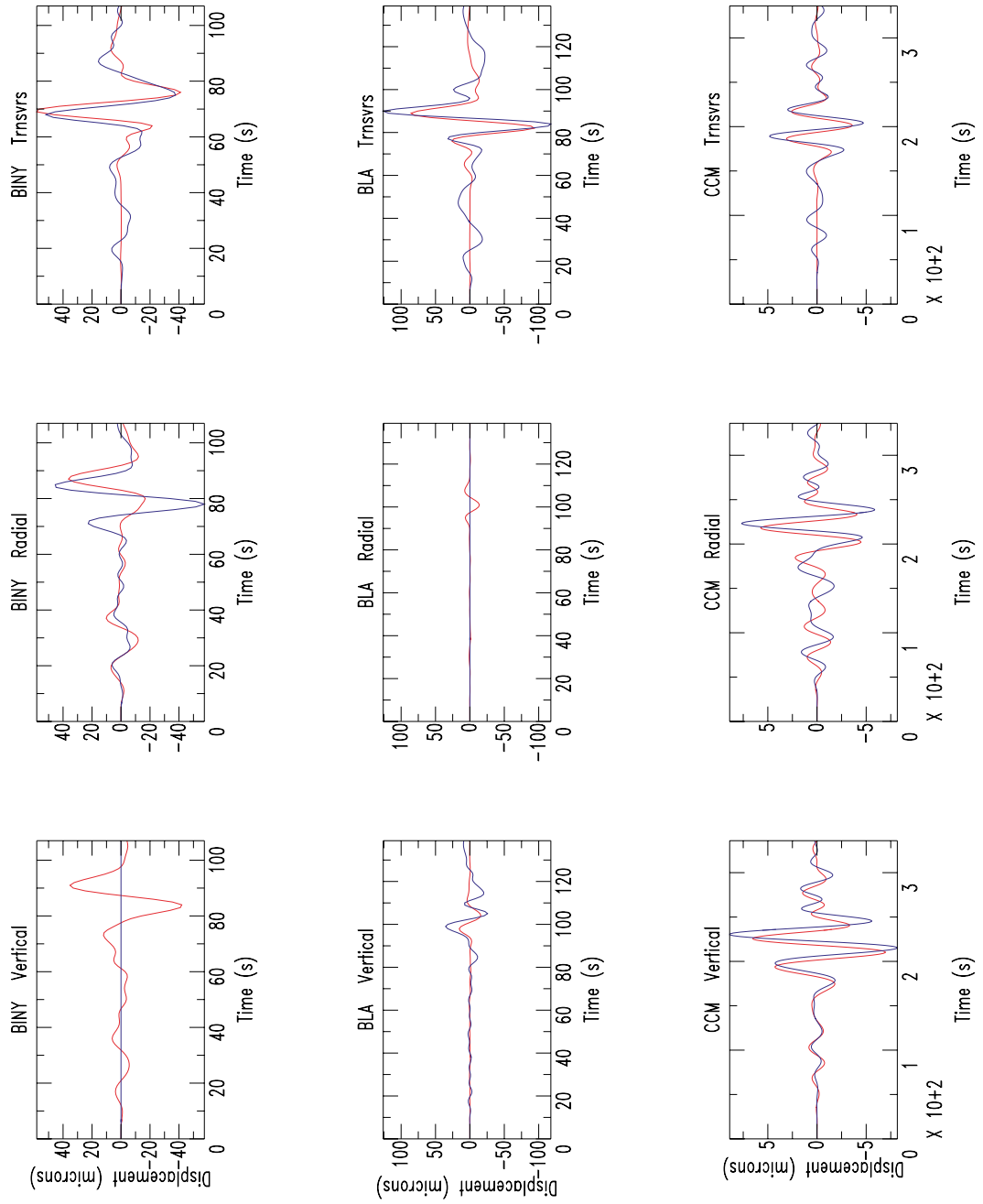


Figure 6.5: Waveform matches corresponding to the best-fitting moment tensor (5 km depth). The blue line identifies the observations, the red line indicates the predictions. Each component of each stations is shown with an individual amplitude scale.

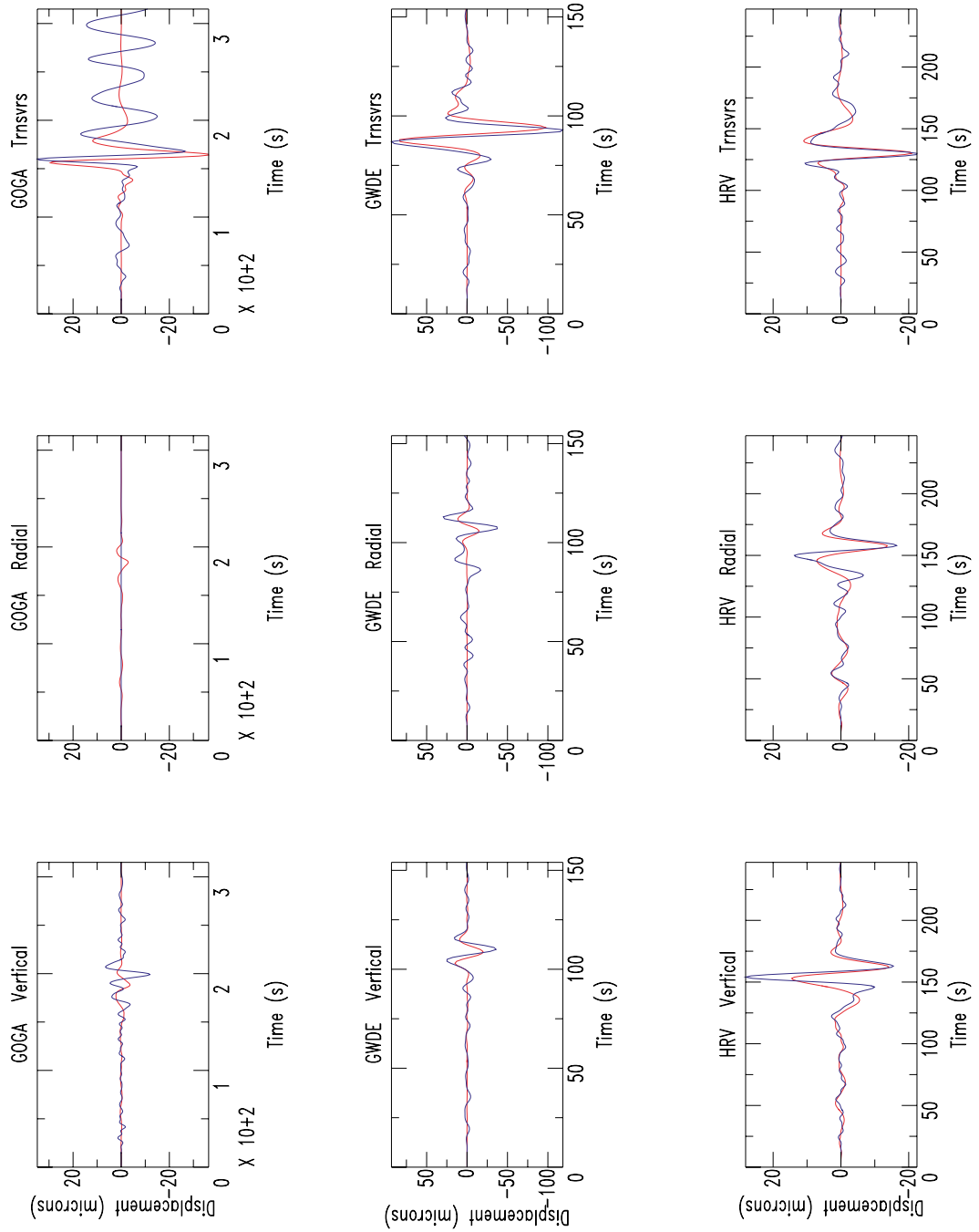


Figure 6.6: Waveform matches corresponding to the best-fitting moment tensor (5 km depth). The blue line identifies the observations, the red line indicates the predictions. Each component of each stations is shown with an individual amplitude scale.

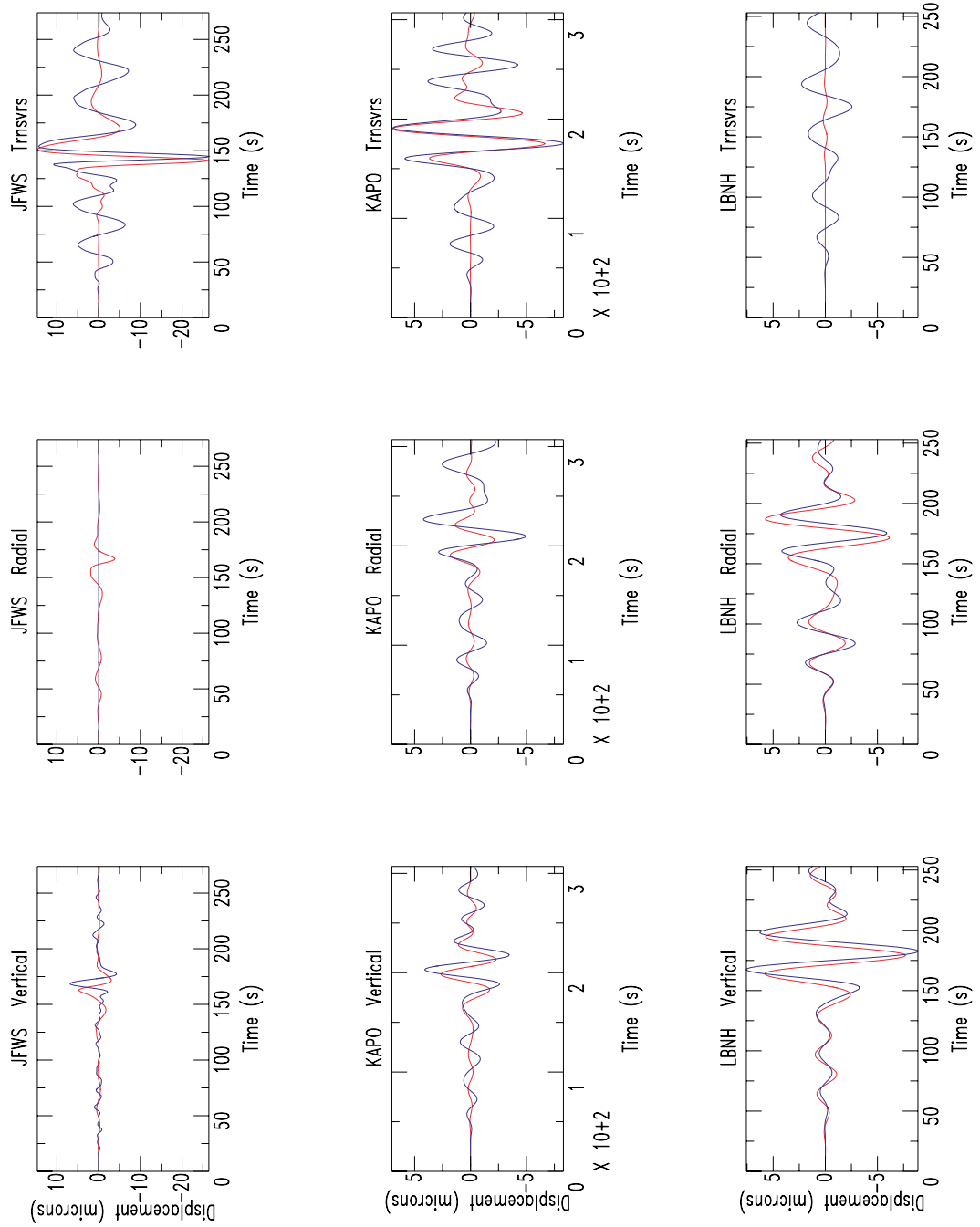


Figure 6.7: Waveform matches corresponding to the best-fitting moment tensor (5 km depth). The blue line identifies the observations, the red line indicates the predictions. Each component of each stations is shown with an individual amplitude scale.

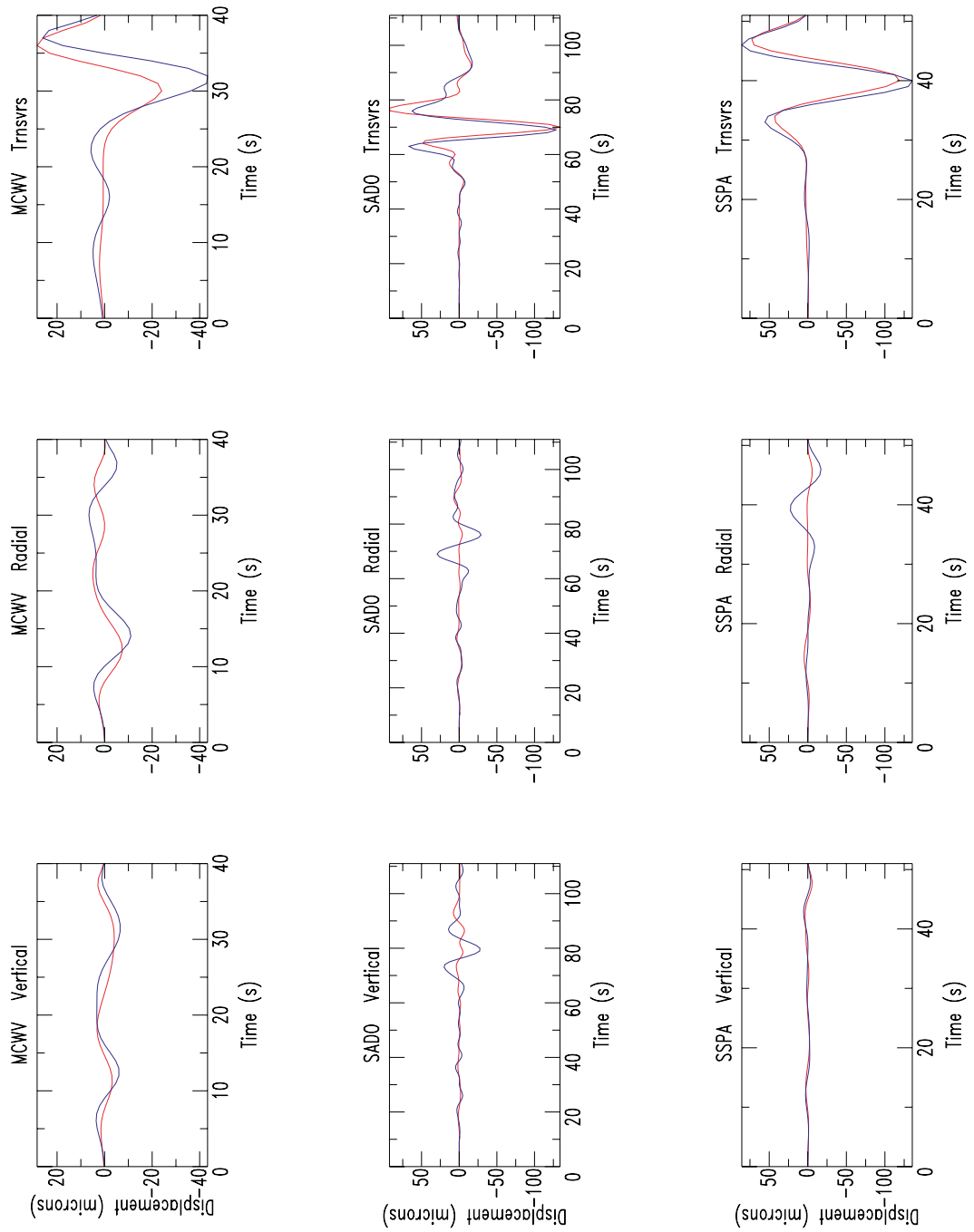


Figure 6.8: Waveform matches corresponding to the best-fitting moment tensor (5 km depth). The blue line identifies the observations, the red line indicates the predictions. Each component of each stations is shown with an individual amplitude scale.

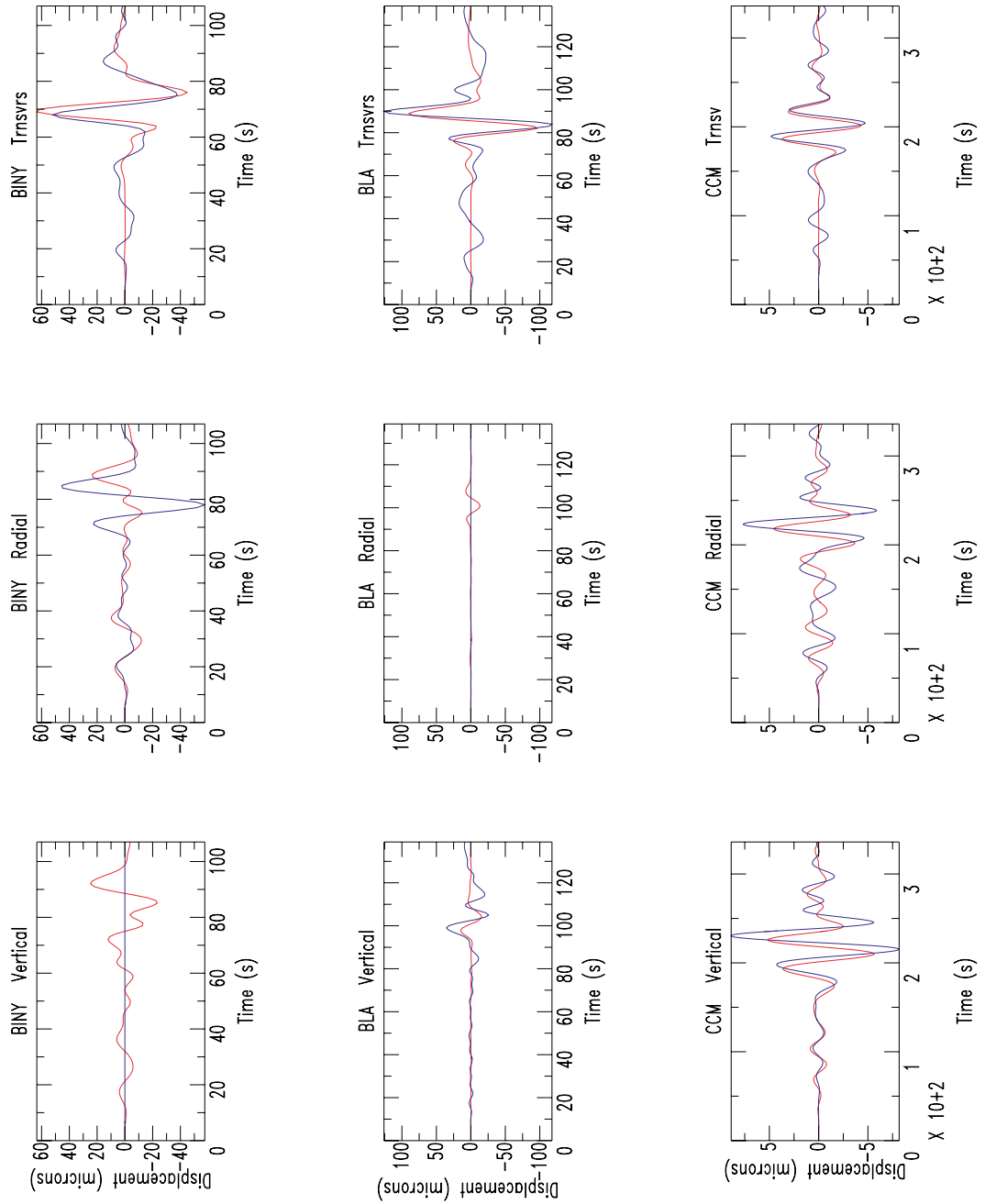


Figure 6.9: Waveform matches corresponding to the least square moment tensor inversion for 7.5 km depth. The blue line identifies the observations, the red line indicates the predictions. The three components of each stations are shown with an individual amplitude scale.

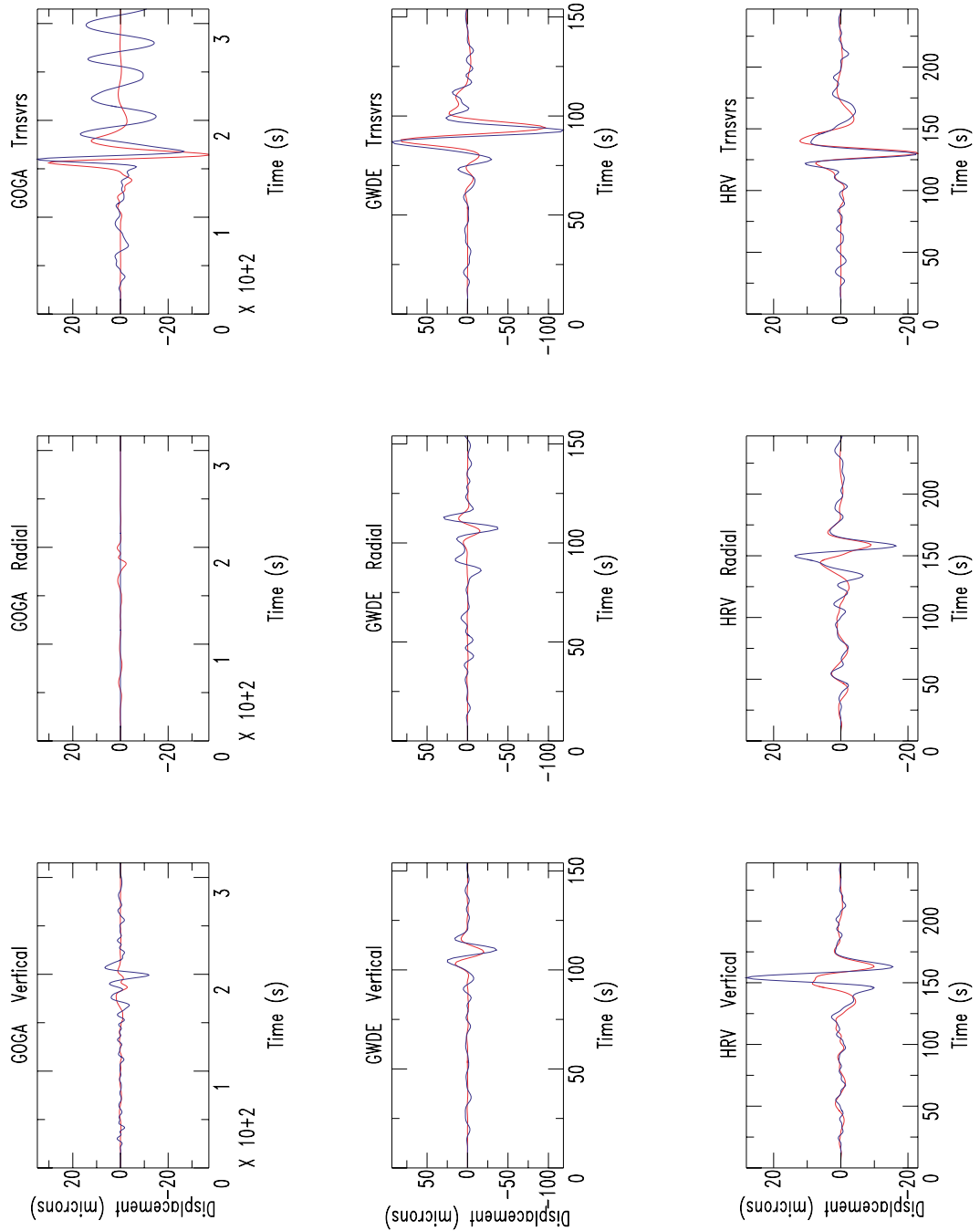


Figure 6.10: Waveform matches corresponding to the least square moment tensor inversion for 7.5 km depth. The blue line identifies the observations, the red line indicates the predictions. The three components of each stations are shown with an individual amplitude scale.

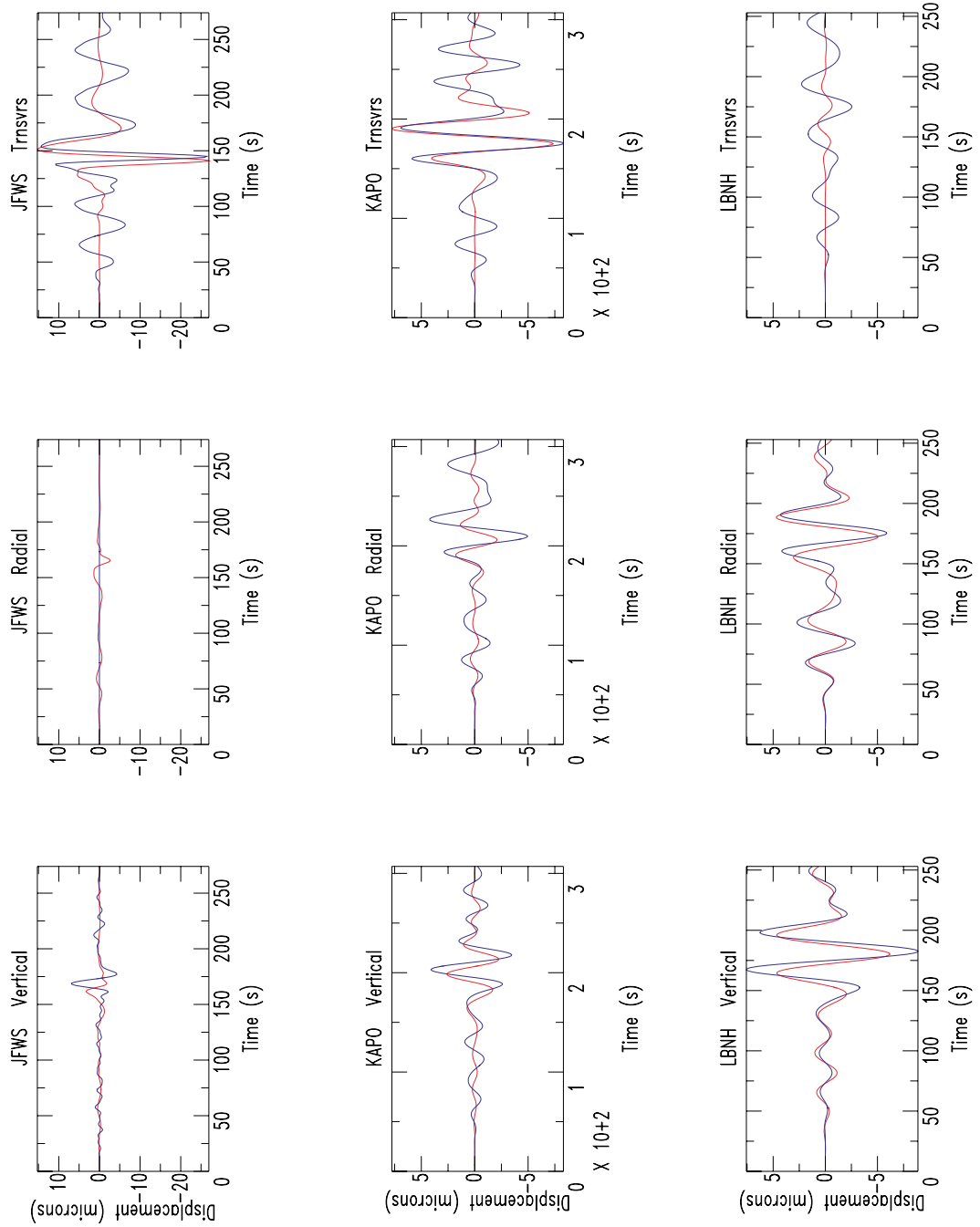


Figure 6.11: Waveform matches corresponding to the least square moment tensor inversion for 7.5 km depth. The blue line identifies the observations, the red line indicates the predictions. The three components of each stations are shown with an individual amplitude scale.

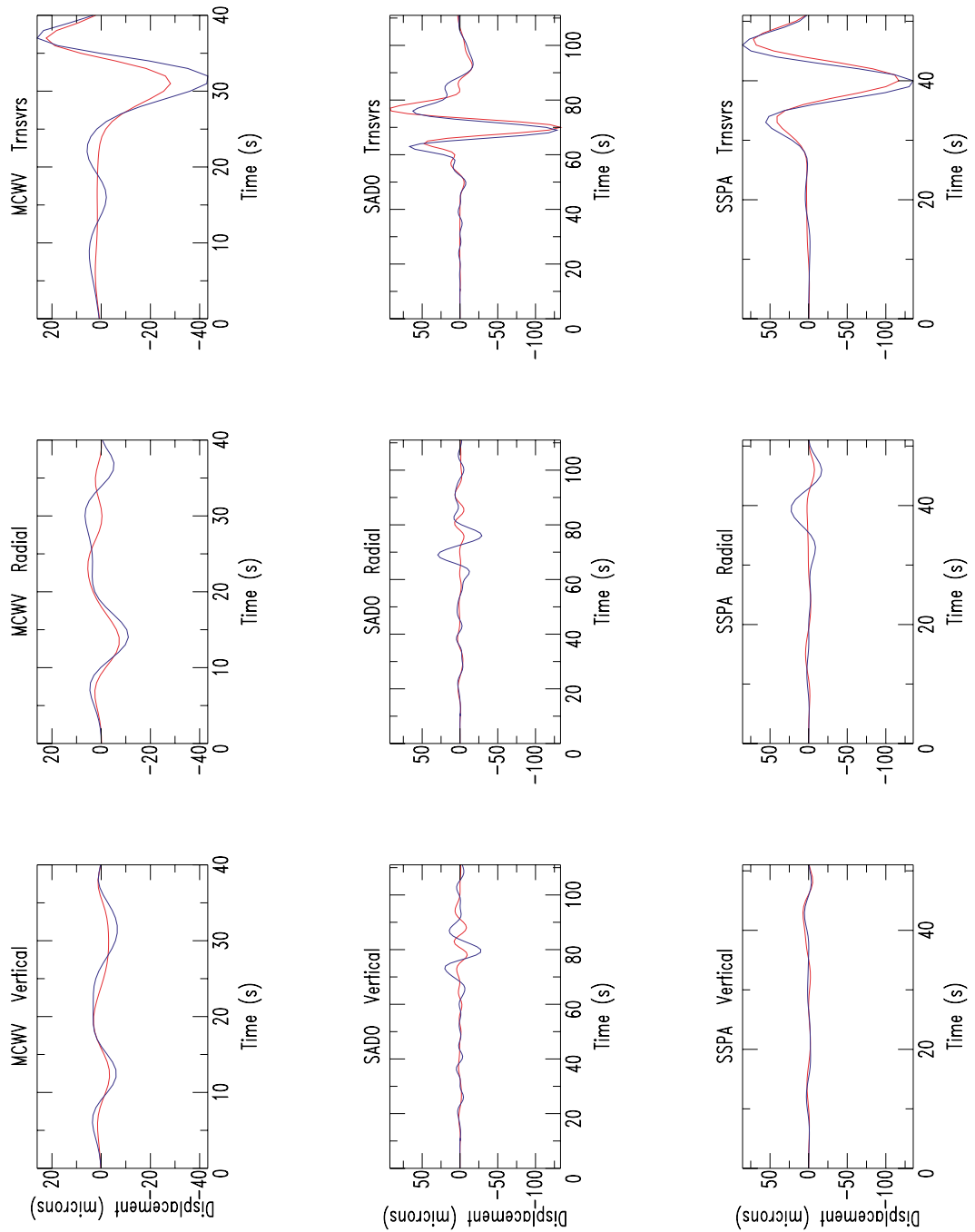


Figure 6.12: Waveform matches corresponding to the least square moment tensor inversion for 7.5 km depth. The blue line identifies the observations, the red line indicates the predictions. The three components of each stations are shown with an individual amplitude scale.

reader compare different solutions discussed later. Seismic waveforms are complex signals that often require visual inspection to discern solutions that may have similar misfit norms. Some of the main characteristics that help constrain the mechanism are the relative amplitudes of Rayleigh and Love waves, and the body waves. For example, the Rayleigh and Love waves are comparable in size at BINY, CCM, HRV, and KAPO, but the Love wave dominates at BLA, GWDE, JFWS, MCWV, SADO, and SSPA, and the Rayleigh waves dominate at station LBNH. Body waves are small at the distant stations but P_{nL} waves are clearly visible at BINY, HRV, and LBNH.

Event depth is best constrained by Rayleigh waves which show substantial sensitivity to this aspect of the source. Although most information on shallow sources is at periods shorter than we can fit with simple earth models, the intermediate period waveforms do constrain the source depth to be less than 7.5 km, and more likely less than five. You can see the effect of source depth by comparing the HRV Rayleigh waves for sources at 2.5 and 7.5 km. The shallower source provide a good match but the deeper value significantly underestimates the HRV Rayleigh wave amplitude. Later I use a teleseismic body wave to corroborate this observation and to show the shallower depth is more appropriate for the Pymatuning event. For now, I return to an investigation of the non double couple components of the source.

Lower hemisphere focal mechanisms for the full moment tensor for a depth of 5 km and two equivalent decompositions are shown in Figure 6.13. The area of each projection is proportional to the moment. The major and minor double couple decomposition is shown in the second row.

The major double couple is a strike slip mechanism with the same P and T axes as the main event. The minor double couple is about 40% smaller with a rotated principal axes (P-to-T, T-to-B, B-to-P). The change in stress directions is somewhat problematic when trying to interpret a non-double couple source as a multiple event. To investigate an alternative that preserves the compressional direction (Villagomez, 1999) (a feature appealing in ENA) is shown in the bottom row. The mechanisms consist of a slightly smaller version of the major DC and a suitably oriented reverse fault (strike of 180, dip of 45, rake of 129°).

Each of the moment tensor decompositions in Figure 6.13 is equivalent and consistent with the full moment tensor. However, before interpreting the apparent source complexity in terms of multiple ruptures, we must carefully and thoroughly investigate the significance of an exotic source. Can we explain the observations with a simpler source? Are certain outlier observations producing the non-double couple component in the source?

6.1.2 L1 NORM TIME-DOMAIN INVERSION

The results from the least-squares, time-domain moment tensor inversion fit the observed waveforms properly, but the percentage of non double-couple component to the faulting mechanism is very high (76%). One hypothesis is that some observations are outliers and that they are producing this high percentage of non double-couple. To test this hypothesis, I performed the inversion using an L1 norm, which is less sensitive to outliers. I used the complete observed seismograms from the same twelve closest stations, in the same bandwidth and with the same inversion weight.

These results also produce a good fit to the observations (see Table 6.3)

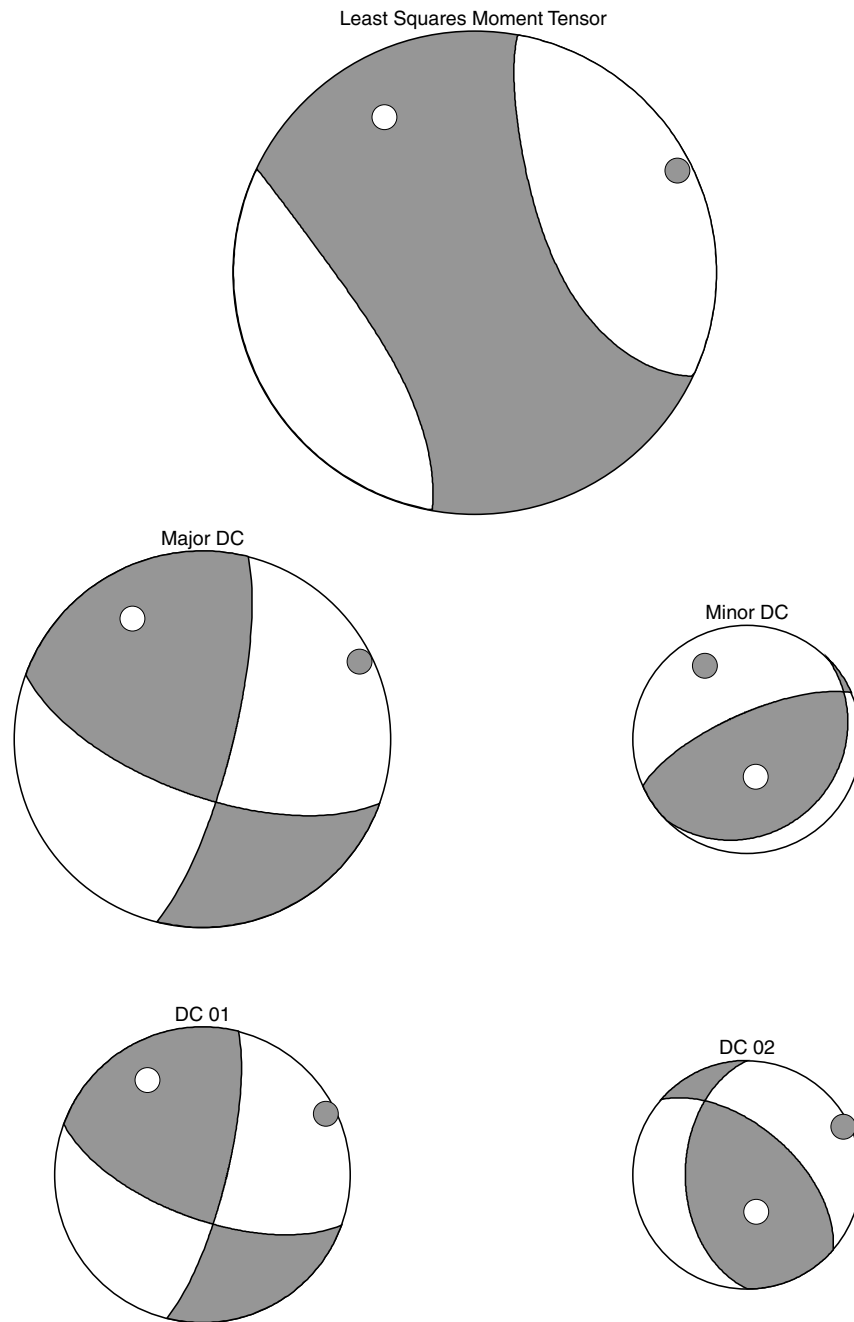


Figure 6.13: Non double-couple focal mechanism resulting from the least squares moment tensor inversion. Decomposition of this NDC mechanism into a major and a minor double couple. The second decomposition is performed fixing the P axis.

Norm L1 Moment Tensor Inversion Misfit								
Depth (km)	Misfit (%)	M ₀ (dyne-cm)	M ₁₁	M ₁₂	M ₁₃	M ₂₂	M ₂₃	M ₃₃
2.5	23.4	4.96E22	-2.15	3.95	-0.50	3.21	-0.84	-1.06
5.0	30.0	5.23E22	-1.77	4.04	-0.60	3.72	0.52	-1.95
7.5	29.8	5.58E22	-1.73	4.43	-0.41	3.83	0.45	-2.11
10.0	42.0	5.53E22	-1.75	4.39	-0.36	3.74	0.83	-1.99
12.5	47.1	5.98E22	-2.06	4.82	-0.37	3.95	0.79	-1.89
15.0	52.3	5.90E22	-1.88	4.85	-0.43	3.64	1.11	-1.76
17.5	53.1	5.76E22	-1.83	4.82	-0.40	3.45	0.92	-1.62
20.0	55.7	5.71E22	-1.79	4.76	-0.43	3.47	0.86	-1.68
22.5	67.5	5.53E22	-1.92	4.61	-0.45	3.29	0.98	-1.37
25.0	77.0	4.93E22	-1.31	4.21	-0.47	2.50	1.26	-1.19

Table 6.3: L1 Norm moment tensor inversion misfits for different depths. Also moment tensor elements.

and a smaller, but still large, percentage of non double-couple component to the faulting mechanism (57%). These results are very similar to the least-squares estimate and so they are also consistent with previous studies of the stress regime in the area. The estimated moment is 5.2×10^{22} dyne-cm, which corresponds to a moment magnitude of 4.4. The major double couple planes strike at 15 N and 109 N, with dips of 77° and 75° , and rakes of 165° and 13° . The P axis strikes 62 N and plunges 1° , the tension axis strikes 332 N and plunges 19° .

The waveform fits computed by assuming source depths of 2.5 and 5.0 km are shown in Figures 6.14 - 6.21. Once again, the match to the observations is not perfect, but the main features are fit well.

The moment tensor closely resembles the least squares estimate and is illustrated in Figure 6.22, which shows the similar radiation pattern and a slightly smaller non-double couple component. As expected, the decompositions produce results similar to that of the least-squares analysis.

These results indicate that the high percentage of non double-couple component to the faulting mechanism is not produced by gross outliers. To check if the observations from a specific station are causing the non

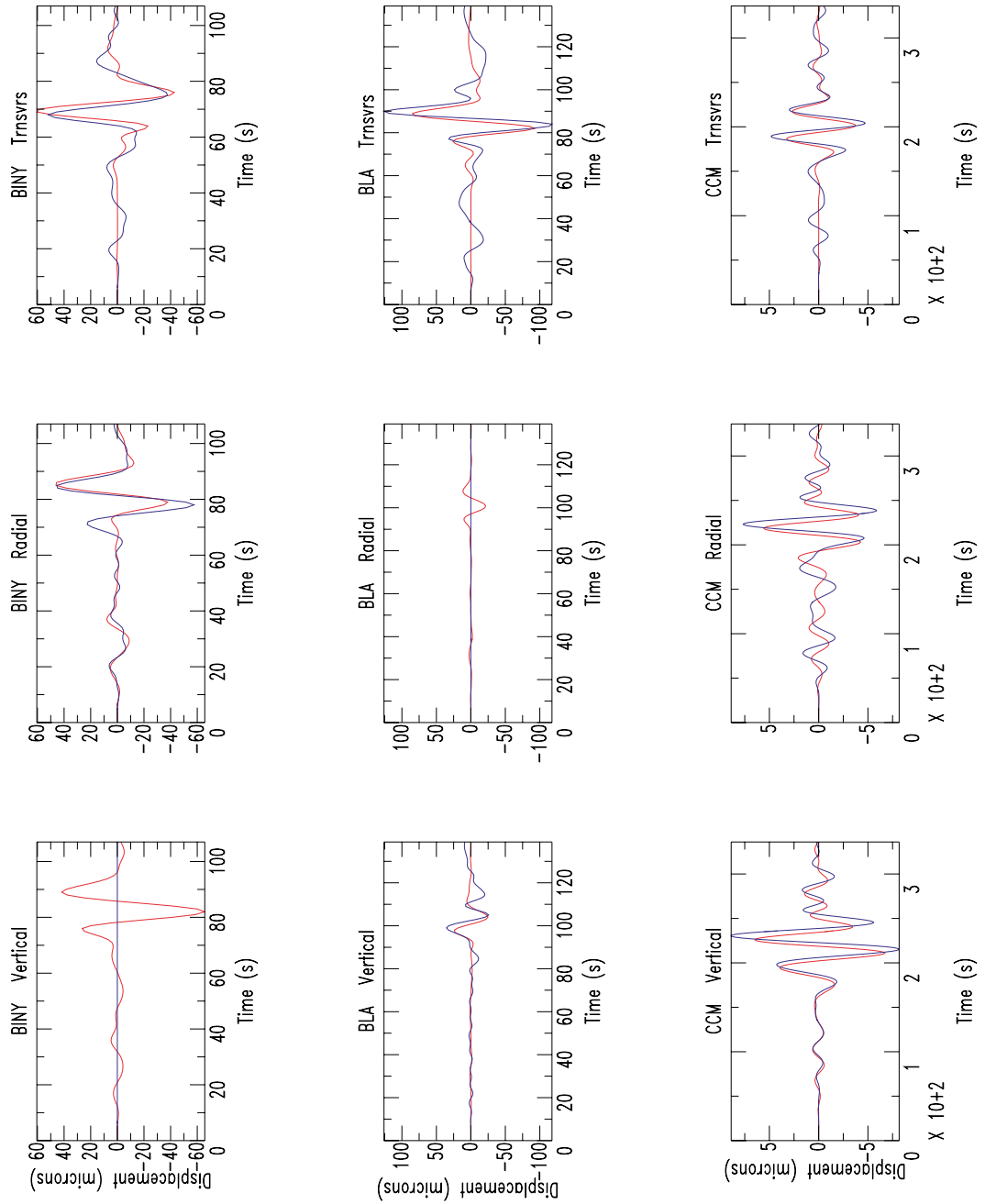


Figure 6.14: Waveform matches corresponding to the best-fitting L1 moment tensor (2.5 km depth). The blue line identifies the observations, the red line indicates the predictions. Each component of each stations is shown with an individual amplitude scale.

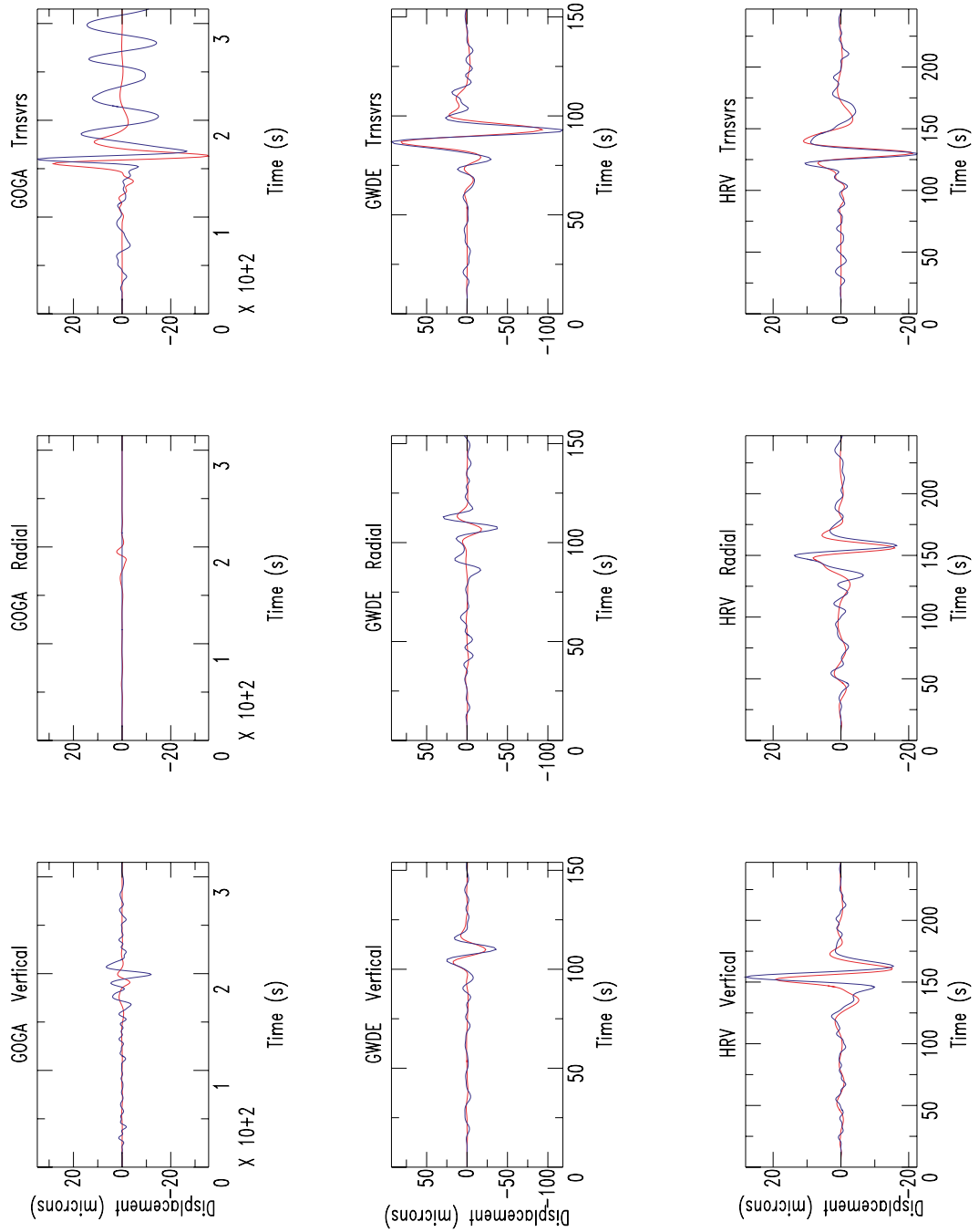


Figure 6.15: Waveform matches corresponding to the best-fitting L1 moment tensor (2.5 km depth). The blue line identifies the observations, the red line indicates the predictions. Each component of each stations is shown with an individual amplitude scale.

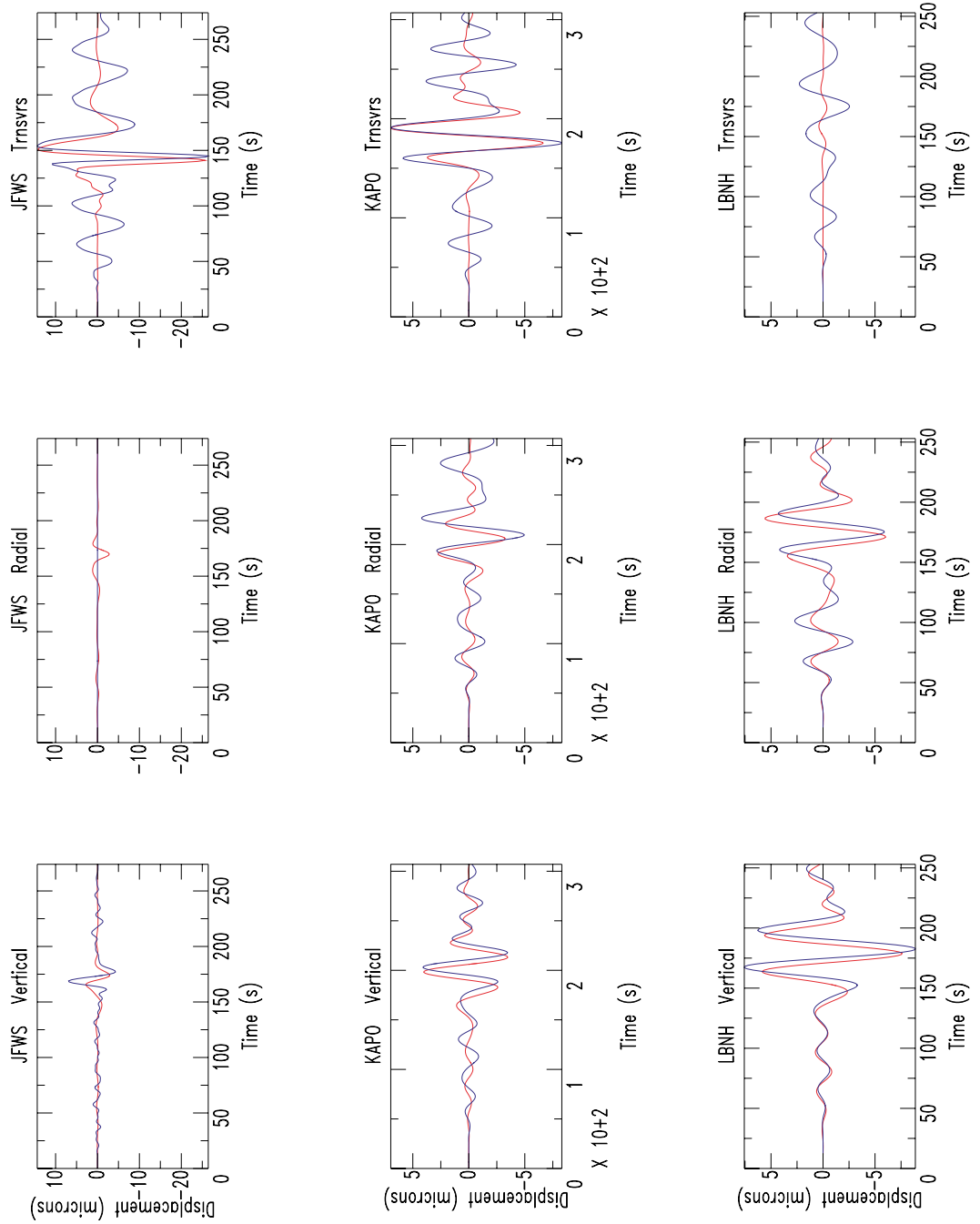


Figure 6.16: Waveform matches corresponding to the best-fitting L1 moment tensor (2.5 km depth). The blue line identifies the observations, the red line indicates the predictions. Each component of each stations is shown with an individual amplitude scale.

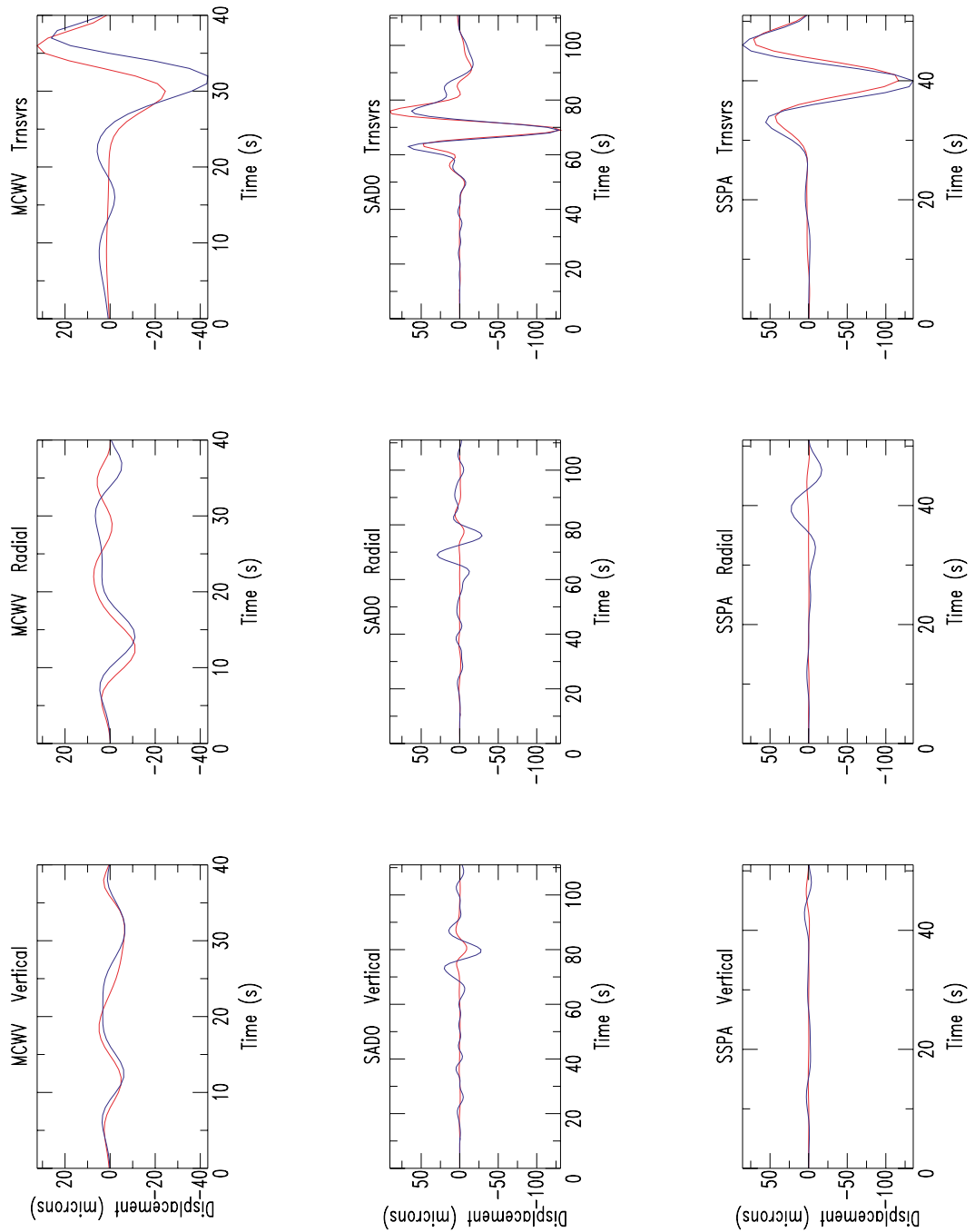


Figure 6.17: Waveform matches corresponding to the best-fitting L1 moment tensor (2.5 km depth). The blue line identifies the observations, the red line indicates the predictions. Each component of each stations is shown with an individual amplitude scale.

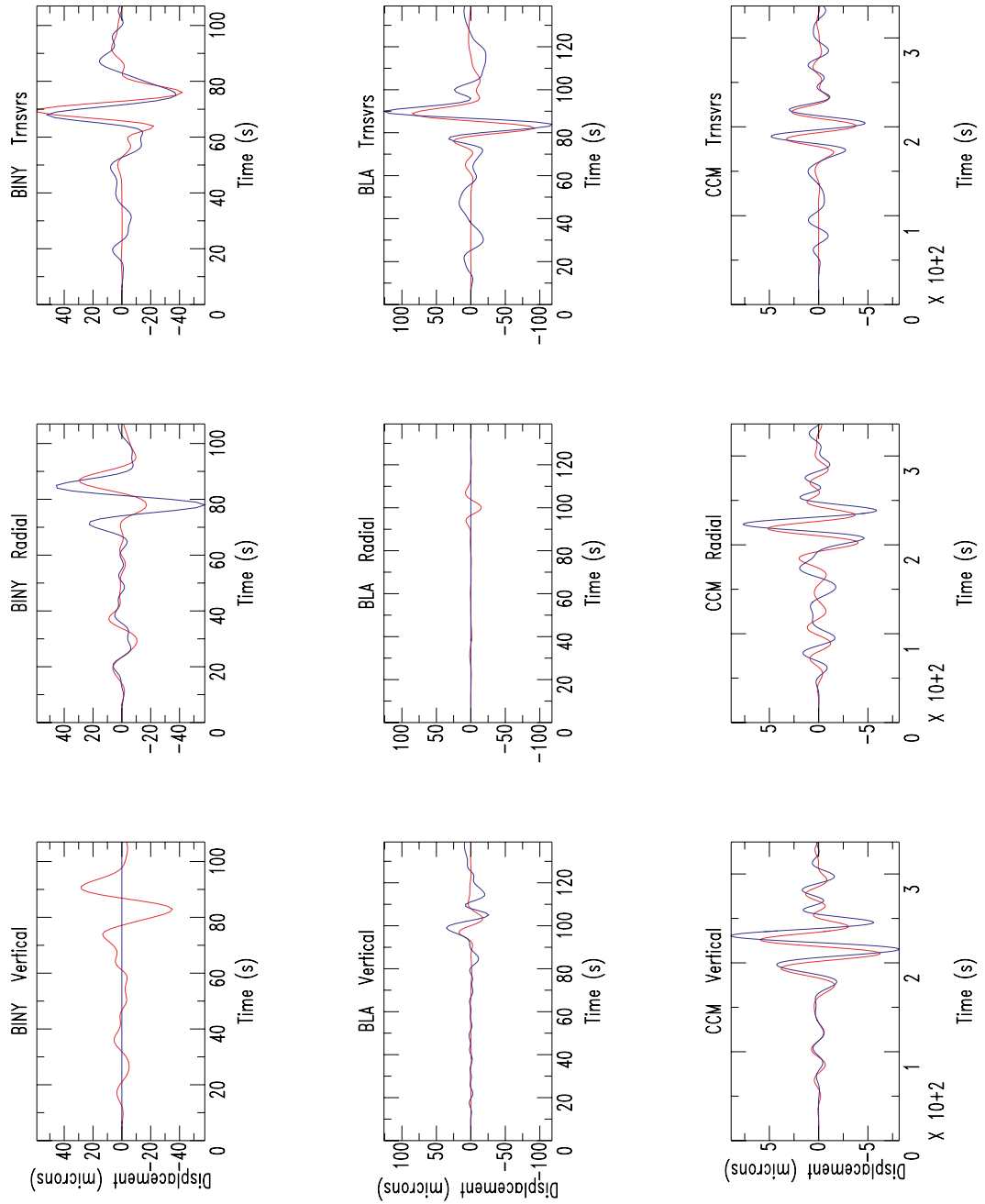


Figure 6.18: Waveform matches corresponding to the best-fitting L1 moment tensor (5 km depth). The blue line identifies the observations, the red line indicates the predictions. Each component of each stations is shown with an individual amplitude scale.

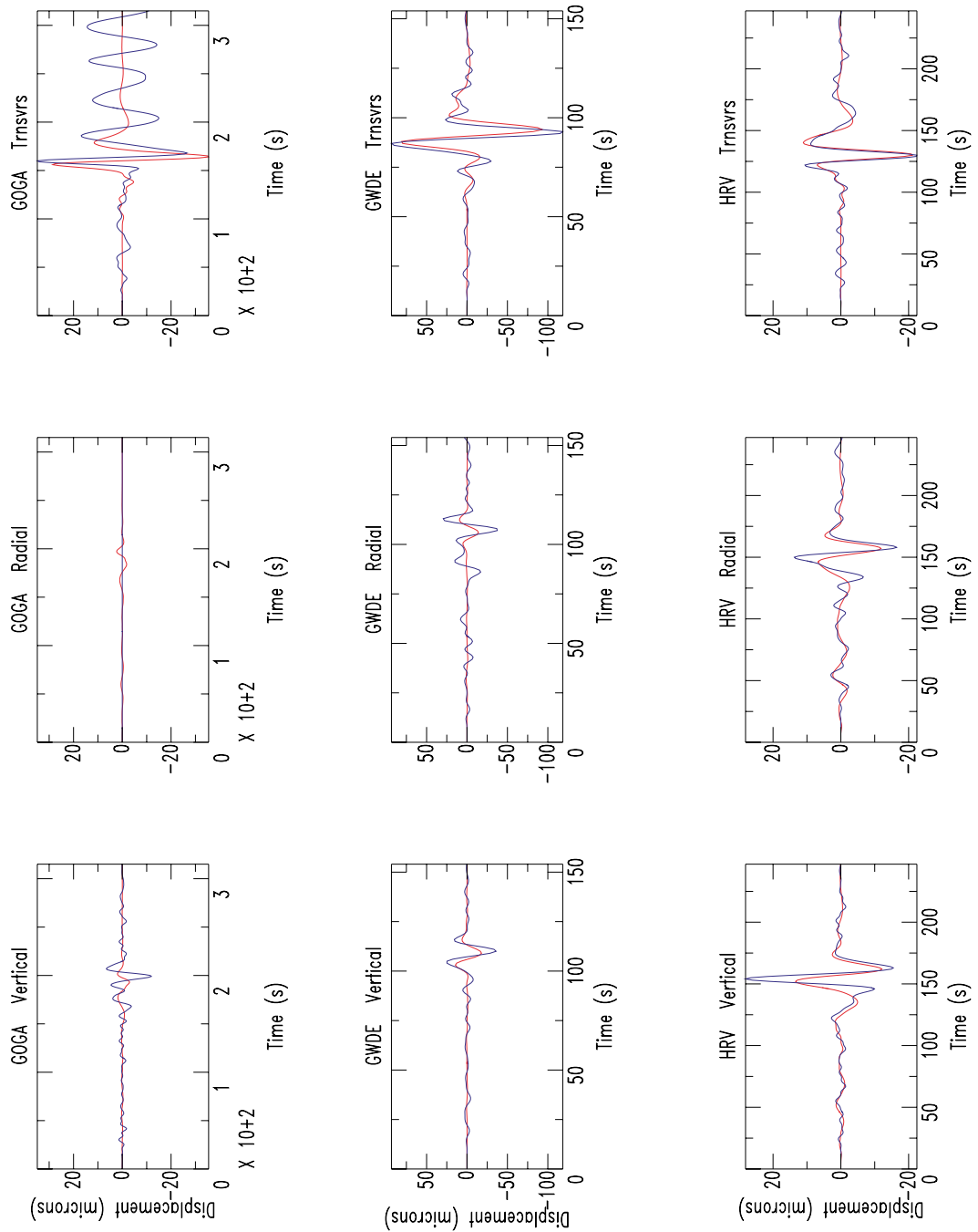


Figure 6.19: Waveform matches corresponding to the best-fitting L1 moment tensor (5 km depth). The blue line identifies the observations, the red line indicates the predictions. Each component of each stations is shown with an individual amplitude scale.

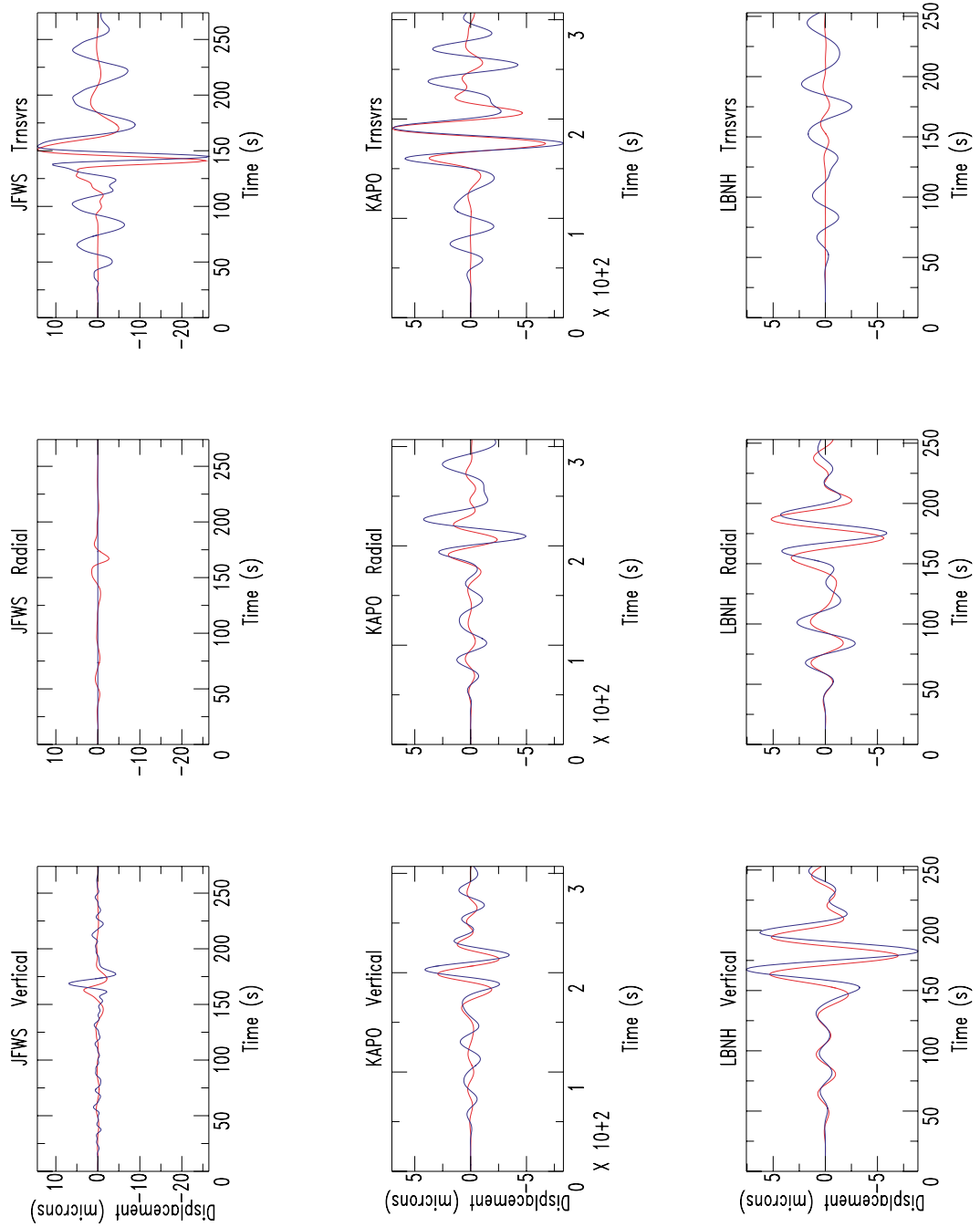


Figure 6.20: Waveform matches corresponding to the best-fitting L1 moment tensor (5 km depth). The blue line identifies the observations, the red line indicates the predictions. Each component of each stations is shown with an individual amplitude scale.

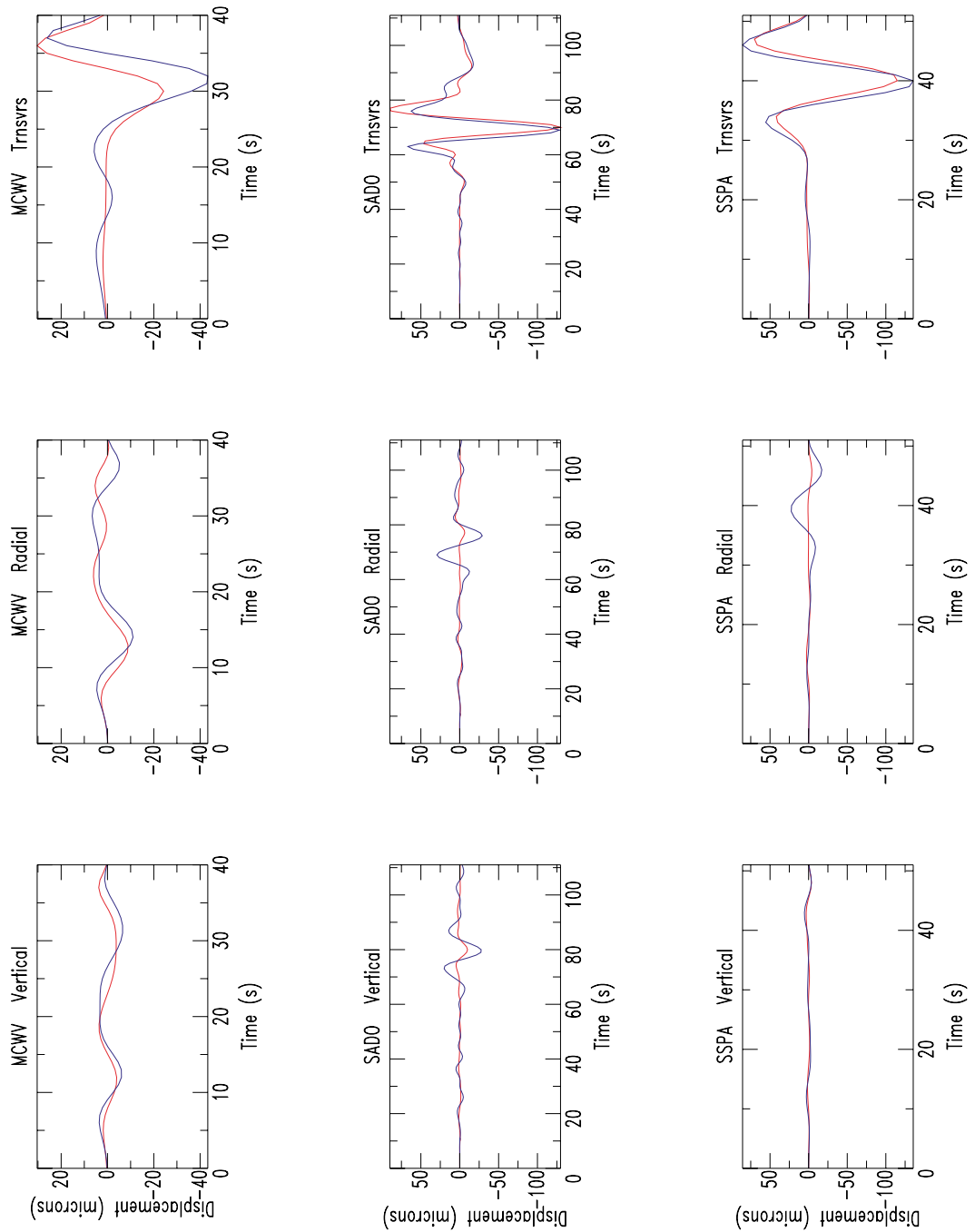


Figure 6.21: Waveform matches corresponding to the best-fitting L1 moment tensor (5 km depth). The blue line identifies the observations, the red line indicates the predictions. Each component of each stations is shown with an individual amplitude scale.

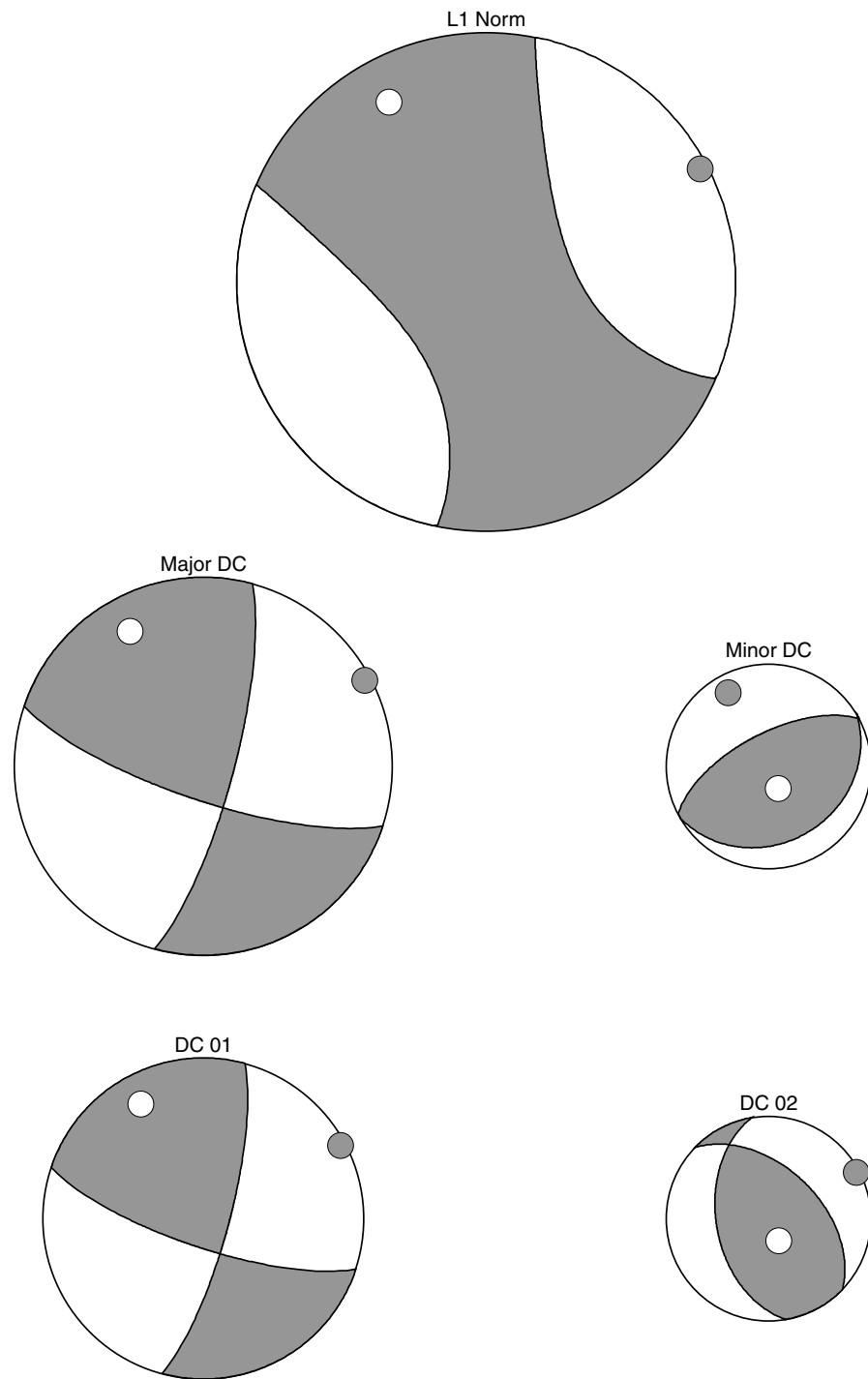


Figure 6.22: Non double-couple focal mechanism resulting from the L1 norm moment tensor inversion. Decomposition of this NDC mechanism into a major and a minor double couple. The second decomposition is performed fixing the P axis.

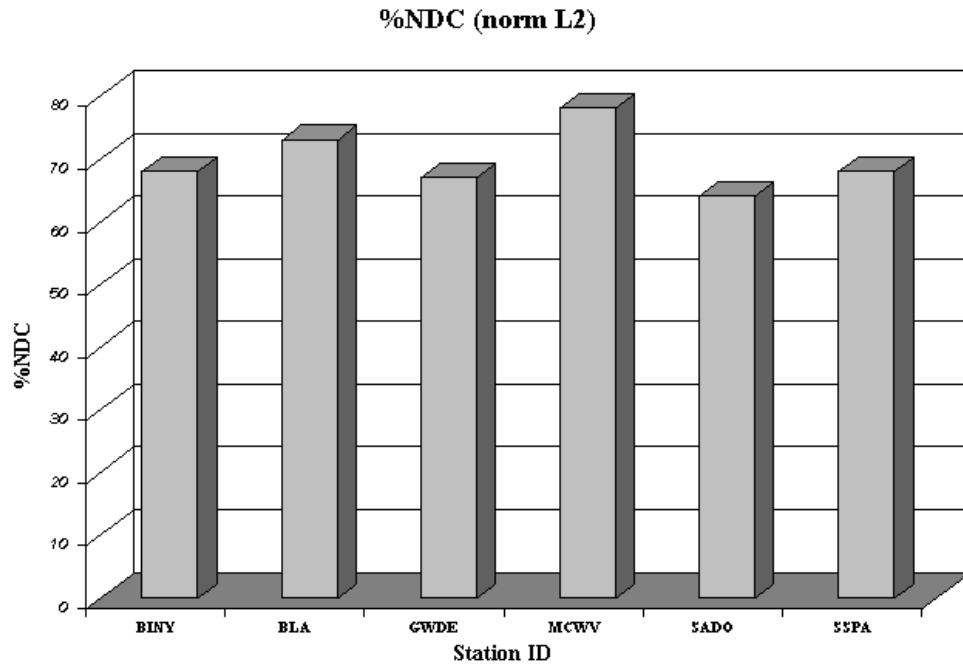


Figure 6.23: Percentage of non double-couple to the faulting mechanism resulted from least-squares, time-domain, moment tensor inversion when one of the stations is not considered.

double-couple, I performed separate inversions excluding, one at a time, one of the closest stations. The resulting percentage of non double couple component, for L2 and L1 norms, are shown in Figures 6.23 and 6.24 respectively. Both graphs show clearly that waveforms at no single station are dominating the others and producing a high percentage of the non double-couple source.

6.2 THE GRID SEARCH

We have one last test that we can perform to investigate the significance of the non double couple component of the source - a grid search inversion that allows only pure double couples. In essence we accept that the non

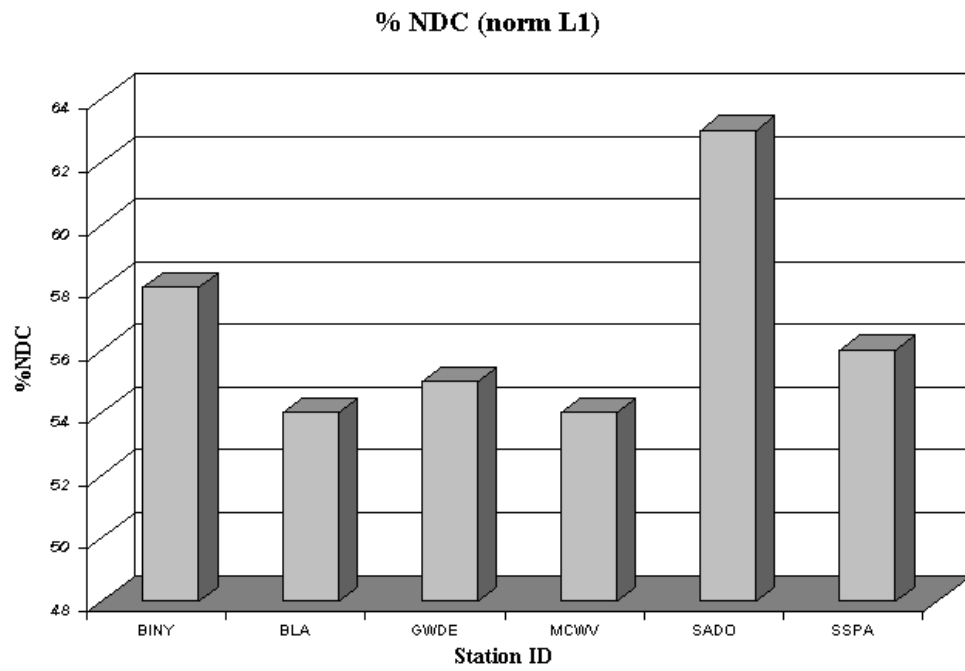


Figure 6.24: Percentage of non double-couple to the faulting mechanism resulted from L1 norm, time-domain, moment tensor inversion when one of the stations is not considered.

Grid Search Misfit					
Depth (km)	Misfit (%)	M_0 (dyne-cm)	Strike ($^\circ$)	Dip ($^\circ$)	Slip ($^\circ$)
2.5	63.7	5.69E22	110	70	20
5.0	69.8	5.67E22	110	70	20
7.5	70.7	5.63E22	110	80	10
10.0	76.3	5.74E22	110	80	10
12.5	78.2	5.83E22	10	80	170
15.0	81.5	6.16E22	10	80	170
17.5	83.7	6.73E22	10	80	170
20.0	87.2	7.48E22	110	80	10
22.5	91.1	7.83E22	110	80	0
25.0	95.7	8.03E22	20	90	170

Table 6.4: Grid search misfits for different depths. Also the obtained fault parameters.

double source fits the observations but now ask can we also fit them with a simpler pure double couple?

I performed a separate grid search for each depth between 2.5 km and 25 km with intervals of 2.5 km, and again the match to the observed seismograms is good (see Table 6.4). The best fit from the grid search for the Pymatuning event is a near-vertical, mostly strike-slip fault at a shallow depth between 2.5 and 7.5 km (see Figure 6.25). The fault planes for this fault strike 110 N and 13 N, with dips of 70 $^\circ$ and 71 $^\circ$, and rakes of 20 $^\circ$ and 159 $^\circ$. The estimated moment from the grid search at 5.0 km depth is 5.6×10^{22} dyne-cm, which corresponds to a moment magnitude of 4.5. The mechanism resembles the major double couples from the moment tensor inversions.

The waveform fits computed by assuming source depths of 2.5 and 5.0 km are shown in Figures 6.26 - 6.33. The fits are comparable to those obtained from the least-squares, time-domain moment tensor inversion. To facilitate comparison of the solutions, I plotted the synthetic seismograms

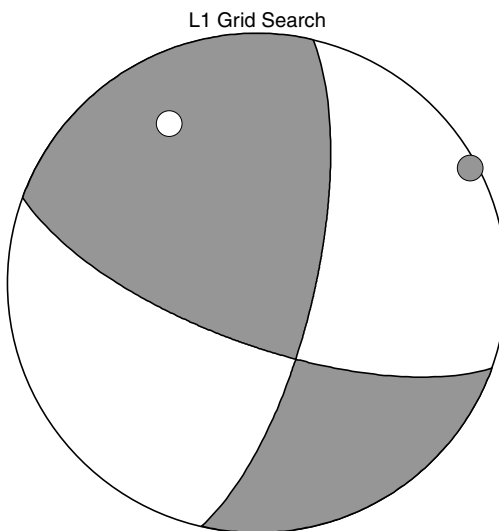


Figure 6.25: Pure double couple focal mechanism for the Pymatuning earthquake from the Grid Search.

for the moment tensor and dislocation sources in Figures 6.34 - 6.37. Examination of these plots suggests that the largest improvement in fit for non double couple source occurs on the nodal surface waves (BLA, GOGA, GWDE, JFWS, MCWV, SADO, and SSPA) which are small and most likely contaminated by “noise” (waves that arrive with relatively large amplitude but they didn’t follow the direct path). So, we can fit the observations with a pure double couple mechanism, but the question is: Does the non double-couple moment tensor fit the observations significantly better? No.

6.3 IMPROVING SOURCE DEPTH RESOLUTION

All three inversions performed in this study, match the observed seismograms well for a source depth less than 7.5 km. The best “formal” fit is for the shallowest source, but the 5.0 and 7.5 km depths fit the data well.

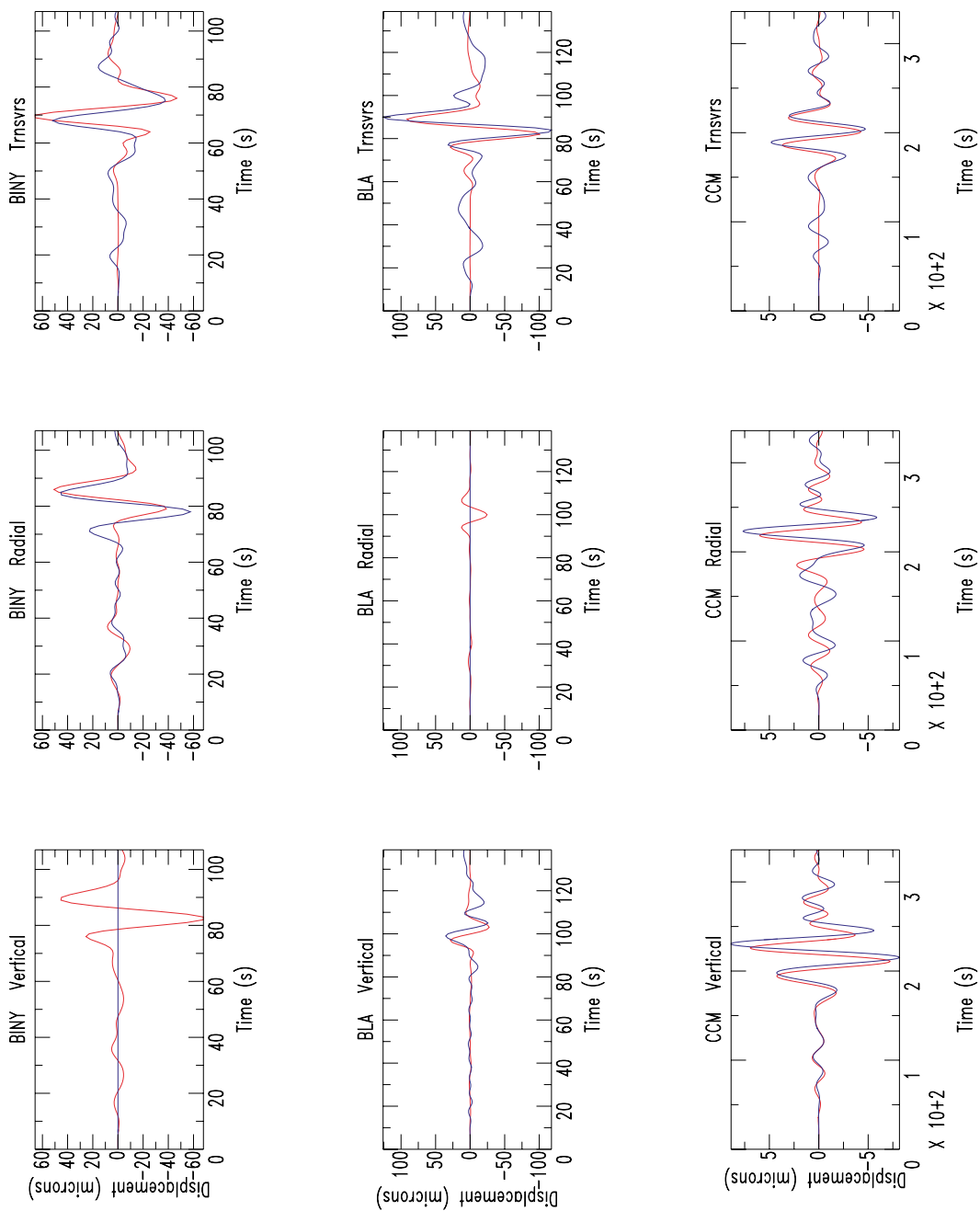


Figure 6.26: Waveform matches between observed and synthetic seismograms from the Grid Search assuming a depth source of 2.5 km. The blue line identifies the observations, the red line indicates the predictions. Each component of each stations is shown with an individual amplitude scale.

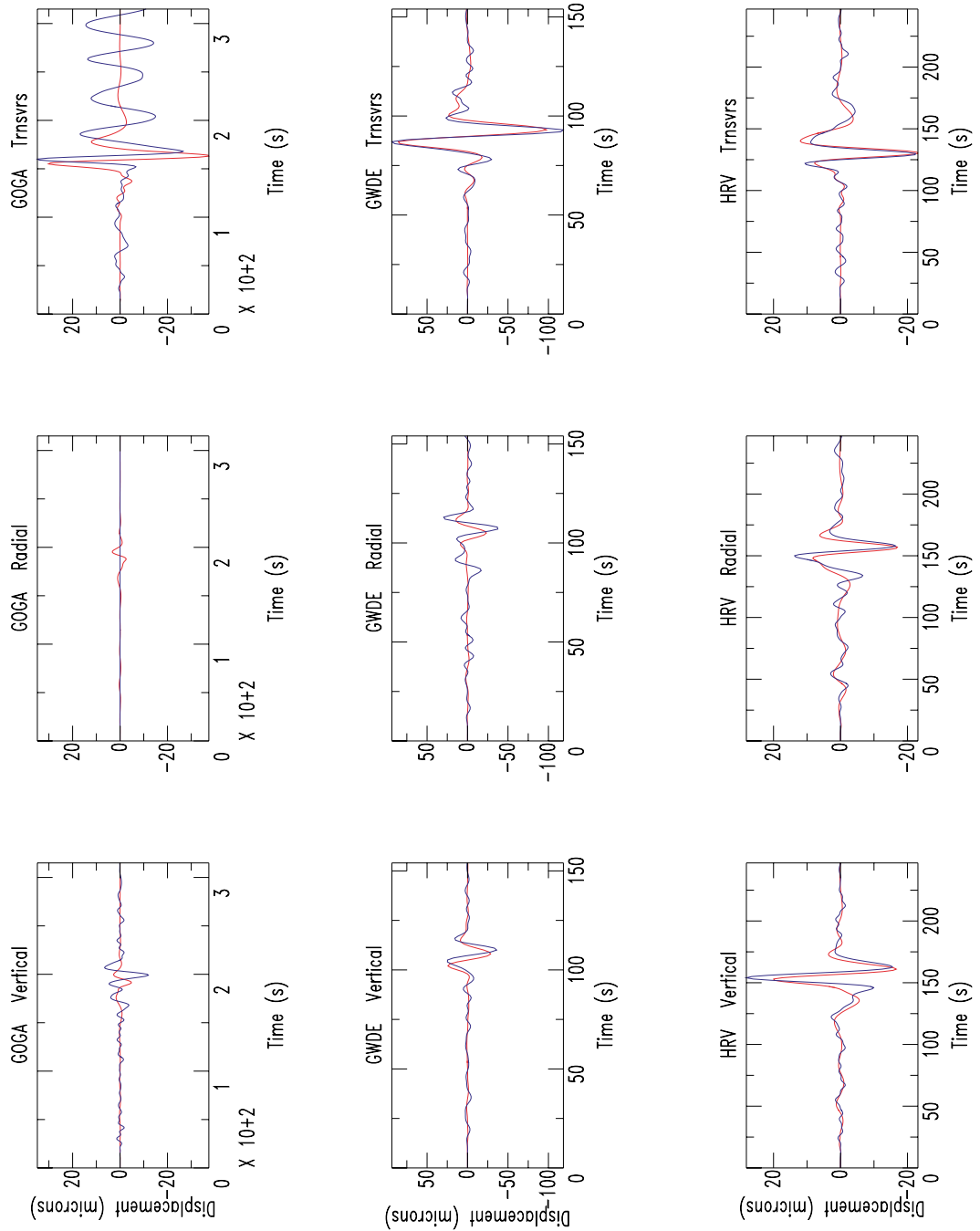


Figure 6.27: Waveform matches between observed and synthetic seismograms from the Grid Search assuming a depth source of 2.5km. The blue line identifies the observations, the red line indicates the predictions. Each component of each stations is shown with an individual amplitude scale.

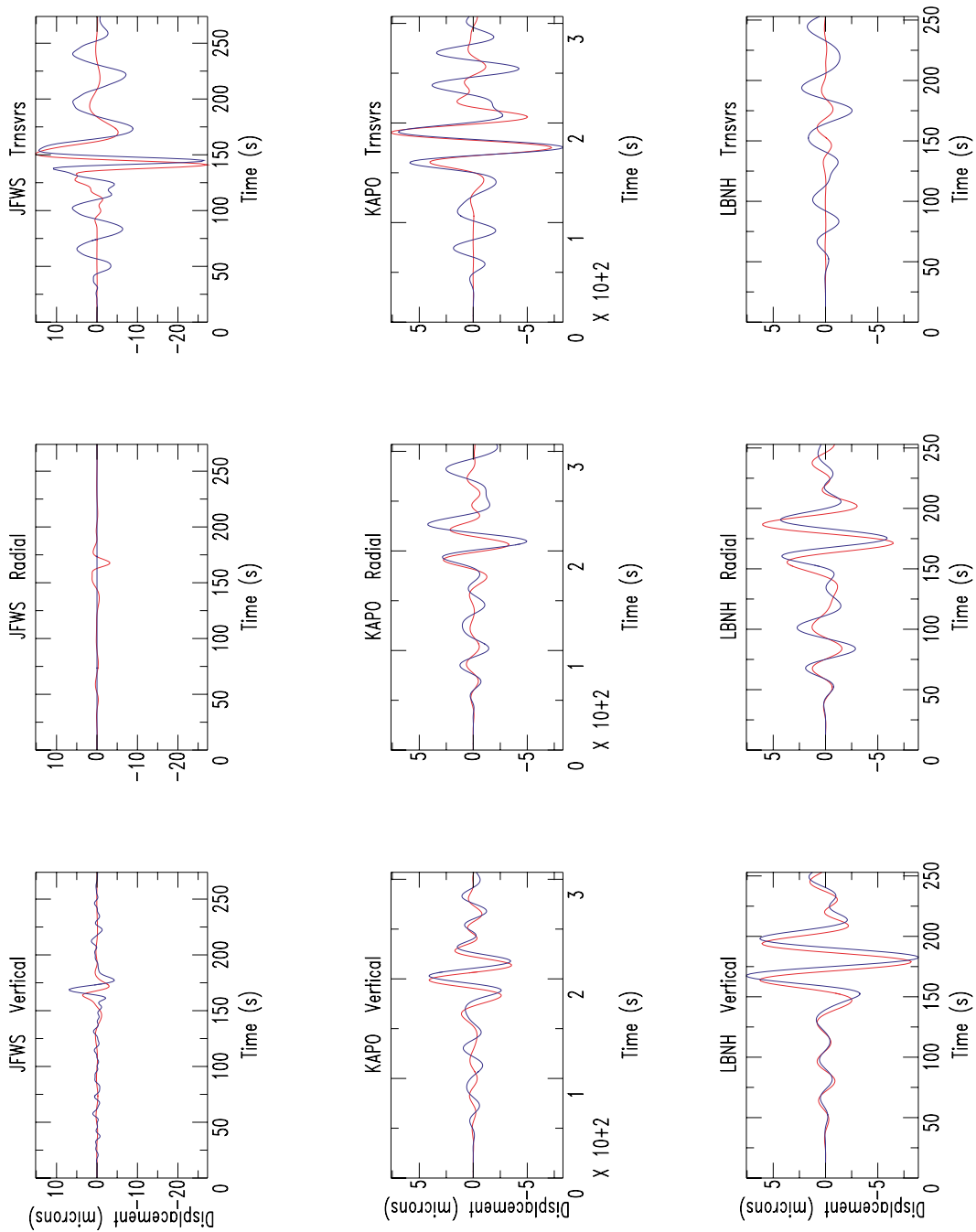


Figure 6.28: Waveform matches between observed and synthetic seismograms from the Grid Search assuming a depth source of 2.5 km. The blue line identifies the observations, the red line indicates the predictions. Each component of each stations is shown with an individual amplitude scale.

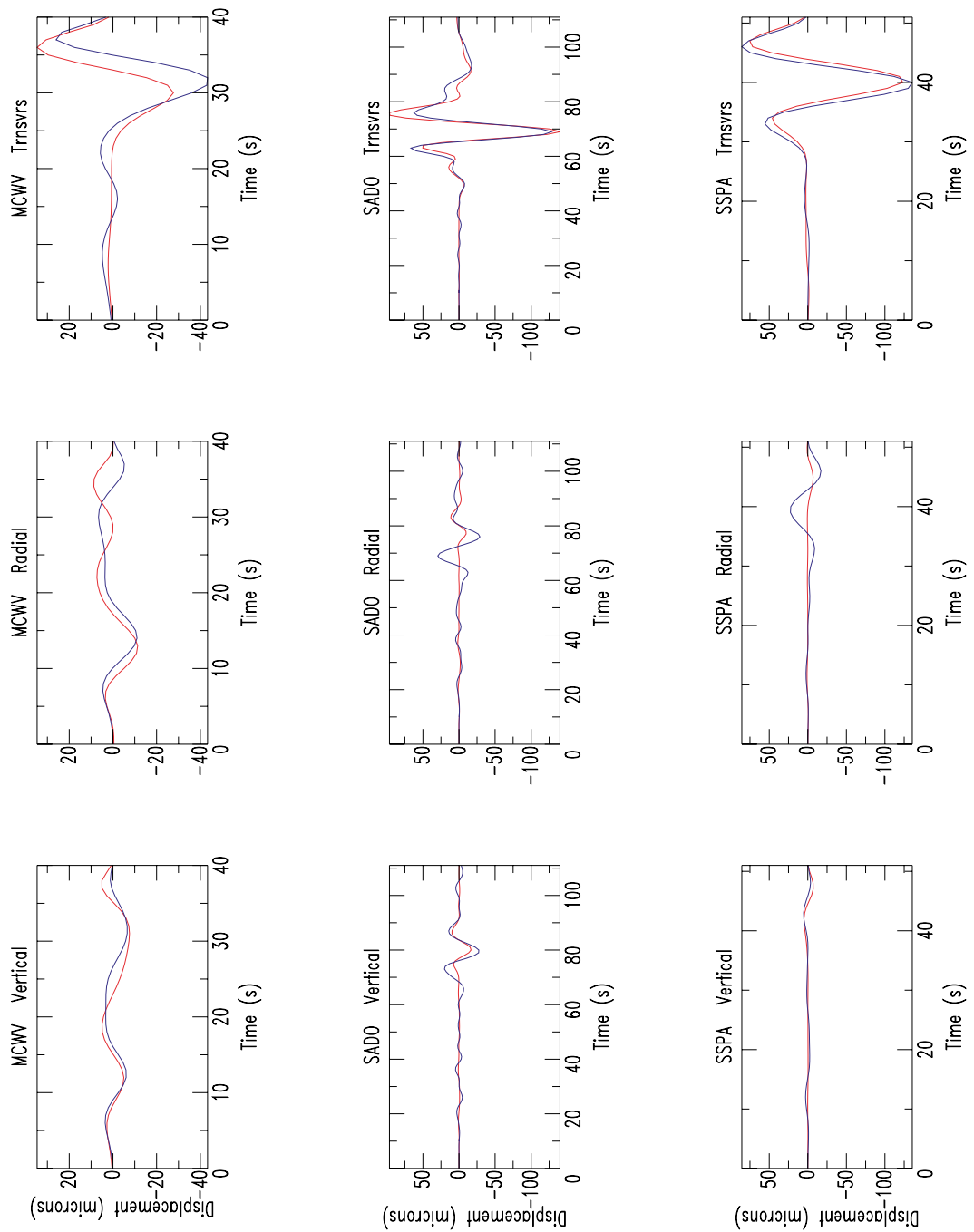


Figure 6.29: Waveform matches between observed and synthetic seismograms from the Grid Search assuming a depth source of 2.5 km. The blue line identifies the observations, the red line indicates the predictions. Each component of each stations is shown with an individual amplitude scale.

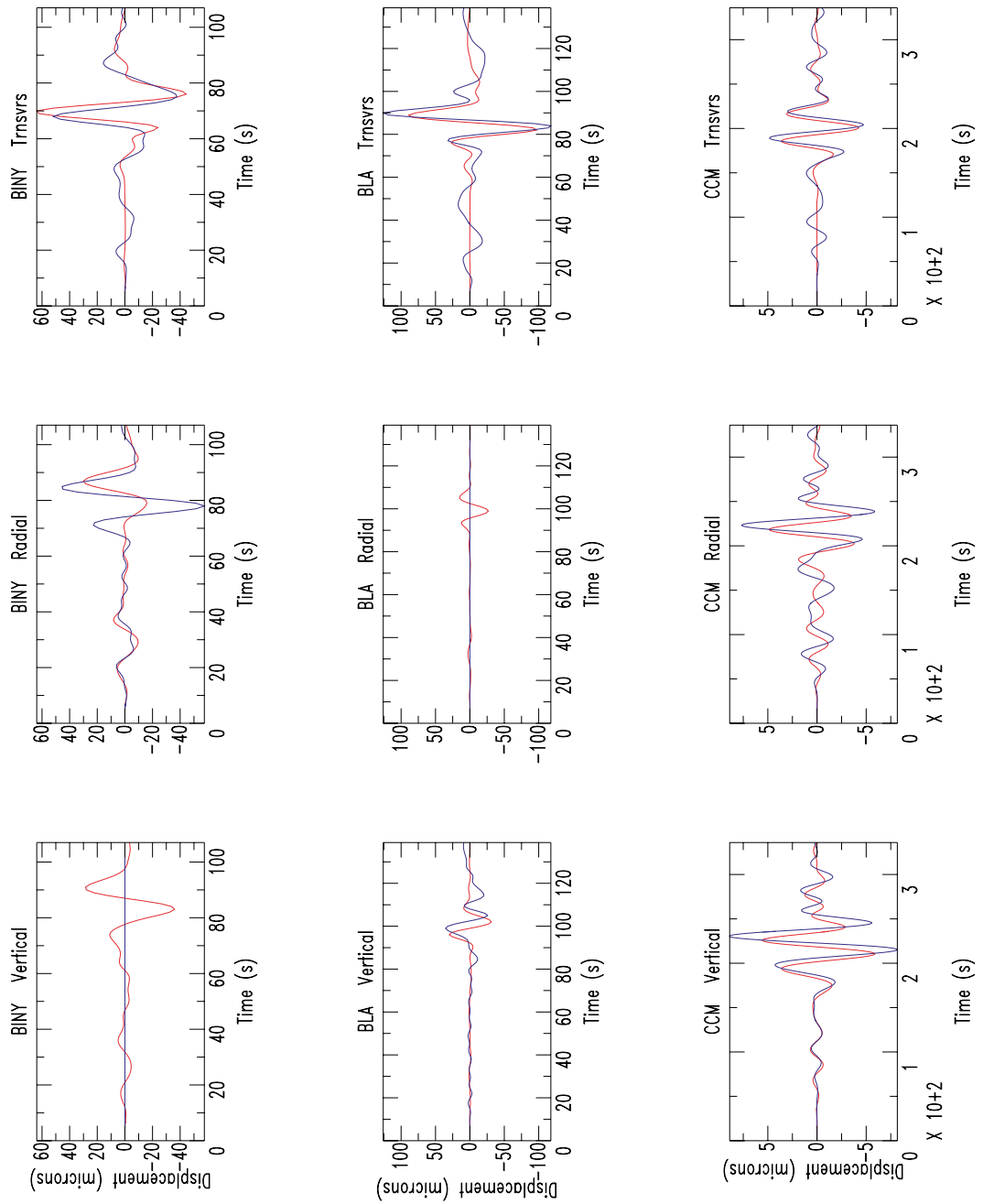


Figure 6.30: Waveform matches between observed and synthetic seismograms from the Grid Search assuming a depth source of 5.0 km. The blue line identifies the observations, the red line indicates the predictions. Each component of each stations is shown with an individual amplitude scale.

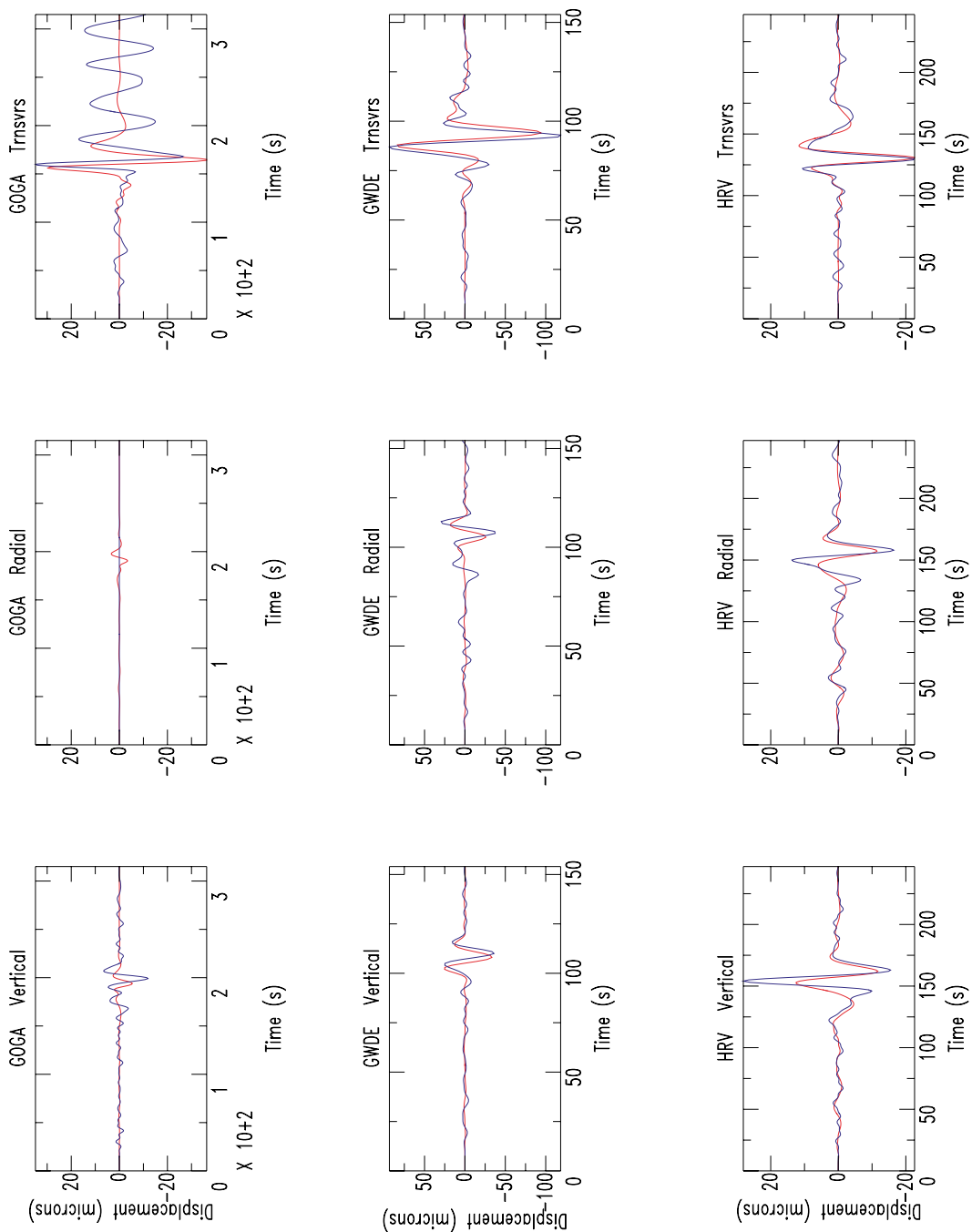


Figure 6.31: Waveform matches between observed and synthetic seismograms from the Grid Search assuming a depth source of 5.0 km. The blue line identifies the observations, the red line indicates the predictions. Each component of each stations is shown with an individual amplitude scale.

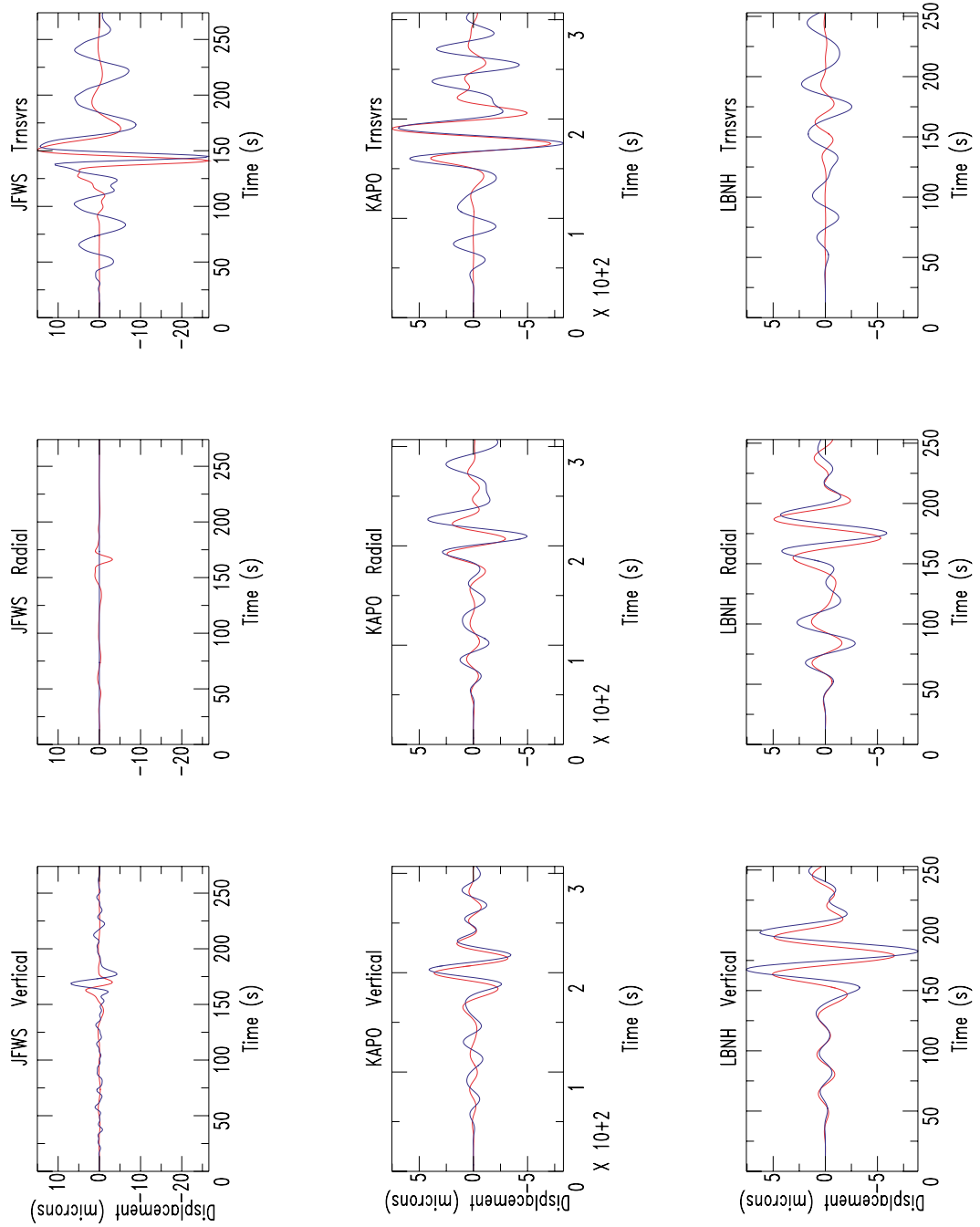


Figure 6.32: Waveform matches between observed and synthetic seismograms from the Grid Search assuming a depth source of 5.0 km. The blue line identifies the observations, the red line indicates the predictions. Each component of each stations is shown with an individual amplitude scale.

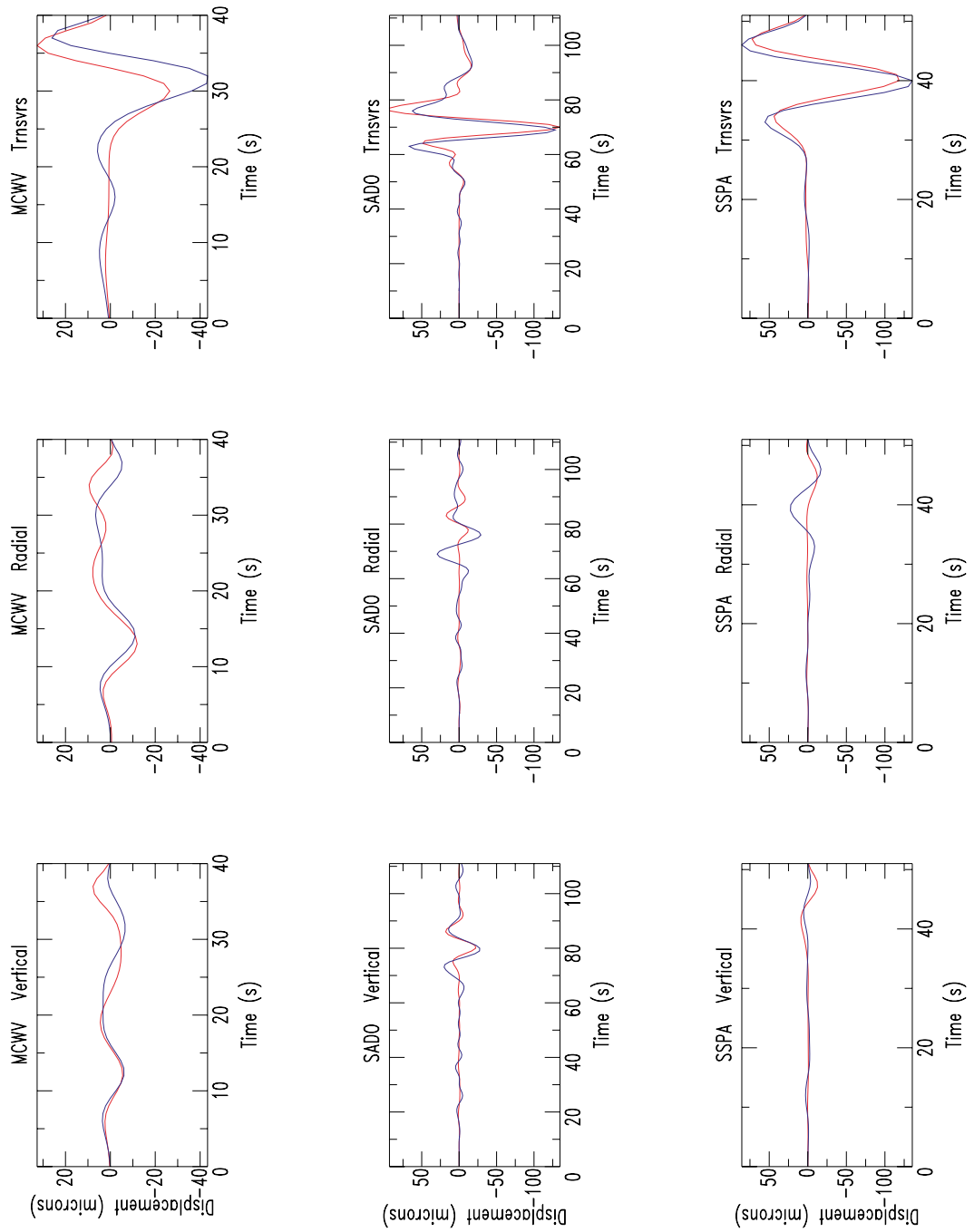


Figure 6.33: Waveform matches between observed and synthetic seismograms from the Grid Search assuming a depth source of 5.0 km. The blue line identifies the observations, the red line indicates the predictions. Each component of each stations is shown with an individual amplitude scale.

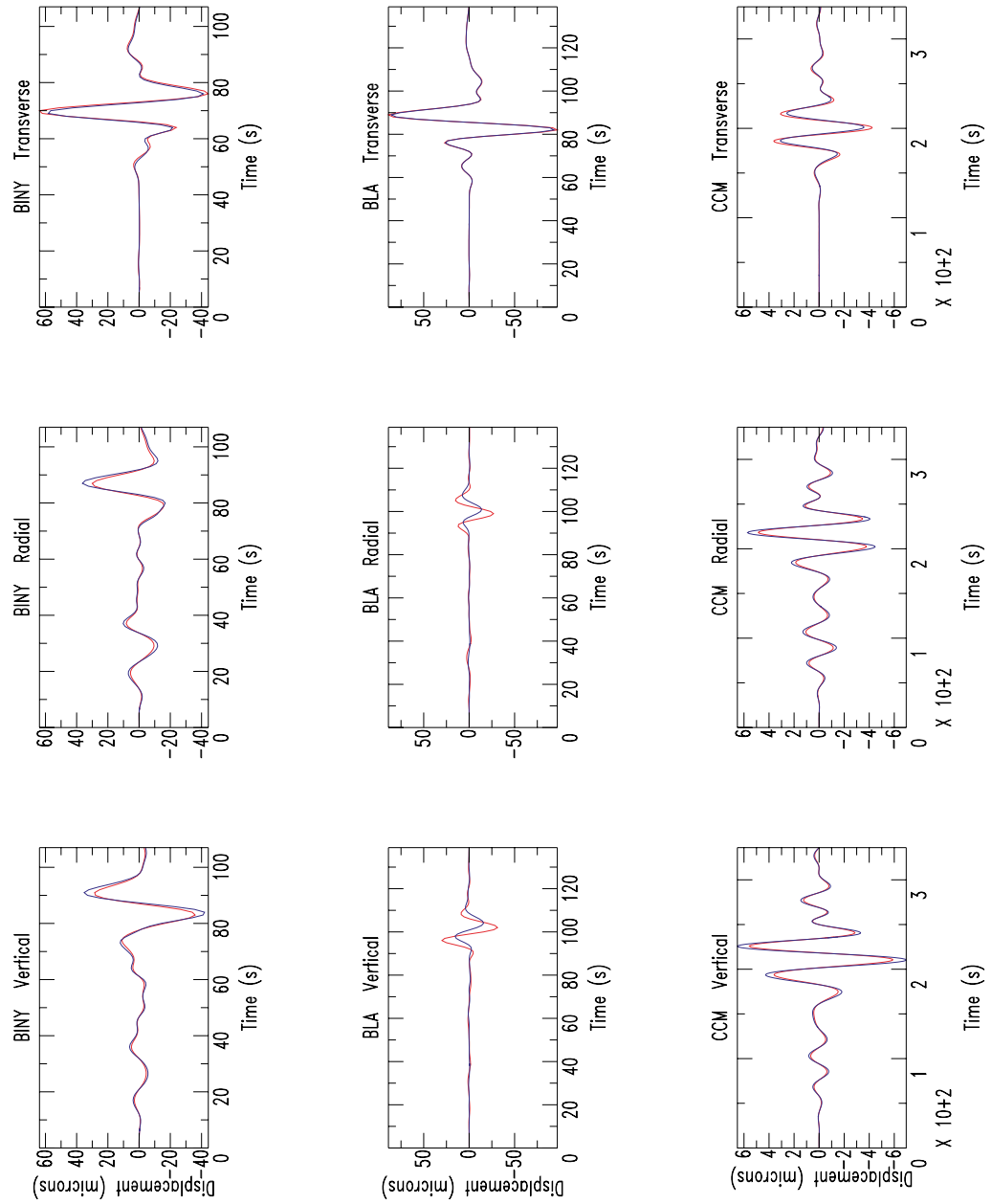


Figure 6.34: Comparison between the synthetics from the least-squares inversion (blue line) and the grid search (red line) for a source depth of 5 km.

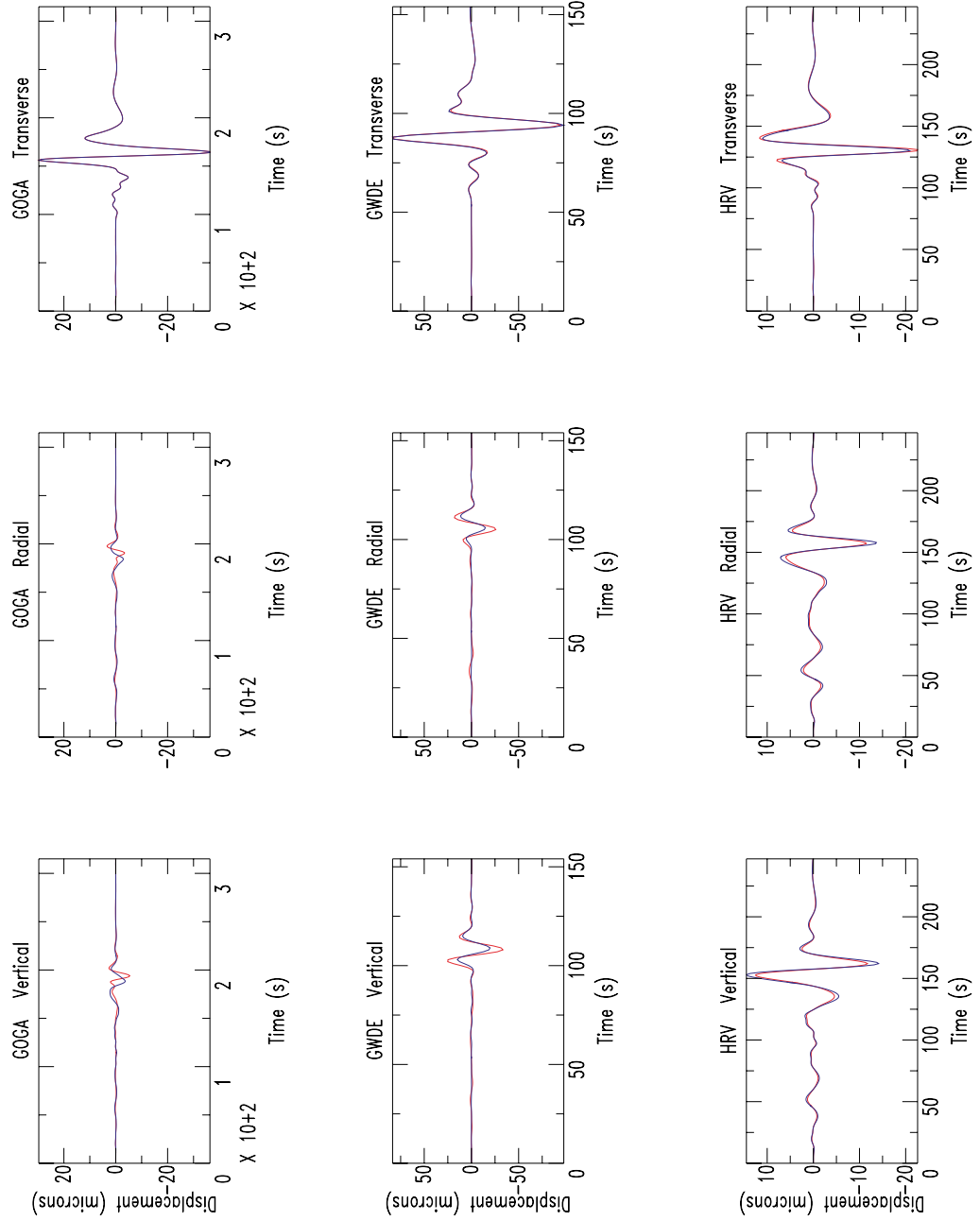


Figure 6.35: Comparison between the synthetics from the least-squares inversion (blue line) and the grid search (red line) for a source depth of 5 km.

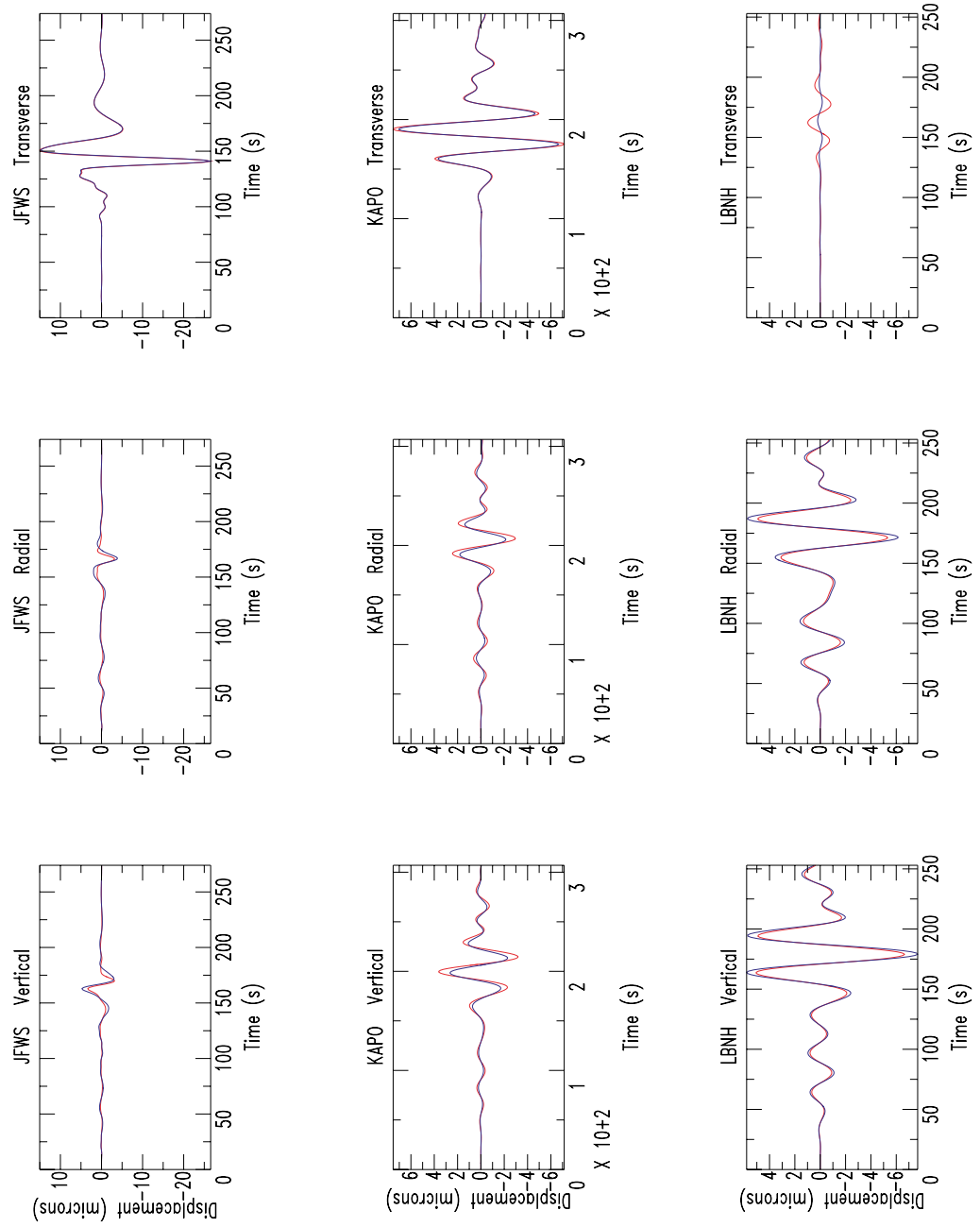


Figure 6.36: Comparison between the synthetics from the least-squares inversion (blue line) and the grid search (red line) for a source depth of 5 km.

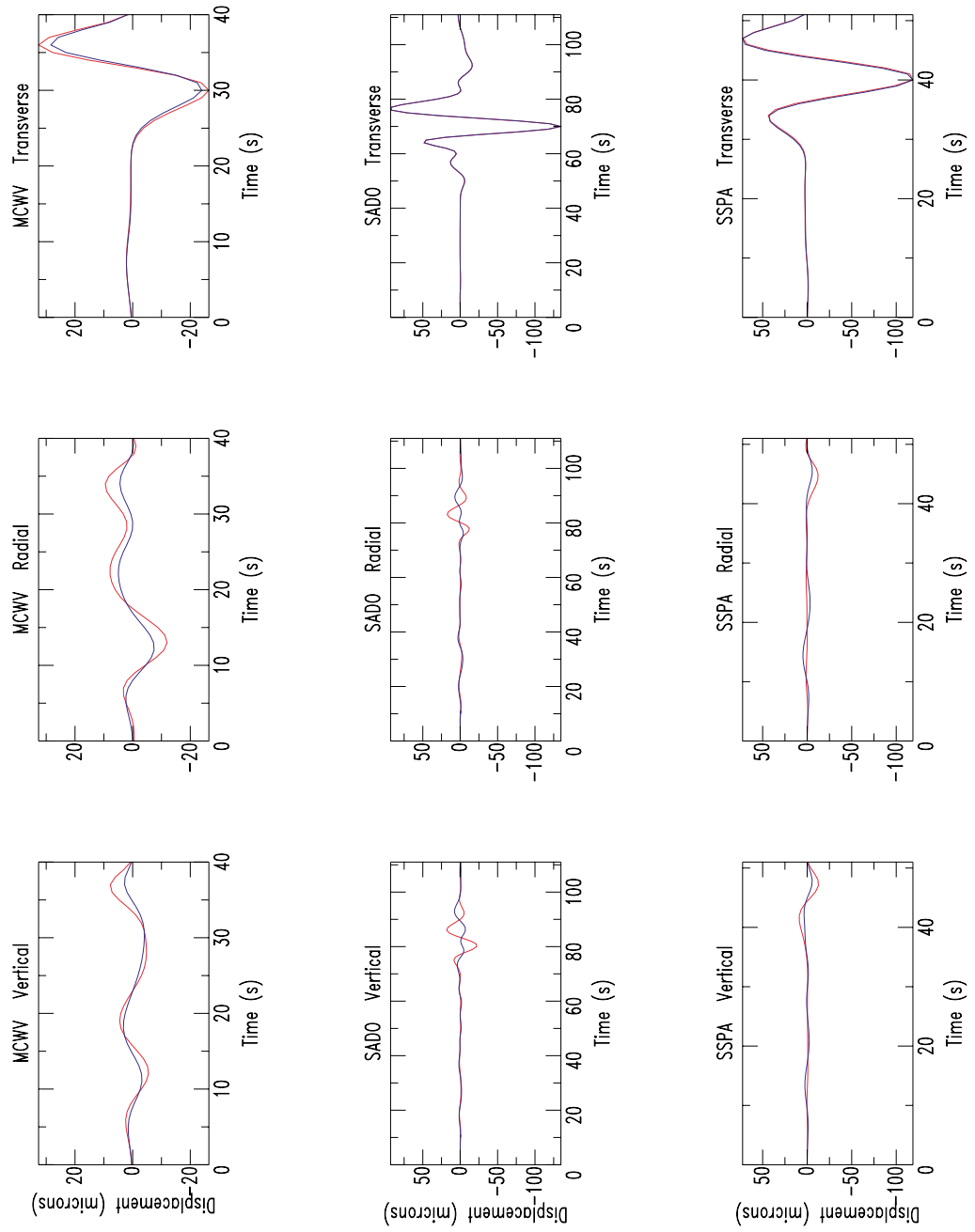


Figure 6.37: Comparison between the synthetics from the least-squares inversion (blue line) and the grid search (red line) for a source depth of 5 km.

A summary of waveform misfit is shown in Figure 6.38. To facilitate the comparison of the L1 and L2 norms, only the L2 misfit is shown (even though the L1 moment tensor inversion and the grid search minimized the L1 norm).

To constrain the depth better, I used a teleseismic P-waveform observation from station YAK, Yakutsk, Russia. Other P waveforms were examined but proved too noisy (not unusual for a small near-vertical strike-slip event). The teleseismic body waves are relatively simple dominated by the direct and primary surface reflections. The seismograms are aligned on the direct P and we can use the relative timing of the depth phases to choose the best source depth. The synthetics were calculated with a uniform crust with a P-velocity of 6.2 km/s. Visual comparison of the observations and predictions (see Figure 6.39) clearly indicates a shallow source, probably near 2.5 km, but conservatively between 2.5 and 5.0 km depth.

Sediment thickness in the region is approximately 2-3 km (World Mapping Project from Exxon Production Research Company). Thus the YAK observations suggest that the source was located near the top of the crystalline basement.

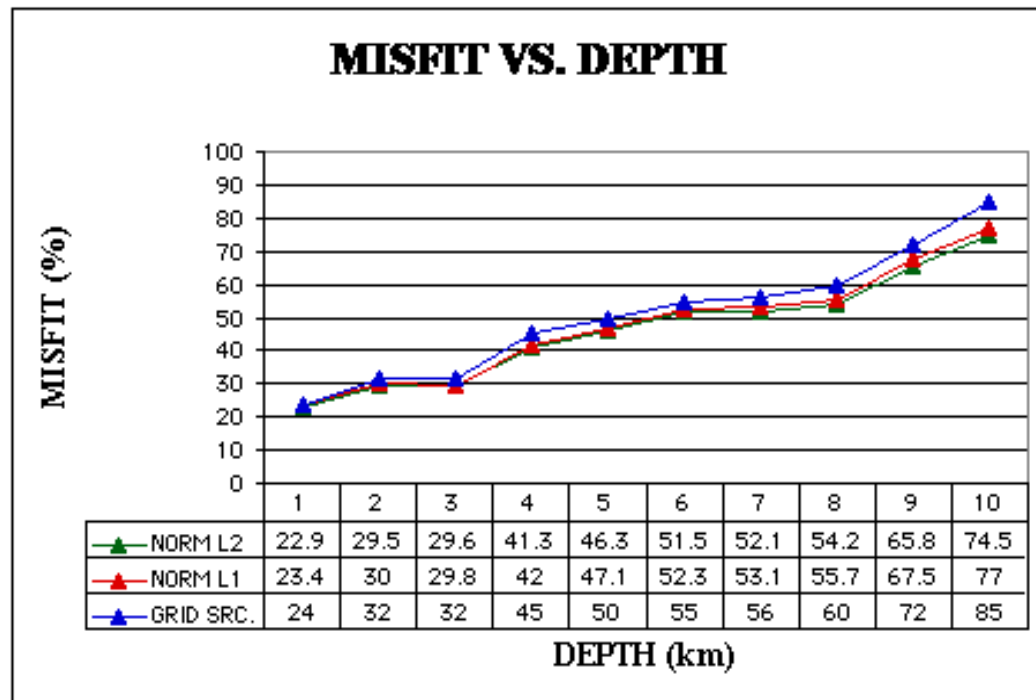


Figure 6.38: Misfit versus depth for least-squares, L1 norm, and grid search inversions.

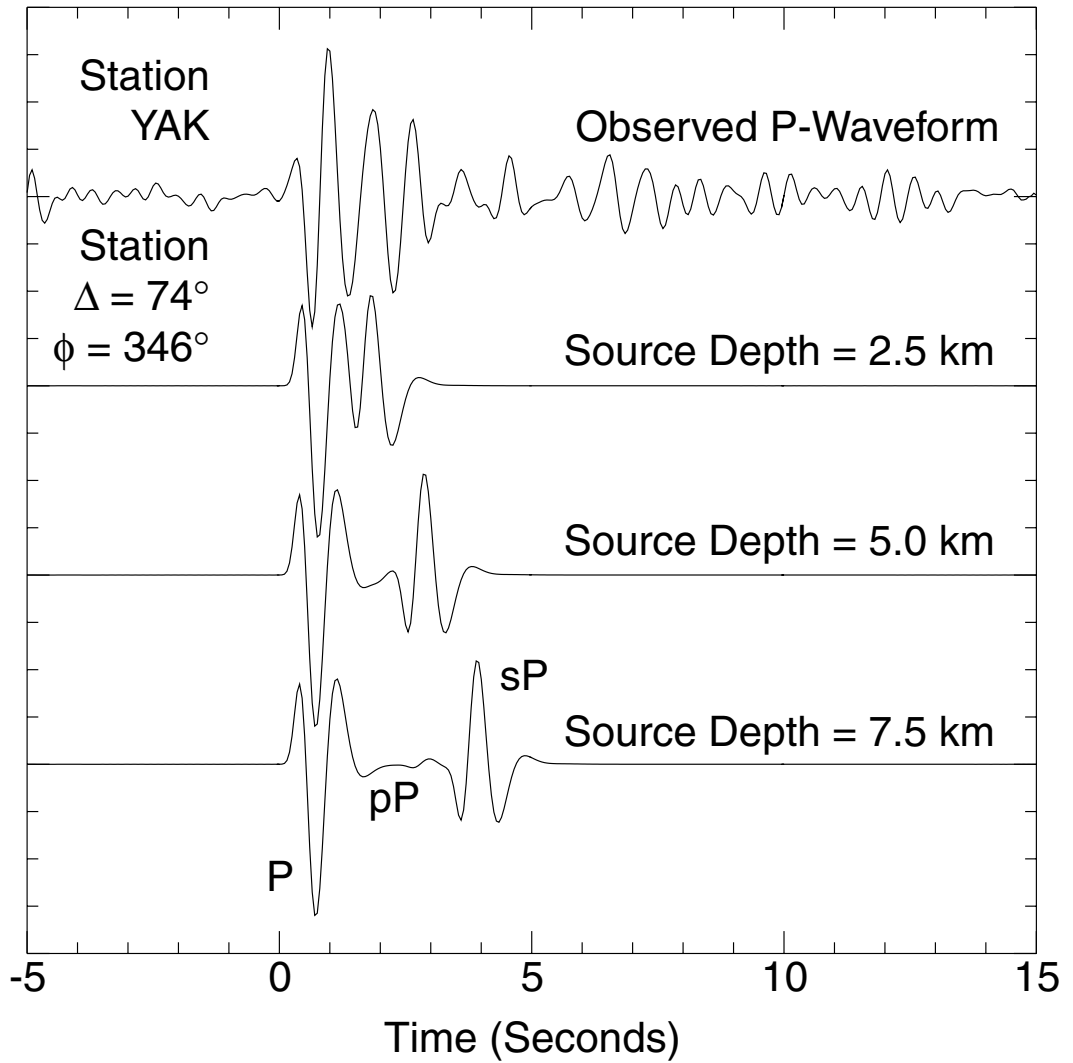


Figure 6.39: Computed body wave seismograms for source depths of 2.5, 5, and 7 km.

7. CONCLUSIONS

Near-real time analysis of seismic waveforms generated by the m_{Lg} 5.2, September 25, 1998 Pennsylvania-Ohio border region earthquake suggested an unusual, large size, non double-couple component to the faulting mechanism. Preliminary checks of these solutions suggested that the non double-couple may have been an artifact caused by the available data. In this study I investigated why early estimates contained large non double-couple component, and I constrained faulting parameters (source depth, fault strike, dip, and slip).

I began performing least-squares, time-domain moment tensor inversions using the observed seismograms from 12 close (epicentral distance less than 1000 km) stations from the USNSN and the CNSN. The fit between observed and synthetic seismograms is not perfect but the major features are explained for a source depth between 2.5 and 7.5 km. The percentage of non double-couple component is high (76%). Then, I performed a L1 norm moment tensor inversion, which is less sensitive to outliers. The results of the this inversion are very close to those obtained from the L2 norm inversion and suggest the unusual source is not a consequence of gross outliers in the data.

To investigate a pure double solution I used a grid search inversion to check the match to the observations for all values of strike, dip, and rake. The results of the grid search for the Pymatuning earthquake are a near-vertical, mostly strike-slip mechanism that resembles the moment tensor

major double couple. The fault planes strike 110 N and 13 N, with dips of 70 ° and 71°, and rakes of 20° and 159°. The estimated moment from the grid search at 5.0 km depth is 5.6×10^{22} dyne-cm, which corresponds to a moment magnitude of 4.5.

Although both the unusual moment tensor and pure double couple fit the regional waveforms well, the preferred solution in this study is the shear dislocation for three main reasons. First, the solution is in agreement with existing estimates of the stress field (Zoback, 1992) (see Figure 7.1). Second, the dislocation angles are consistent with the January 31, 1986 Ohio earthquake faulting mechanism. And third, the Pymatuning earthquake was a small earthquake, so it is most likely simple.

In summary, the Pymatuning earthquake of September 25, 1998, had strike, dip, and rake angles of 110°, 70°, and 20° respectively, with moment magnitude 4.4, and shallow source depth between 2.5 and 5 km.

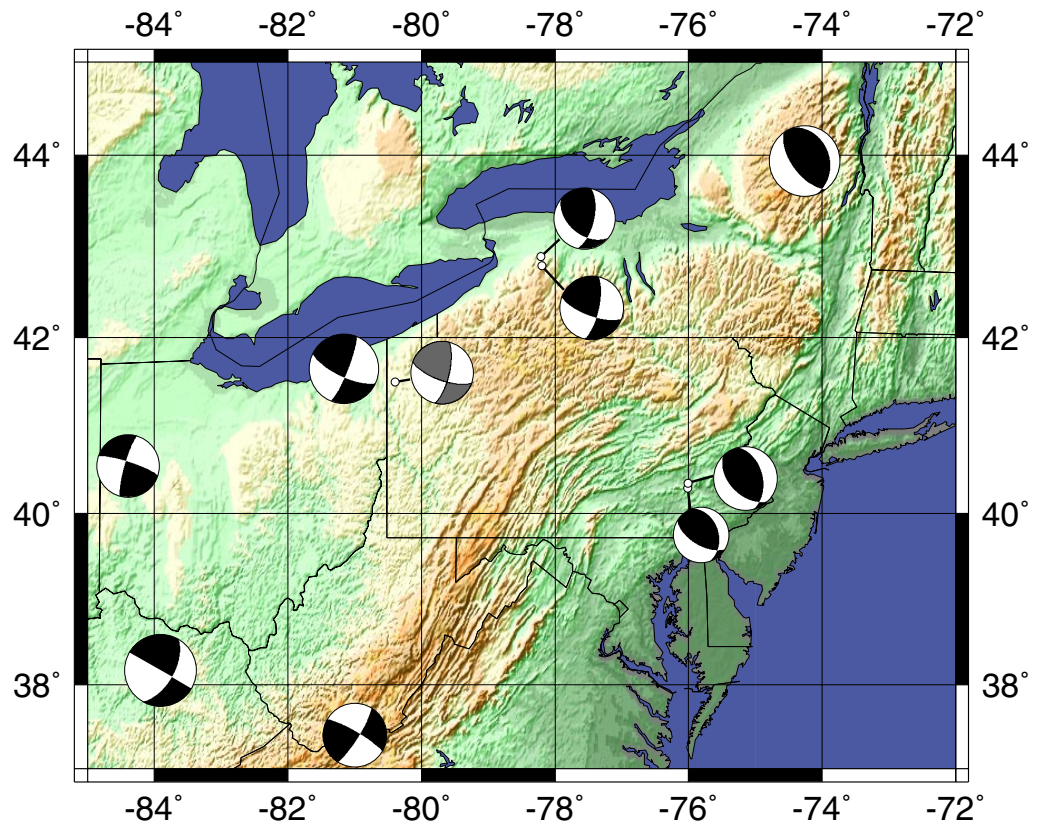


Figure 7.1: Focal mechanisms in Pennsylvania and surrounding states of northeast North America. The Pymatuning event focal mechanism obtained in this study (grey shading for compressional quadrants) is consistent with previous earthquakes in the area.

BIBLIOGRAPHY

Alexandrowicz N., and Cole R., Structure beneath the Appalachian Plateau of northwestern Pennsylvania and relationship to the 1998 Pyramating earthquake, *Geol. Soc. Am.*, V31, No. 2, 1999.

Ammon C.J., Herrmann R.B., Langston C.A., and Benz H., Faulting parameters of the January 16, 1994 Wyomissing Hills, Pennsylvania Earthquakes, *Seismol. Res. Lett.*, Vol. 69, 1998.

Bradley E.A., and Bennett T.J., Earthquake history of Ohio, *Bull. Seismol. Soc. Am.*, V55, 1965.

Chang T.M., Ammon C.J., and Herrmann R.B., Faulting Parameters of the October 24, 1997 Southern Alabama earthquake, *Seismol. Res. Lett.*, V69, 1998.

Coffman J.L., von Hake C.A., and Stover C.W., Earthquake history of the United States, U. S. National Ocean and Atmospheric Administration and U. S. Geological Survey, Publication No 41-1, 1982.

Der Z., Masse R., and Landisman M., Effects of observational errors on the resolution of surface waves at intermediate distances, *J. Geophys. Res.*, 75, 1970.

Dreger D.S., and Helmberger D.V., Broadband modeling of local earthquakes, *Bull. Seismol. Soc. Am.*, V80, 1990.

Dreger D.S., Ritsema J., and Pasyanos M., Broadband analysis of the 21 September, 1993 Klamath Falls earthquake sequence, *Geop. Res. Lett.*, V22, 1995.

Evans K.F., Appalachian stress study, 3, Regional scale stress variations and their relation to structure and contemporary tectonic, *J. Geop. Res.*, 94, 1989.

Frohlich C., and Apperson D.K., Earthquake focal mechanisms, moment tensors, and the consistency of seismic activity near plate boundaries, *Tectonics*, V11, 1992.

Hasegawa H.S., Adams J., and Yamazaki K., Upper crustal stresses and vertical stress migration in eastern Canada, *J. Geop. Res.*, 90, 1985.

Herrin E., and Goforth T., Phase-matched filters: application to the study of Rayleigh waves, *Bull. Seismol. Soc. Am.*, V63, 1977.

Herrmann R.B., Some aspects of band-pass filtering of surfaces waves, *Bull. Seismol. Soc. Am.*, V63, 1973.

Herrmann R.B., Surface wave generation by central United States earthquakes, Ph. D. Dissertation, St. Louis Univ., St. Louis, MO, 1974.

Herrmann R.B., Surface wave focal mechanisms for eastern North American Earthquakes with tectonic implications, *J. Geop. Res.*, Vol. 84, 1979.

Herrmann R.B., Surface-wave studies of some south Carolina earthquakes, *Bull. Seismol. Soc. Am.*, V76, 1986.

Herrmann R.B., Langston C.A., and Zollweg J.E., The Sharpsburg, Kentucky, earthquake of 27 July 1980, *Bull. Seismol. Soc. Am.*, V72, 1982.

Herrmann R.B., and Ammon C.J., Faulting parameters of earthquakes in the New Madrid, Missouri, region, *Engin. Geol.*, 46, 1997.

Hoffman P.F., Precambrian geology and tectonic history of North America, in the *Geology of North America - An Overview*, A.W. Bally and A.R. Palmer, eds., *Geol. Soc. Am.*, 1989.

James T.S., Post-glacial deformation, Ph.D. thesis, Princeton Univ., Princeton, N.J., 1991.

Johnston A.C., and Kanter L.R., Earthquakes in stable continental crust, *Scient. Am.*, March 1990.

Julian B.R., Non-double-couple earthquakes, 1 Theory, *Rev. of Geoph.*, 36, 1998.

Kanamori H., and Given J.W., Use of long-period surface waves for rapid determination of earthquake-source parameters, *Phys. Earth Planet. Int.*, 27, 1981.

Kennett B.L.N., Seismic wave propagation in stratified media, Cambridge University Press, Cambridge, England, 1983.

King P.B., The evolution of North America, Princeton, New Jersey, Princeton University Press, 1977.

Lanczos C., Linear Differential Operators, Van Nostrand, New York, 1961.

Langston C.A., Source inversion of seismic waveforms: the Koyna, India, earthquakes of 13 September 1967, Bull. Seismol. Soc. Am., Vol. 71, 1981.

Lay T., and Wallace T.C., Modern Global Seismology, Academic Press, 1995.

Luza K.V., Madole R.F., and Crone A.J., Investigations of the Meers fault, southwestern Oklahoma, Oklahoma Geol. Survey Special Publication, 1987.

Mitchell B.J., Radiation and attenuation of Rayleigh waves from the southeastern Missouri earthquake of October 21, 1965, J. Geop. Res., V78, 1973.

Mitchell B.J., Regional Rayleigh wave attenuation in North America, J. Geop. Res., V80, 1975.

Mitchell B.J., Nuttli O.W., Herrmann R.B., and Stauder W., Seismotectonics of the central United States, in Slemmons D.B., Engdahl E.R., Zoback M.D., and Blackuell D.D., eds., Neotectonics of North America, Boulder, Colorado, Geol. Soc. Am., V1, 1991.

Nuttli O.W., The Mississippi valley earthquakes of 1811 and 1812: Intensities, ground motion and magnitudes, Bull. Seism. Soc. Am., 63, 1973a.

Nuttli O.W., Seismic waves attenuation and magnitude relations for eastern North America, J. Geop. Res., V78, 1973b.

Nuttli O.W., The seismicity of the central United States, Mem. Geol. Soc. Am., in press, 1978.

Nuttli O.W., The earthquake problem in the eastern United States, *Am. Soc. Civil Engin.*, No 261, 1981.

Nuttli O.W., Average seismic source-parameter relations for mid-plate earthquakes, *Bull. Seismol. Soc. Am.*, V73, 1983a.

Nuttli O.W., Empirical magnitude and spectral scaling relations for mid-plate and plate-margin earthquakes, *Tectonoph.*, 93, 1983b.

Patton H., A note on the source mechanism of the southeastern Missouri earthquake of October 21, 1965, *J. Geop. Res.*, V81, 1976.

Poth C.W., Geology and hydrology of the Mercer quadrangle, Mercer, Lawrence, and Butler Counties, Pennsylvania, *Pennsylvania Geol. Survey*, 4th series, Water Resources Report 16, 1963.

Richardson R.M., and Reding L., North American plate dynamics, *J. Geop. Res.*, 96, 1991.

Romanowicz B., Dreger D.S., Pasyanos M., and Uhrhammer R., Monitoring of strain release in central and northern California using broadband data, *Geop. Res. Lett.*, V20, 1993.

Russell D.R., Herrmann R.B., and Hwang H., Application of frequency variable filters to surface-wave amplitude analysis, *Bull. Seismol. Soc. Am.*, V78, 1988.

Saikia C.K., and Herrmann R.B., Application of waveform modeling to determine focal mechanisms of four 1982 Miramichi aftershocks, *Bull. Seismol. Soc. Am.*, V75, 1985.

Stein S., Sleep N.H., Geller R.J., Wang S.C., and Wortel R., Earthquakes along the passive margin of eastern Canada, *Geop. Res. Lett.*, 6, 1979.

Stover C.W., and Coffman J.L., Seismicity of the United States, 1568-1989 (Revised), U. S. Geological Survey Professional Paper 1527, 1993.

Talwani P., and Rajendran K., Some seismological and geometric features of intraplate earthquakes, *Tectonophysics*, 186, 1991.

Villagomez R.A., The 1995 Macas earthquake sequence, Ecuador: Brittle failure of a flower structure, Masters Dissertation, St. Louis Univ., St. Louis, MO, 1999.

Von Hake C.A., Earthquake Information Bulletin, V8, No 4, May-June 1973.

Wegweisser M., Wegweisser A., Babcock L., and Harper J.A., Morpho-tectonic features associated with cross-strike discontinuities in Upper Devonian rocks of northwestern Pennsylvania, Guidebook for the 63rd Annual Field Conference of Pennsylvania Geologists, Oct. 1-3, 1998.

Wheeler R.L., and Johnston A.C., Geologic implications of earthquake source parameters in central and eastern North America, Seismol. Res. Lett., V63, No 4, 1992.

Zoback M.D., and Zoback M.L., Tectonic stress field of North America and relative plate motions, in The Geology of North America, Decade Map Vol. 1, Neotectonics of North America, edited by B. Slemmons et al., Geological Society of America, Boulder, Colorado, 1991.

Zoback M.D., et al., New evidence on the state of stress of the San Andreas fault system, Science, 238, 1987.

Zoback M.D., Prescott W.H., and Kroeger S.W., Evidence for lower crustal ductile strain localization in southern New York, Nature, 317, 1985.

Zoback M.L., Stress field constraints on intraplate seismicity in eastern North America, J. Geoph. Res., V97, 1992.

Zoback M.L., et al., Global patterns of tectonic stress, Nature, 341, 1989.

Some of the information used in this study is available on line at the following WWW pages:

www.geo.lsa.umich.edu/~ruff/980925.OhioPenn/EQoverview.html
(maintained by Professor Larry Ruff, University of Michigan)
groundmotion.cr.usgs.gov/pym/pym.htm
groundmotion.cr.usgs.gov/PYMLPA_Geo/
(maintained by Dr. Ed Cranswick, USGS)

Vita Auctoris

Monica Maceira Quintas was born on April 22, 1973, in Santiago de Compostela, in the green northwest region of Spain. She was a daddy's girl and she was going to study what her father always wanted for her: medicine; but sometime in her last two years of High School, something changed her mind and in September 1991 she enrrolled herself in the University of Santiago de Compostela as a physics student. After three first years full of math and abstract physics, she decided to move to Madrid to study the most wonderful branch of Physics, Geophysics.

In July 1996 she received her Bachelor's degree in Physics - with specialization in Earth and Cosmos Physics. She stayed one more year in Madrid working for free for the Earth and Atmospheric Sciences Department of the Universidad Complutense. During that year she received the offer for joining another Earth and Atmospheric Sciences department, but this time very far from her home. She accepted the challenge and on August 23, 1997, she landed on what it was going to be her home for a couple of years, Saint Louis. From that day to the present, the author has been attending Saint Louis University for pursuing her Master of Science and it looks like, finally, she would get her degree as a Christmas present just before the new milenium arrives.